



**I
N
A
O
E**

**Instituto Nacional de Astrofísica,
Óptica y Electrónica.**

**Physics and technique of detecting
pulsed and continuous light radiation.**

By:

Ana Luz Muñoz Zurita

A thesis submitted to the program in
Optics

Optics Department

In partial fulfillment of requirements
for the degree of

Doctor of Science in Optics

Supervised by:

Dr. Alexandre S. Shcherbakov
(INAOE- México).

Dr. Joaquín Campos Acosta
(IFA.CSIC-Spain).

©INAOE 2009

Derechos Reservados

El autor otorga al INAOE el permiso de
reproducir y distribuir copias de esta tesis en su
totalidad o en partes.



AGRADECIMIENTOS.

Agradezco a Dios, por llegar a ser y estar en donde nunca imagine.

A CONACYT por el apoyo a través de la beca 170240 y el proyecto 61237.

A mi Madre Amparo Zurita Vda de M, por todo su apoyo, comprensión, cariño, por ser mi madre, amiga, compañera.

A mis hermanos Guillermo (M) y Alejandro (w) por su apoyo, cariño, consentimientos.

A mis asesores:

Dr. Alexandre S Shcherbakov, gracias por su apoyo, amistad, comentarios, conocimientos, correcciones, enseñanzas, por confiar en mí, (Gracias por todo, Annuska).

Dr. Joaquín Campos Acosta, muchas gracias por recibirme en Madrid, por apoyarme, por guiarme, por sus comentarios, conocimientos, enseñanzas, consejos, por confiar en mí y por su amistad.

A mis sinodales:

Dr. Carlos G. Treviño, Dr. Julio Cesar Ramírez, Dra. Alicia Pons, Dra.Svetlana Mansurova, por todos los comentarios, observaciones y correcciones hacia esta tesis.

Al Dr. Gabriel Martínez Niconoff, por haber confiado en mí, por su apoyo en cierta situación difícil.

A mi gran Familia Zurita. (Tíos, primos y mis queridos sobrinos).

A mi familia en Madrid: Carmen Glz, Conny Huerta, Ivonne Bazan, Martín Leal, Leo Laguna, Emilia Pardo, Israel Sánchez (BALU), Vladimir Aldana, Laura Tocco, Daniel Pérez.

A mis amigos: Karim, Bernabé, Ariel, Mercedes, Dario, Juan Manuel, Rosalba, Alberto, Marco Antonio, Daniel, Maru.

Al Dr. Wyatt Anthony Crudup por su amistad y apoyo.

A todo el personal del INAOE y del IFA-CSIC.

DEDICATORIAS.

† A mi papá G. Guillermo Muñoz Romero, como poder decirte que me haces falta, que desde que falleciste mi vida cambio, aunque han pasado casi 18 años, aun te extraño, gracias papá por que hasta el ultimo minuto de tu vida pensaste en mí, TQM.

INDEX

Introduction	6
CHAPTER 1	12
FUNDAMENTALS CONCEPTS	
1.1 Optical pulses	12
1.2 Pulse shape characterization and properties	13
1.3 Measurement techniques	16
1.3.1 Correlation functions	17
1.3.2 Correlation methods	23
1.3.3 Pulsewidth measurements	25
1.4 Phase matching	27
1.5 Silicon photodiodes	29
1.6 InGaAs photodiodes	31
1.7 Formulation of the problem	34
1.8 References	35
CHAPTER 2	
DETERMINING THE TIME-FREQUENCY PARAMETERS OF LOW- POWER BRIGHT PICOSECOND OPTICAL PULSES WITH GAUSSIAN SHAPE.	38
2.1 The Wigner time-frequency distribution for the Gaussian pulse with $T = 1$, and the varying parameter b	39
2.2 The gaussian pulse with a high-frequency filling	43
2.3 A new technique of measuring the train-average pulse width as well as the value and sign of the frequency chirp of picosecond optical pulses in high- repetition-rate trains	49
2.4 Conclusions	55
2.5 References	56

CHAPTER 3	59
DETERMINING THE TIME-FREQUENCY PARAMETERS OF LOW-POWER BRIGHT PICOSECOND OPTICAL PULSES WITH HYPERBOLIC-SECANT SHAPE.	
3.1 The joint Wigner time-frequency distributions for the sech-like pulses	61
3.2 Square-average determination for the parameters of a sech-pulse	66
3.3 A sech-pulse with a high-frequency filling	69
3.4 Auto-correlation function for a sech-pulse with the frequency chirp	69
3.5 Application of the above proposed technique to sech-like pulses	79
3.6 Conclusions	83
3.7 References	84
CHAPTER 4	87
APPLYING A TRIPLE AUTO-CORRELATION TO MEASURING THE ENVELOPES OF ULTRASHORT OPTICAL PULSES	
4.1 Triple auto-correlation	87
4.2 The triple auto-correlation function for a one-dimensional signal	89
4.3 The algorithm of recovering the temporal signal from its triple auto-correlation function	93
4.4 The algorithm of recovering the temporal signal from its triple auto-correlation function	97
4.5 Application to the characterization of picosecond optical pulses	98
4.6 Conclusions	102
4.7 References	102
CHAPTER 5	104
ANALYSIS OF SILICON PHOTODIODES SPECTRAL REFLECTANCE	
5.1 Photodiode spectral reflectance	106
5.2 Experimental procedure of Silicon Photodiodes	108
5.3 Analysis of Spectral Reflectance of Silicon Photodiodes	110
5.4 Conclusions	114
5.5 References	115

CHAPTER 6	117
STUDY OF REFLECTANCE AND NEW MODEL OF INTERNAL QUANTUM EFFICIENCY OF InGaAs/InP PHOTODIODES	
6.1 InGaAs/InP-photodetectors	117
6.2 Experimental procedure	118
6.3. Analysis of Reflectance	120
6.4 New Model of Quantum Internal Efficiency of some photodetectors of InGaAs	123
6.4.1 External quantum efficiency	124
6.4.2 Photodiode structure	125
6.4.3 Internal quantum efficiency	126
6.5 Conclusions	128
6.6 References	129
CHAPTER 7	131
GENERAL CONCLUSIONS	
STATEMENTS	134
APPENDIX I:	136
ORIGINATING THE JOINT WIGNER TIMEFREQUENCY DISTRIBUTION	
Index of Figures	141

INTRODUCTION

In optics, the measure of the magnitudes is associated with the radiant energy in the optical interval of the electromagnetic spectrum (ultraviolet, visible and infrared) [1]. One of the magnitudes associated to the radiation is the quantity of energy transported and for multiple reasons it is necessary to carry out measurements of radiant energy with higher precision and accuracy. This necessity has impelled the most precise and exact search of measuring system [2].

The rapid development of picosecond, femtosecond and attosecond technology has allowed us to examine fundamental process in materials. To accurately determine an interval of short duration, one must first be able to measure its duration. One measuring technique is to identify events that recur regularly over and over again, such as the passing of a day. The ancients knew how to subdivide time by using devices such as sundials. For measuring still shorter time intervals, they used the hour glass or allowed a specific quantity of water to drip from cistern. However, they apparently showed no interest in studying physical events with these methods [3].

Much of the ground work for picosecond light pulse technology was laid by related discoveries during the five years preceding the use of high power modelocked lasers. All main lasers now used for picosecond work were discovered during this period: the ruby, Nd:glass, Nd YAG, and dye lasers [4].

Besides the discovery of lasers in this five years period, many nonlinear optical effects were detected, some of which were shortly to become an integral part of picosecond techniques, e.g. second and third harmonic generation [5].

To measure the power associated to optical radiation a photodetector is used. Depending on the power level, spectral distribution, temporal features and other geometric features of the beam different types may be used. Photodiodes as silicon, InGaAs/InP and other, are the most suitable photodetectors in many applications (Ana may include some at this point) as far as the spectral range of interest is within their spectral sensitivity interval. Perhaps their greatest inconvenience is that responsivity, the response amount by unit of incident power, is depending on wavelength. Consequently, to use them as radiometers they have to be calibrated at every wavelength of interest, what it is routinely done in calibration laboratories of different levels. However, another approach can be taken to know the responsivity of a photodiode based on the physics of the interaction between the radiation and the photodiode. This approach has been realized in the case of silicon photodiodes and has shown to be very useful not only to know the responsivity but to know about other detectors features as linearity and response uniformity. Therefore the goal in this thesis is to study the possibility of applying this approach to InGaAs/InP photodiodes.

Assuming that the photodiode is used in the short-circuit configuration, i. e. measuring the short circuit current produced by the incoming optical radiation, the physical phenomena occurring in this system can be analyzed and a simple equation can be derived for the responsivity. First, the absorbed radiation power is obtained from the incoming one except for the reflected fraction, since the photodiodes are designed as opaque devices to improve their efficacy. Then the absorbed power will excite electrons and holes within the diode, which will contribute to the short circuit current with different probability. The probability is mainly related to the position where the charges are excited within the photodiode, varying from almost 1 in the charge depletion region to almost 0 at the back of the photodiode. Therefore, since the absorption distribution depends on wavelength, the charge collection efficiency

will (internal quantum efficiency) also depends on wavelength. Then if the reflectance and internal quantum efficiency are known the responsivity will be known without comparing to another calibrated radiometer.

To try this approach with success the photodiode manufacturing technology has to be mature and be able to produce almost perfect devices from a solid state point of view (very low charge losses) and very flat and plane sensitive surfaces. As it happened some years ago with silicon photodiodes, it seems that the manufacturing of InGaAs/InP photodiodes has reached that maturity stage at present. Afterward, if the internal structure and complex refraction index of the materials composing the device were known, a model could be developed to calculate the reflectance and internal quantum efficiency of the devices. Since these data are not completely known because manufacturers do not publish them, it is necessary to measure the reflectance, assume a structure model from an optical point of view and fit experimental data to the model to be able to know reflectance at every wavelength. Then measuring the responsivity at some wavelengths, internal quantum efficiency can be obtained from those values and the corresponding reflectance values.

Again, assuming a structure, a model can be developed for the internal quantum efficiency and fitted to values calculated before. This is the alternative approach that is suggested and used in this thesis to know the responsivity of InGaAs/InP photodiodes.

As important as knowing responsivity is to know its temporal stability for optical radiation measurements, that will depend in turn on the reflectance and internal quantum efficiency stabilities. Since stability studies have to be done over a relatively wide set and large area InGaAs/InP photodiodes are still expensive, it was decided for the purpose of this thesis to focus the study on the

reflectance variability of a wide set of silicon photodiodes available at the Institute for applied physics. The similarity between these two kinds of photodiodes could help to extrapolate results from one to another. Temporal stability of silicon internal quantum efficiency has been studied yet by different authors, therefore it has not been included in this thesis.

Structure of the thesis.

Chapter 1 presents the fundamental concepts of this thesis, the related to the study of optical pulses, measurement techniques, as well as on the silicon and InGaAs/InP photodiodes.

Chapter 2 and 3 present approaches to the characterization of low-power bright picosecond optical pulses with an internal frequency modulation simultaneously in both time and frequency domains in practically much used cases of the Gaussian and sech-like shapes. In so doing, first of all, it implement the technique for recognizing the width as well as the magnitude and sign of the frequency chirp peculiar for such ultrashort pulses in high-repetition-rate (approximately 1 GHz) trains.

Chapter 4 presents an approach based on the algorithm of the triple autocorrelations the key features of a novel experimental technique are related to both accurate and reliable measurements of the train-average parameters inherent in sequences of picosecond optical pulses with an internal frequency modulation. Here, three types of pulse envelopes, namely, Gaussian, rectangular, and smooth asymmetric shapes are under analysis and algorithmic investigation.

Chapter 5 presents a study about the reflectance of silicon photodiodes, with two goals: To study the variability of reflectance among photodiodes from a single batch, which is important for silicon trap

detectors, and to study the reflectance ageing of some silicon photodiodes used as standards during six years.

Chapter 6 presents the study of reflectance and internal quantum efficiency of InGaAs/InP photodiodes. Models for them are proposed and fitted to experimental data obtaining a good agreement.

Chapter 7 presents the general conclusions of this Ph.D. thesis. Finally the statements of this thesis are formulated.

References .

- [1]. Dereniak E.L and Boreman G.D. “Infrared detectors and systems”, John Wiley & Sons 239-333, (1996).
- [2]. A.S. Grove. “Physics and technology of semiconductors devices”, John Wiley & Sons 121-235, (1996).
- [3]. L.P.Boivin “Automated absolute and relative spectral linearity measurements on photovoltaic detectors”. Metrologia, **30**, 355-360, (1993).
- [4]. J.Geist, E.F. Zalewski & A.R. Schaefer “Spectral response self calibration and interpolation of silicon photodiodes” Applied Optics, **35**, 3795-3799 (1980).
- [5]. K. D. Stock and R. Heine, “Spectral characterization of InGaAs trap detectors and photodiodes used as transfer standards”, Metrologia **37**, 449-452, (2000).

[6]. L. Werner, R. Friedrich, U. Johannsen and A. Steiger, ‘Precise scale of spectral responsivity for InGaAs detectors based on a cryogenic radiometer and several laser sources’, *Metrologia* **37**, 523-526 (2000).

[7]. P. Corredera, J. Campos, M.L. Hernanz, J.L. Fontecha, A. Pons and A. Corróns, ‘Calibration of near Infrared Transfer Standards at Optical Fibres Communication Wavelengths by Direct Comparison with a Cryogenic Radiometer’, *Metrologia* **35** 273-277 (1998).

CHAPTER 1.

FUNDAMENTAL CONCEPTS.

In this section a short introduction to nonlinear optics and basic concepts on photodetectors are given. They will be concentrating on optical pulses, measurement techniques, as well as on silicon and InGaAs/InP photodiodes.

1.1 Optical pulses

Optical pulses are flashes of light, which are often generated with lasers (laser pulses) and delivered in the form of laser beams. Due to the high optical frequencies, optical pulses can be extremely short (ultrashort), with their optical bandwidth spans a significant fraction of the mean frequency. Therefore, amplified ultrashort pulses are very important for high-intensity physics, studying phenomena such as multi-photon ionization, high harmonic generation, or the generation of even shorter pulses with attosecond durations. Depending on the required pulse duration, pulse energy, and pulse repetition rate, different methods for pulse generation, pulse compression and pulse characterization are used, overall covering extremely wide parameter regimes. Pulse propagation in media has many interesting aspects.

The peak of a pulse in a transparent medium propagates with the group velocity, not the phase velocity. Dispersion can cause temporal broadening (or compression) of pulses. For high peak intensities, optical nonlinearities can strongly affect the pulse propagation, often they lead to pulse broadening, but strong nonlinear compression is also possible [1]. There are various methods for measuring the pulse duration achieved or for pulse characterization in other respects. For measuring the duration of ultrashort pulses purely optical techniques are very important since electronics are too slow for such purposes. However,

such method not efficient, because most of the light will be lost at the modulator, and also the pulse duration is limited by the speed (bandwidth) of the modulator. Pulses with much higher energies and much shorter durations can be generated in pulsed lasers [2].

In optics, an ultrashort pulse of light is an electromagnetic pulse whose time duration is on the order of the femtosecond (10^{-15} second). Such pulses have a broad optical spectrum, and can be created by mode-locked oscillators. They are commonly referred as ultrafast events [3].

1.2 Pulse properties.

Although optical devices used for continuous light, like beam expanders and spatial filters, may be used for ultrashort pulses, several optical devices have been specifically designed for ultrashort pulses. One of them is the pulse compressor, a device that can be used to control the spectral phase of ultrashort pulses. It is composed of a sequence of prisms, or gratings. When properly adjusted it can alter the spectral phase $f(\omega)$ of the input pulse so that the output pulse is a bandwidth-limited pulse with the shortest possible duration. A pulse shaper can be used to make more complicated alterations on both the phase and the amplitude of ultrashort pulses [4].

They are characterized by a high peak intensity (or more correctly, irradiance) that usually leads to nonlinear interactions in various materials, including air. These processes are studied in the field of nonlinear optics [5].

The word "ultrashort" refers to femtosecond (fs) or picosecond (ps) pulses, although such pulses no longer hold the record for the shortest pulses generated. Indeed, pulse durations on the attosecond time scale have been reported. The real electric field corresponding to an ultrashort pulse is oscillating at an angular frequency ω_0 corresponding to the central wavelength of the pulse [6].

The time structure of optical pulse is usually determined by the intensity $I(t)$ and the phase $j(t)$. In general case the intensity contour $I(t)$ and its spectral representation $I(\omega)$ are connected with each other due to existing dependence of the field strength on the phase $j(t)$. The only thing that one can write is the relation between the half-widths T_L and V_L of the envelopes.

$$T_L V_L \approx C_B \quad (1.1)$$

where C_B is the constant determined by the pulse shape. The shortest pulse, which can be obtained at a given V_L is spectrally (transform) limited pulse with $T_L = C_B/V_L$.

Let us consider the Gaussian pulse with the field strength

$$E(t) = E_0 \exp(-at^2 + ibt^2) \quad (1.2)$$

The term ibt^2 describes linear variation of frequency inside the pulse or the internal phase modulation, or the frequency chirp, see Fig.1.1

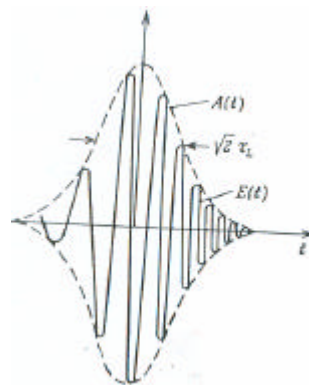


Fig 1.1 Describe linear variation of frequency inside the pulse or the internal phase modulation, or the frequency chirp.

The constant g is connected with the half-width of pulse power as

$$t_L = \frac{2 \ln 2}{\pi} \frac{g}{g} \frac{\omega}{\omega} \quad (1.3)$$

After Fourier transform Eq (1.2), one can obtain

$$Dn_L = \frac{1}{\pi} \frac{2 \ln 2}{\pi} \frac{g^2 + b^2}{g} \frac{\omega}{\omega} \quad (1.4)$$

The product of the half-widths T_L and V_L is given by

$$t_L Dn_L = \frac{2 \ln 2}{\pi} \frac{1}{\pi} + \frac{2 \ln 2}{\pi} \frac{b^2}{g^2} \frac{\omega}{\omega} \quad (1.5)$$

From equation (1.2), in the particular case of $\mathbf{b} = \mathbf{0}$ (absence of the phase modulation), one can find $C_B = 0.441$. It is seen from Eq (1.11) that with a fast phase modulation the product in the left hand side of Eq.(1.11) can be rather large, so that $\mathbf{b}/g \gg 1$. In the case of hyperbolic-secant-squared pulse (**sech** $1.76 t/T_L)^2$ one can estimate $C_B = 0.315$ [7].

1.3 Measurement techniques

Several techniques are available to measure ultrashort optical pulses:

- Intensity autocorrelation: gives the pulse width when a particular pulse shape is assumed.
- Spectral interferometry (SI): a linear technique that can be used when a pre-characterized reference pulse is available. Gives the intensity and phase. The algorithm that extracts the intensity and phase from the SI signal is direct.

- Spectral phase interferometry for direct electric-field reconstruction (SPIDER): a nonlinear self-referencing technique based on spectral shearing interferometry. The method is similar to SI, except that the reference pulse is a spectrally shifted replica of itself, allowing one to obtain the spectral intensity and phase of the probe pulse via a direct FFT filtering routine similar to SI, but which requires integration of the phase extracted from the interferogram to obtain the probe pulse phase.
- Frequency-resolved optical gating (FROG): a nonlinear technique that yields the intensity and phase of a pulse. It's just a spectrally resolved autocorrelation. The algorithm that extracts the intensity and phase from a FROG trace is iterative.
- Grating-eliminated no-nonsense observation of ultrafast incident laser light e-fields (GRENOUILLE), a simplified version of FROG [8].

1.3.1 Correlation Functions.

Nonlinear optical techniques for pulse measurement do not provide a direct display of pulse shape but give instead measurement of correlation functions. It is important therefore to consider in some detail the theoretical relationship between a signal $\mathbf{I}(\mathbf{t})$ and its correlation functions. The second-order autocorrelation function of the intensity $\mathbf{I}(\mathbf{t})$ is given in normalized form by:

$$\mathbf{G}^2(\mathbf{t}) = \frac{\langle \mathbf{I}(\mathbf{t})\mathbf{I}(\mathbf{t} + \mathbf{t}) \rangle}{\langle \mathbf{I}^2(\mathbf{t}) \rangle} \quad (1.6)$$

where the brackets indicate an average over a sufficiently long interval of time. This is the function one can obtain by Second Harmonic Generation (SHG) or Two Photon Fluorescence (TPF). If $\mathbf{I}(\mathbf{t})$ is a single isolated pulse, $\mathbf{G}^2(\mathbf{t})$ vanishes for large relative delay \mathbf{t} and its half-width provides a measure of

the duration of $\mathbf{I}(t)$. It is obvious from (1.6) that $\mathbf{G}^2(t)$ is always symmetric regardless of any asymmetric in $\mathbf{I}(t)$. This fact is the fundamental limitation on the use of $\mathbf{G}^2(t)$ to determine pulse shape. If $\mathbf{I}(t)$ were known to be symmetric, its shape could in fact be deduced from $\mathbf{G}^2(t)$.

In general, higher-order correlation functions must be used in addition to $\mathbf{G}^2(t)$ to determine $\mathbf{I}(t)$ uniquely. The n -th order correlation function is given by

$$\mathbf{G}^n(\mathbf{0}, \mathbf{0}, \dots, t) = \frac{\langle \mathbf{I}^{(n-1)}(t) \mathbf{I}(t+t) \rangle}{\langle \mathbf{I}^n(t) \rangle} \quad (1.7)$$

As the order increases, $\mathbf{I}^{n-1}(t)$ becomes a sharper function of time and therefore a better probe of the shape of $\mathbf{I}(t)$. With picosecond laser pulses, correlation functions up to order five have been obtained [9].

The relationship between $\mathbf{G}^2(t)$ and different types of optical signals is most easily illustrated with specific examples. Consider first the case where $\mathbf{I}(t)$ is a Gaussian random variable, the intensity produced by a continuous source of thermal noise. A laser operating in large number of randomly phased modes approximates such a source. The intensity can be described by

$$\mathbf{p}(\mathbf{I})d\mathbf{I} = \frac{1}{\langle \mathbf{I} \rangle} \exp(-\mathbf{I}/\langle \mathbf{I} \rangle) d\mathbf{I} \quad (1.8)$$

where $\mathbf{p}(\mathbf{I})d\mathbf{I}$ is the probability of observing the intensity \mathbf{I} in an interval $d\mathbf{I}$, and $\langle \mathbf{I} \rangle$ is the average intensity. For large t , where $\mathbf{I}(t+t)$ and $\mathbf{I}(t)$ are independent random variables yields

$$\mathbf{G}^2(t \otimes \mathbb{Y}) = \frac{\langle \mathbf{I}(t) \rangle^2}{\langle \mathbf{I}^2(t) \rangle} = \frac{1}{2} \quad (1.9)$$

Since $G^2(0)$ is by definition unity, It see that even a random signal produces a peak in its autocorrelation with $G^2(0)/G^2(\infty) = 2$. The width of this peak is a measure of the temporal coherence of the signal, and is just related to the inverse of the spectral bandwidth of the source. The only information about the actual temporal behavior is contained in the contrast ratio, $G^2(0)/G^2(\infty)$. Contrast ratios different from 2 imply some deviation from purely random behavior. Smoother signals give lower contrast and enhancement of intensity peaks increases contrast. Several higher-order correlations of Gaussian noise are also the interest. The third-order correlation function.

$$G^3(0,t) = \frac{\langle I^2(t)I(t+t) \rangle}{\langle I^3(t) \rangle} \quad (1.10)$$

has a contrast ratio of 3. With nonlinear harmonic generation followed by second-order correlation one can also measure

$$G^{2n}(0,\dots,t) = \frac{\langle I^n(t)I^n(t+t) \rangle}{\langle I^{2n}(t) \rangle} \quad (1.11)$$

which results [10,11] in a contrast ratio of $(2n)!/(n!)^2$. In the limit of the large n one obtains the contrast of a single, isolated pulse (produced by nonlinear selection of the largest noise spike in $I(t)$). The next case it consider is that of an isolated burst of Gaussian noise. This has its practical manifestation in a laser that is partially modelocked [12]. It is described by $I(t) = I_1(t) \times I_2(t)$ where $I_1(t)$ is a random variable as above and $I_2(t)$ is a more slowly varying envelope function. It can be shown [13] that

$$G^2(t) = G_1^2(t) \times G_2^2(t) \quad (1.12)$$

where $G_1^2(t)$ and $G_2^2(t)$ are the autocorrelation functions of $I_1(t)$ and $I_2(t)$, respectively. From an initial ($t = 0$) value of 1, $G^2(t)$ falls to value of $(1/2)G_2^2(t)$ for t longer than the coherence time of the random variable $I_1(t)$ and then to zero as $G_2^2(t) \gg \langle I_2(t)I_2(t+t) \rangle \approx 0$. In this case the temporal isolation produced by the envelope of the signal results in a high contrast ratio overall. The contrast between noise and envelope contributions is unity. A careful determination of $G^2(t)$ yields information about the envelope of the signal as well as its coherence. Note that higher-order correlations of a noise burst tend to accentuate the relative amplitude of the coherence spike [14]. It should be mentioned that in the case of an isolated pulse of noise, the actual shape of the correlation function may differ from the expectation value. Examples of such deviations are found in [15-18].

The second-order correlations expected from these different types of optical intensity signals are given in Fig 1.2.

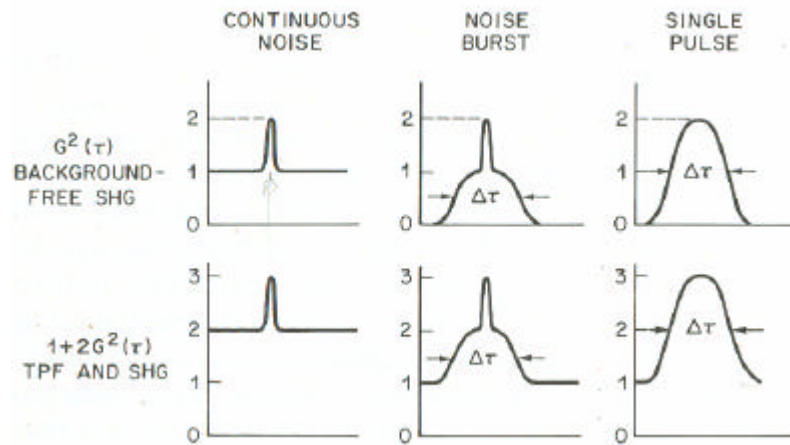


Figure 1.2 Theoretical correlation traces for SHG and TPF measurements.

For comparison with experiment, the form measured in SHG and TPF experiments with inherent background are also shown. Higher-order correlation measurements produce similar shapes but with

different contrast ratios. It is common in the literature to estimate the duration of a pulse Δt by simply measuring the width $\Delta \nu$ of that part of the correlation due to pulse envelope. Of course the actual $\Delta t / \Delta \nu$ depends upon the precise pulse shape, but the uncertainty in such an estimate can be decreased than a factor two.

Table 1.1 gives $\Delta t / \Delta \nu$ for several theoretical pulse shapes. Also shown for each case is the predicted spectral width. Comparison of experimental bandwidth with the predicted width is an important test of the assumed pulse shape. It is interesting to note that the Gaussian pulse envelope which is known to have the minimum time-bandwidth uncertainty product does not have the minimum half-width product. The Lorentzian intensity profile $I(\nu) = \frac{1}{\nu^2 + \nu_c^2}$ without chirp has a singular spectrum [19]. If the measured bandwidth is much greater than that expected for a reasonable pulse shape, two possible causes are apparent. Either the experiment has not resolved the noise correlation spike indicative of amplitude substructure, or the actual pulse contains frequency modulation which does not show up in a correlation measurement [20]. If a frequency sweep is present, it is possible to compress the pulse in time.




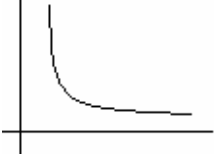
$I(t)$	Dt/Dt	$Dt Du$	
$1(0 \leq t \leq Dt)$	1	0.886	
$\exp\left\{-\frac{(4 \ln 2)t^2}{Dt^2}\right\}$	$\sqrt{2}$	0.441	
$\text{sech}^2\left\{\frac{1.76t}{Dt}\right\}$	1.55	0.315	
$\exp\left\{-\frac{(\ln 2)t}{Dt}\right\} (t \geq 0)$	2	0.11	

Table 1.1 Correlation widths and spectral bandwidths for four different transform-limited pulse shapes.

An important point is that correlation measurements are not particularly sensitive to low-level background signals which may be present in have been necessary to estimate the fraction of the total energy contained in the short-pulse component [21-23].

1.3.2 Correlation methods

The initial signal $S(t)$ is applied to the input port 1 of a multiplier playing the role of a nonlinear element. The input port 2 is activated by either the additional signal $H(t)$ or the initial signal $S(t)$, but they both have some temporal shift τ due to passing through the delay line V and take the forms of $H(t+\tau)$ and $S(t+\tau)$, respectively.

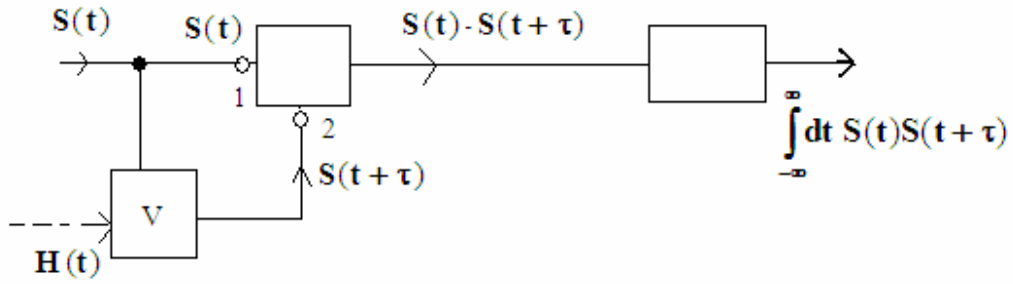


Figure 1.3 Illustrate the set-up for shaping both cross-correlation and auto-correlation functions.

The product of a pair of the input signals is integrated with respect of time by the integrator **J**. Thus, for example, the auto-correlation function is given by

$$G(t) = \int_{-\infty}^{\infty} dt S(t)S(t+t), \quad K(t) = \int_{-\infty}^{\infty} dt S(t)H(t+t). \quad (1.13)$$

This formula represents the auto-correlation function of the second order. Under some additional conditions, but definitely not always, the availability of the function $G(t)$ makes it possible to identify the time dependence of the input signal $S(t)$. For, example, if it is known that the signal has the Gaussian shape

$$S(t) = S_0 \exp\{-4(\ln 2)(t/t_s)^2\} \quad (1.14)$$

the half-width t_s of this incoming pulse is connected with the half-width t_A of the corresponding auto-correlation function as

$$t_s = \frac{1}{\sqrt{2}} t_A \quad (1.15)$$

In the case, when $H(t)$ is extremely short pulse, which can be approximated by the Dirac δ -function,

and the integral of the function $H(t)$ is normalized to unity, i.e. $\int_{-\infty}^{\infty} dt H(t) = 1$, one can find that $K(t) =$

$S(t)$.

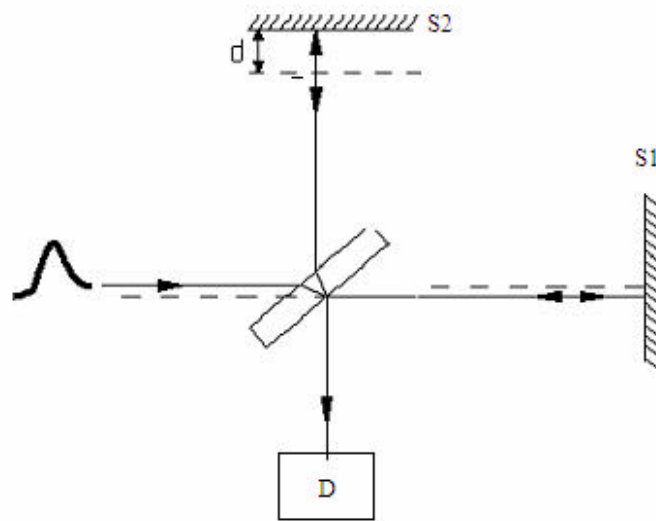


Figure 1.4 Exploiting a two-beam Michelson interferometer as the correlator of the field strength. Two fields $E_1(t) = E(t)$ and $E_2(t) = E(t+T)$ related to the signals reflected from the mirrors S1 and S2 are summarized in the detector D. The delay time T from pulse to pulse can be varied by shifting the mirror S2. The output signal is proportional to the energy on the detector D under condition that the time of integration is long enough. This energy is proportional to the value: $\int_{-\infty}^{\infty} dt (\mathbf{E}_1 + \mathbf{E}_2)^2 \gg [G_E(0) + G_E(t)]$, where

$$G_E(t) = \int_{-\infty}^{\infty} dt E(t)E(t+t) = \frac{1}{2\pi} \int_{-\infty}^{\infty} d\omega |E(\omega)|^2 e^{-i\omega t} \quad (\text{the second formula is the auto-correlation function of the field strength.})$$

The simplest optic auto-correlator is a two-beam scanning Michelson interferometer with a photo-detector and non-linear medium, see Fig. 1.4. It makes it possible to detect the auto-correlation function for the light field strength and, after conversion, the Fourier spectral density of light radiation, which is proportional to $|E(\omega)|^2$, and find the spectral width of radiation.

However, during such a measurement (as well as with exploiting another Fourier spectrometers) the information about the phase of the field $E(\omega)$ becomes lost. That is why one cannot correct (unambiguously) conclusion about the pulse width. The pulse width can be determined from the spectral width rather accurately only if it is known in advance that that optical pulse is spectrally

(transform) limited, i.e. does not include any internal frequency modulation. This takes place when the phase of field strength along the pulse width grows linearly, so that only the shape of pulse envelope determines the spectrum width. The half-width $D\omega$ of the spectrum of power density for spectrally limited pulses and the half-width t_L for the dependence of power on time inherent in the spectrally (transform) limited pulses are connected by

$$\frac{D\omega}{2\pi} t_L = C_B \quad (1.16)$$

where C_B is the constant determined by the pulse shape. In general case, when pulse is not transform limited, the left hand side of Eq.(1.16) exceeds C_B . To determine the pulse width, one needs two independent measures of the spectrum width and the internal frequency modulation.

Now on the case of Second harmonic generation, picosecond optical pulses provide a unique means for studying ultrafast processes associated with the interaction of light with matter. Implementation of these studies has required the development of new measurement techniques capable of picosecond time resolution. It described the various methods that are now available for characterizing picosecond laser pulses and for detecting rapid events created by them.

The emphasis here is on the relative advantages and limitations of the techniques themselves and less on the results of particular experiments. An understanding of these techniques is necessary for proper evaluation of any picosecond experiment. Many inconsistencies in early work have been due not to the variability of pulsed laser sources but to improper interpretation of experimental results. As the various pitfalls of picosecond measurement become better understood, experimental studies become more reliable. At the same time, a better understanding of ultrafast process will undoubtedly lead to new and better measurement techniques.

1.3.3 Pulsewidth measurements.

The invention of the passively modelocked Nd: glass laser in 1965 [24] provided a pressing need for new techniques to measure the duration of ultrashort optical pulses. Direct measurement by the combined use of the photodetectors and oscilloscopes was no longer adequate to temporally resolve the pulses being produced. Within a year, however, an indirect technique with subpicosecond time resolution had been proposed and demonstrated. This technique, based on the nonlinear process of second-harmonic generation (SHG), is illustrated diagrammatically in Fig 1.5.

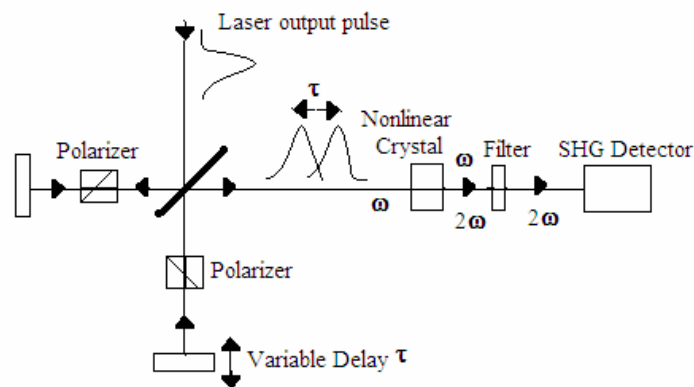


Figure 1.5 Interferometric arrangement for pulse correlation measurement by SHG.

The optical pulse is divided into two beams which travel different paths before being recombined in a nonlinear crystal. By polarizing the two beams differently [25,26] or by making them noncollinear [27], it can be arranged that no SHG is detected when either beam is blocked or when the two pulses arrive at the crystal at sufficiently different times. Temporal overlap of the two pulses at the crystal can be varied by mechanically changing one of the path lengths. The amount of SHG detected is a maximum when the pulses are coincident and decreases as one is delayed with respect to the other.

The primary experimental difficulty in using the SHG, method in conjunction with pulsed lasers is that it requires plotting the pulse correlation point by point with successive firings of the laser. Although the development of cw modelocked lasers has greatly revived interest in this technique, its use with pulse lasers was effectively ended within one year by the invention of the two-photon-fluorescence (TPF) method [28]. The TPF technique in its most commonly used form is illustrated in Fig 1.6.

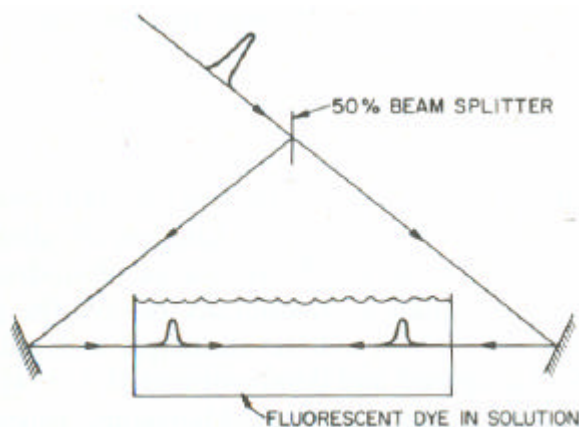


Figure 1.6 Triangular arrangements for TFP.

An input pulse is divided into two beams which then travel in opposite directions in an organic dye solution. Fluorescence from the dye is proportional to two-photon absorption which is a maximum at the point where the two pulses are coincident in time. With this scheme a single photograph of the fluorescence track provides a TPF measurement of pulse correlation. If carefully performed, SHG and TFP measurement can provide a reliable estimate of pulse duration. A critical review of the use of both techniques is given below. They do not give a direct display of the pulse shape. It has been necessary to use different techniques to determine such pulse characteristics as temporal asymmetry and dynamic spectral behavior [29].

1.4 Phase matching

The above ignores the position dependence of the electrical fields. In a typical situation, the electrical fields are traveling waves described by

$$\mathbf{E}_j(\mathbf{x}, t) = \exp[i(\omega_j t - \mathbf{k}_j \cdot \mathbf{x})] \quad (1.17)$$

at position \mathbf{x} , with the wave vector $\mathbf{k}_j = n(\omega_j) \omega_j / c$, where c is the velocity of light and $n(\omega_j)$ the index of refraction of the medium at angular frequency ω_j . Thus, the second-order polarization angular frequency ω_3 is

$$\mathbf{P}^{(2)}(\mathbf{x}, t) \propto \mathbf{E}_1^{n_1} \mathbf{E}_2^{n_2} \exp[i(\omega_3 t - (\mathbf{m}_1 \mathbf{k}_1 + \mathbf{m}_2 \mathbf{k}_2) \cdot \mathbf{x})] \quad (1.18)$$

At each position \mathbf{x} , the oscillating second-order polarization radiates at angular frequency ω_3 and a corresponding wave vector $\mathbf{k}_3 = n(\omega_3) \omega_3 / c$. Constructive interference, and therefore a high intensity ω_3 field, will occur only if

$$\mathbf{k}_3 = \mathbf{m}_1 \mathbf{k}_1 + \mathbf{m}_2 \mathbf{k}_2 \quad (1.19)$$

The above equation is known as the *phase matching condition*. Typically, three-wave mixing is done in a birefringent crystalline material (v.e, the refractive index depends on the polarization and direction of the light that passes through.), where the polarizations of the fields and the orientation of the crystal are chosen such that the phase-matching condition is fulfilled. Typically a crystal has three axes, one of which has a different refractive index than the other ones. This axis is called the extraordinary (e) axis, while the other two are ordinary axes (o). There are several schemes of choosing the polarizations. If the signal and idler have the same polarization, it is called "Type-I phase-matching", and if their polarizations are perpendicular, it is called "Type-II phase-matching". However, other conventions exist that specify further which frequency has what polarization relative to the crystal axis. These types

are listed below, with the convention that the signal wavelength is shorter than the idler wavelength [30].

To obtain, the intensity of the correlation, a photodetector is used, whose responsivity has to be know. In order to determine this feature, experimental tests to obtain the reflectance and quantum internal efficiency of Silicon and InGaAs/InP photodetectors were realized.

1. 5 Silicon photodiodes

The photodetectors are sensors of light or other electromagnetic energy. A photodiode is a type of photodetector capable of converting light into either current or voltage, depending upon the mode of operation.

Photodiodes are similar to regular semiconductor diodes except that they may be either exposed (to detect vacuum UV or X-rays) or packaged with a window or optical fibre connection to allow light to reach the sensitive part of the device [31].

An understanding of the diode structure, in particular the behaviour of the depletion layer, is required to make the best use of a silicon photodiode in any given application. The junction region is produced by diffusion or ion implantation of boron into selected areas of the surface of a high resistivity n-type silicon wafer. The geometry of this is accurately defined by a silicon dioxide layer having windows etched in it using standard photolithographic techniques. A heavily doped n-type layer is introduced

into the rear face when the device is to be operated in the fully depleted mode, which will be described later.

A silicon nitride passivation layer is deposited onto the front face, the thickness being chosen so that the layer acts as an antireflection coating for the wavelength of operation. The front contact is normally by means of a photolithographically defined aluminium layer and the rear contact is by means of one of a number of alternative multilayer metallisations.

Between the p-type region and the lightly doped n-type region there is a depletion region which is free from mobile charges. The width of this region depends upon the resistivity of the silicon and the applied voltage; even with no externally applied bias the diffusion of electrons and holes across the junction creates a depletion region with an electric field across it which is known as the "built-in" field.

When a photon is absorbed in a semiconductor an electron-hole pair is formed. Photocurrent results when photon-generated electron-hole pairs are separated, electrons passing to the n-region and holes to the p-region. Alternatively, holes and electrons may recombine, thereby causing no charge displacement and thus no contribution to photocurrent. There is a greater probability of separation of a photon-generated electron-hole pair when it is formed within the depletion region where the strongest electric field exists.

The primary parameter defining the sensitivity of a photodiode is its quantum efficiency, (QE) which is defined as the percentage of incident photons generating electron-hole pairs which subsequently contribute to the output signal. Quantum efficiencies in the region of 80% are usual for silicon detectors operating at wavelengths in the 800-900 nm region.

The sensitivity of a photodiode may also be expressed in practical units of amps of photodiode current per watt of incident illumination. This parameter, usually known as responsivity (R), may be derived by multiplying the Q.E. by the electronic charge (e) and dividing by the photon energy for a particular wavelength [32].

1.6 InGaAs/InP Photodiodes.

These photodetectors are chosen as the first device of interest because of their simple structure, and since their analysis is a natural extension, almost an example, of our discussion of p-n diodes. Whereas the field of photodetectors goes far beyond that of semiconductor photodetectors, we restrict ourselves here to such devices. It will be discussed p-i-n diodes, which are also referred to as photovoltaic detectors, photoconductors or solar cells photodetectors. The distinction between the different devices is somewhat artificial since many similarities exist between these devices but it enables to clearly separate the difference in structure, principle of operation and purpose of the devices [33].

Semiconductor photodetectors based on InP materials are the ones most often used in state of the art long wavelength optical fiber communication system. Mixed compounds such as InGaAs (P) and In(Al)GaAs lattice matched to InP are the materials responsible for detecting long wavelength light, specially the nondispersion wavelength (1.3 μm) and loss minimum wavelength (1.55 μm) of silica optical fibers. The characteristics of these InP-based photodetectors are superior to those of conventional photodiodes composed of elemental Ge, which was the only material applicable for wavelengths below 1.55 μm . By using a heterostructure, which hadn't been expected in group IV elemental semiconductors such as Si and Ge, new concepts and new designs for high performance photodetectors

have been developed. For example, the absorption region can be confined to a limited layer and the InP wide bandgap layer can serve as a transparent layer for specific communication wavelength. Recently InGaAs/InP avalanche photodiodes (APDs) with a SAM (separation of absorption and multiplication) configuration have become commercially available. The SAM configuration is thought to be necessary for high performance APDs utilizing long wavelengths.

Because photodiodes may be operated under reverse bias, high quality semiconductor layers need to be produced. To obtain photodiodes that operate at a low bias and have a low dark current, it is necessary to produce epitaxial layers that are pure and have few defects (such as dislocations, point defects, and impurity precipitates). To get stable and uniform gain in APDs, in which internal gain is achieved through the carrier avalanche process, the layers in the avalanche region must be uniform and free of dislocations. Furthermore, a planar device structure requires that a guard ring be used to keep the electric field around the photoreceptive area from increasing too much. Fabrication and processing technologies such as impurity diffusion, ion implantation, and passivation will also play important roles in the production of reliable photodetectors [34].

From a radiometric point of view, the photodetectors important characteristics are: Speed of (characterized by the bandwidth of the frequency response or the Full Width Half Maximum (FWHM) of the pulse response), responsivity (determined as the ratio of current out the detector to the incident optical power on the device), sensitivity (defined as the minimal input power that can still be detected which, as a first approximation, is defined as the optical power which generates an electrical signal equal to that due to noise of the diode).

When the light radiation impinges on a detector, various physical processes occur; part of the incident light is reflected by the sensitive surface, while the rest passes inside the detector, where can be partially, because of losses due to absorption, converted into an electronic signal. The response of each photodetector is conditioned by a quantity of the converted light power, but for evaluating the incident power one has to know the ratios of the reflected, absorbed, and converted portions.

An InGaAs/InP-photodetector is a photodiode based on a p-n or hetero-structure. There is a region, which can be denominated as the depleted or exhausted region, where an electric field sweeps the generated charge carriers and produces an external electrical current. In addition charge generated outside that region also contributes to the photocurrent. Thus, the total photodiode response I can be written as

$$I = \frac{e}{e} [1 - r(\lambda)] \eta \frac{1}{e} \frac{1}{hc} \lambda f \quad (1.20)$$

where η is the internal quantum efficiency, which indicates the number of electrons produced by each absorbed photon, e is the electron charge, h is the Planck constant, c is the velocity of light, f is the radiant flux, λ is the wavelength and $r(\lambda)$ is the photodiode's reflectance. From equation (1.20), the responsivity R can be obtained as:

$$R = \frac{I}{f} = [1 - r(\lambda)] \eta \frac{1}{e} \frac{1}{hc} \lambda \quad (1.21)$$

This equation shows that the responsivity depends on the wavelength of the incident light by three ways, directly, via the reflectance of the surface, and through the quantum efficiency. This equation indicates also, that the responsivity will be known if both the reflectance and the internal quantum

efficiency are known at every wavelength and is the quantity usually measured. It is seen from equation (1.21) that the photodiode response depends on a set of parameters inherent in the incident light like the spectral distribution, polarization, modulation frequency, angle of incidence, and radiant power. Furthermore, the response is determined by photodetectors features such as the material refractive index and the structure of diode as well as by some environmental factors, such as temperature, for example [35].

1.7 Formulation of the problems.

The problems to be resolved in this thesis are:

- The characterization of low-power bright picosecond optical pulses with an internal frequency modulation simultaneously in both time and frequency domains in the case of the Gaussian shape. This approach exploits the Wigner time-frequency distribution, which can be found for these bright pulses by using a novel interferometric technique.
- The characterization of low-power bright ultrashort optical pulses with an internal frequency modulation simultaneously in both time and frequency domains. The analysis and computer simulations are applied to studying the capability of Wigner distribution to characterize solitary pulses in practically important case of the sech-pulses.
- Measuring the train-averaged parameters of picosecond optical pulses with both symmetric and asymmetric envelopes being arranged in high-frequency repetition trains and corrupted by additive

Gaussian noise. In so doing, one can exploit the temporal triple auto-correlation function, whose Fourier transformation gives the bispectrum of signal.

- Determining the spectral responsivity from the reflectance and the internal quantum efficiency at the near infrared range for InGaAs/InP photodiodes, and measuring the reflectance of silicon photodiodes in visible range that were used to maintain the scale of the spectral responsivity.

1.8 References

- [1] F. Krausz et al., “Femtosecond solid-state lasers”, *IEEE J. Quantum Electron.* **28** (10), 2097, (1992).
- [2] Ch. Spielmann, “Ultrabroadband femtosecond lasers”, *IEEE J. Quantum Electron.* **30** (4), 1100, (1994).
- [3] S. Arahira et al., “Mode-locking at very high repetition rates more than terahertz in passively mode-locked distributed-Bragg-reflector laser diodes”, *IEEE J. Quantum Electron.* **32**, 1211 (1996).
- [4] U. Morgner et al., “Sub-two cycle pulses from a Kerr-lens mode-locked Ti:sapphire laser”, *Opt. Lett.* **24** (6), 411, (1999).
- [5] D. H. Sutter et al., “Semiconductor saturable-absorber mirror-assisted Kerr lens modelocked Ti:sapphire laser producing pulses in the two-cycle regime”, *Opt. Lett.* **24** (9), 631, (1999).
- [6] C. Hönniger et al., “Ultrafast ytterbium-doped bulk lasers and laser amplifiers”, *Appl. Phys. B* **69** (1), 3 (1999).
- [7] J. Herrmann and B. Wilhelmi. *Laser für Ultrakurze Lichtimpulse*. (Akademi-Verlag, Berlin, (1984).
- [8] R. Paschotta et al., “Progress on all-solid-state passively mode-locked ps and fs lasers”, *Proc. SPIE* 3616, 2, (1999).

- [9] E. Sorokin et al., “Diode-pumped ultra-short-pulse solid-state lasers”, *Appl. Phys. B* **72**, 3 (2001).
- [10] L. Krainer et al., “Compact Nd:YVO₄ lasers with pulse repetition rates up to 160GHz”, *IEEE J. Quantum Electron.* **38** (10), 1331 (2002).
- [11] E. Innerhofer et al., “60W average power in 810-fs pulses from a thin-disk Yb:YAG laser”, *Opt. Lett.* **28** (5), 367 (2003).
- [12] U. Keller, “Recent developments in compact ultrafast lasers”, *Nature* **424**, 831 (2003).
- [13] A. Fernandez et al., “Chirped-pulse oscillators: a route to high-power femtosecond pulses without external amplification”, *Opt. Lett.* **29** (12), 1366 (2004).
- [14] R. Paschotta and U. Keller, “Passively mode-locked solid-state lasers”, in *Solid-State Lasers and Applications* (ed. A. Sennaroglu), CRC Press, Boca Raton, FL (2007), Chapter 7, pp. 259–318.
- [15] D. Dragoman, “Phase space interference as the source of negative values of the Wigner distribution function,” *Journal of the Optical Society of America A*, **17**, 12, 2481–2485, (2000).
- [16] Euisuk Kim, Hyoungjoo Kim & Jaewoo Noh Measurement of the Spatial Wigner Distribution Function of Laser Light by Using a Sagnac Interferometer *Journal of the Korean Physical Society*, **46**, No. 6, pp. 1342-1346 , (2005).
- [17] D. Dragoman, "Applications of the Wigner distribution function in signal processing," *EURASIP Journal on Applied Signal Processing*, **10**, pp. 1520-1534, (2005).
- [18] E.P.Ippen and C.V.Schenk, “Picosecond Techniques and Applications.” in *Ultrashort Light Pulses*, Ed. by S.Shapiro (Springer, Heidelberg, 1977).
- [19] L. Cohen, “Time-frequency distributions—a review,” *Proc.IEEE*, vol. 77, no. 7, pp. 941–981, 1989.
- [20] D. Dragoman and M. Dragoman, “Quantum coherent versus classical coherent light,” *Optical and Quantum Electronics*, **33**, 3, pp. 239–252, 2001.

- [21] Eran Mukamel, Konrad Banaszek & Ian Walmsley, “Direct measurement of the spatial Wigner function with area-integrated detection”, *Optics Letters*, **28**, pp 1317-1319, (2003).
- [22] S. C. Zeller et al., “Passively mode-locked 50-GHz Er:Yb:glass laser”, *Electron. Lett.* **40** (14), pp. 875-880 (2004)
- [23] R. Paschotta et al., “Picosecond pulse sources with multi-GHz repetition rates and high output power”, *New J. Phys.* **6**, 174, (2004)
- [24] A.J. De Maria, D.A. Stetser, H. Heynau, “Self Mode Locking of lasers with saturable absorbers”, *Applied Physics Letters* **8**, pp.174, (1966).
- [25] H.P. Weber, “Method for pulsewidth measurement of ultrashort light pulses generated by phase-locked lasers using nonlinear optics”, *Journal Applied Physics*, **38**, pp. 2231,(1967)
- [26] J.A. Armstrong, “Measurement of picosecond laser pulse widths”, *Appl.Phys.Lett*, **10** pp.16-23,(1967).
- [27] E. Sorokin et al., “Ultrabroadband infrared solid-state lasers”, *IEEE J. Sel. Top. Quantum Electron.* **11** (3), 690, (2005)
- [28] S. V. Marchese et al., “Femtosecond thin disk laser oscillator with pulse energy beyond the 10-microjoule level”, *Opt. Express* **16** (9), 6397, (2008)
- [29]. R Kakarala. Triple correlation on groups. Ph.D. Thesis University of California Irvine (1992).
- [30] D.J. Kame and R. Trebino. “Single-shot measurement of the intensity and phase of a femtosecond laser pulse.” *Proc. SPIE*, vol.1861, 150-160 (1993).
- [31] Y. Takanashi, M. Kawashima, and Y. Horikoshi, “Required donor concentration of epitaxial layers for efficient InGaAsP avalanche photodiodes”, *Journal Applied Physics*, **19**, 693-701, (1980).
- [32] E.F. Zalewski, J. Geist “Silicon photodiode absolute spectral response self-calibration”, *Applied Optics*, **19** (8), pp. 1214-1216, (1980).

- [33] E.L Dereniak and G.D.Boreman, “Infrared detectors and systems”, Wiley series in pure and applied optics, John Wiley, (1996).
- [34] O.Wada and H.Hasegawa , “InP-Based materials and devices physics and technology” John Wiley, (1999).
- [35] J.Campos, P. Corredera, A. Pons, A. Corróns J. L. Fontecha. “Reflectance dependencies of silicon trap detectors”. ,IOP Metrología, **35**, 455-460,(1998).

CHAPTER 2

DETERMINING THE TIME-FREQUENCY PARAMETERS OF LOW-POWER BRIGHT PICOSECOND OPTICAL PULSES WITH GAUSSIAN SHAPE.

Although the Wigner distribution is mainly used for characterizing optical beams and pulses that propagate through linear media, some studies have also focused on nonlinear propagation [1,2].

When the spectrum of signal varying in time is the subject of interest, it is worthwhile to apply the joint function of the time and frequency, which would be able to describe the intensity distribution of this signal simultaneously in time domain as well as in frequency one.

Such a distribution gives us opportunities for determining a relative part of energy at a given frequency in the required temporal interval or for finding the frequency distribution at a given instant of time. The method of deriving the time frequency distribution can be based on usage of the corresponding characteristic function [3].

The joint Wigner time-frequency distribution, which can be determined and developed for these bright optical pulses by using a novel interferometric technique under our proposal.

Either power or spectral densities inherent in such pulses can be obtained through integration the Wigner distribution with respect to the corresponding conjugate variable [4]. Many techniques of investigation about of evolving the optical solitons in active and passive waveguide structures [5]. However, in many cases, the information on the average field phase is lost and it is impossible to determine the time variation of the field amplitude.

Exact determination of the train-average pulse duration from the width of the radiation spectrum is only possible when the shape of pulse envelope is known a priori and, in addition, the pulse spectrum is limited.

Here, it demonstrates an opportunity of providing experimental conditions, under which the train-average auto-correlation function of the field strength can serve as a source of exact and reliable information on the average values of both duration and frequency chirp of a low-power optical pulses traveling in high-repetition-rate trains [6,7]. It proceeds from the assumption that all pulses in a train are identical pulses with a sech function, the analysis and computer simulations are applied to studying the capability of Wigner distribution.

2.1 The Wigner time-frequency distribution for the Gaussian pulse with $T = 1$, and the varying parameter b .

The complex amplitude of a solitary optical pulse with Gaussian shape of envelope can be written as:

$$A_G(t) = \exp \left[-\frac{(1+ib)t^2}{2T^2} \right], \quad (2.1)$$

where T is the Gaussian pulse half-width measured at a level of $1/e$ for the intensity contour and b is the parameter of the frequency modulation.

In this case, the joint Wigner time-frequency distribution, see Eq.(A13), is given by

$$W_G(t, \mathbf{w}) = \frac{T}{\sqrt{\mathbf{p}}} \exp \left[-\frac{t^2}{T^2} - \left(\mathbf{w}T + \frac{bt}{T} \right)^2 \right]. \quad (2.2)$$

The Wigner distribution for the Gaussian pulse is positive-valued. When $T = 1$ and $b = 0$, Eq.(2.2) gives the distribution, which is symmetrical relative to repositioning the variables t and \mathbf{w} .

With decreasing the parameter b , the energy distribution concentrates in a bandwidth corresponding the chirp-free spectrum whose center lies along the line $\mathbf{w} = bt/T^2$.

A few examples of the time-frequency distribution $W_G(t, \mathbf{w}) = \mathbf{p}^{-1/2} \exp \left[-t^2 - (\mathbf{w} + bt)^2 \right]$, defined by Eq.(2.2) with $T = 1$ are presented in Fig.2.1.

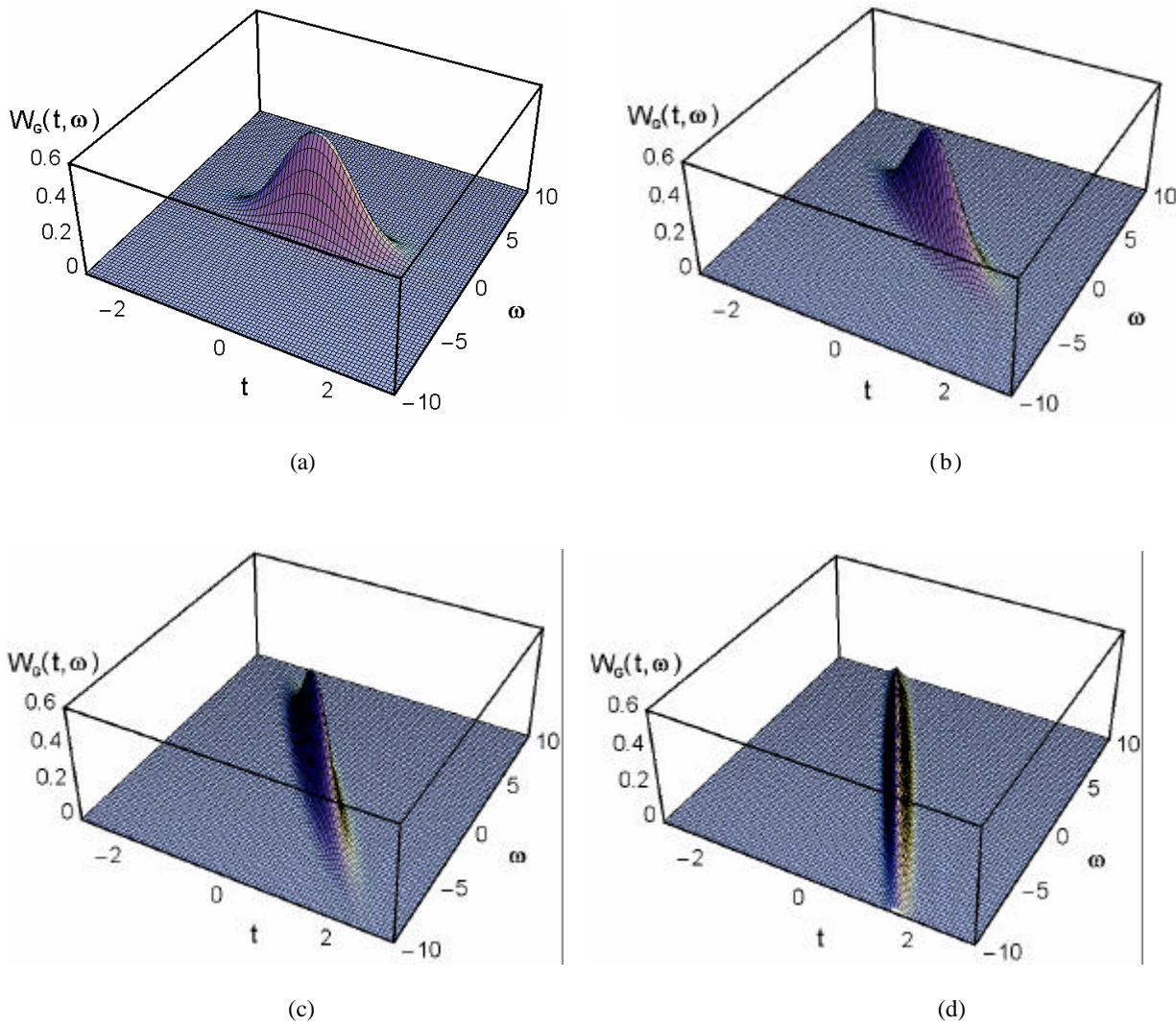


Figure 2.1. The Wigner time-frequency distribution for the Gaussian pulse with $T = 1$ and the varying parameter b : (a) $b = 0$, (b) $b = 2$, (c) $b = 4$, and (d) $b = 6$.

Integrations in Eqs.(A15) give the partial one-dimensional Wigner distributions for the Gaussian pulse over the time or frequency separately

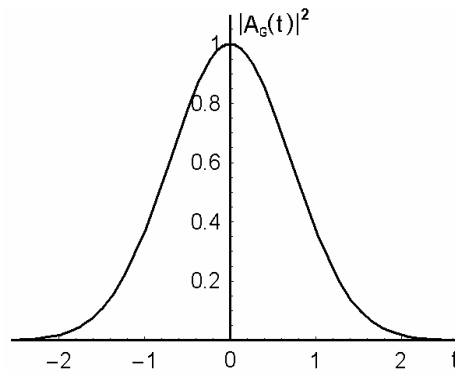
$$|A_G(t)|^2 = \int_{-\infty}^{\infty} W_G(t, \mathbf{w}) d\mathbf{w} = \exp\left(-\frac{t^2}{T^2}\right) \quad (2.3)$$

$$|S_G(\mathbf{w})|^2 = \int_{-\infty}^{\infty} W_G(t, \mathbf{w}) dt = \frac{T^2}{\sqrt{1+b^2}} \exp\left(-\frac{T^2 \mathbf{w}^2}{1+b^2}\right) \quad (2.4)$$

It is seen from Eq.(2.4) that to reach a level of $1/e$ one need vary the variable \mathbf{w} from $-T^{-1}\sqrt{1+b^2}$ to $T^{-1}\sqrt{1+b^2}$, so that the variation $D\mathbf{w} = T^{-1}\sqrt{1+b^2}$ means actually the half-width of the spectral contour at a level of e^{-1} . Thus, one can determine the product

$$D\mathbf{w} T = \sqrt{1+b^2} \quad (2.5)$$

In the particular case of $b = 0$ (i.e. in the absence of the frequency chirp or the phase modulation), one yields $D\mathbf{w} T = 1$ for the Gaussian pulse. Nevertheless, in general case, $b \gg 1$, so the product $D\mathbf{w} T$ can far exceed unity. A few examples of the time and frequency distributions, determined by Eqs.(2.3) and (2.4) with $T = 1$ are shown in Fig.2.2



(a)

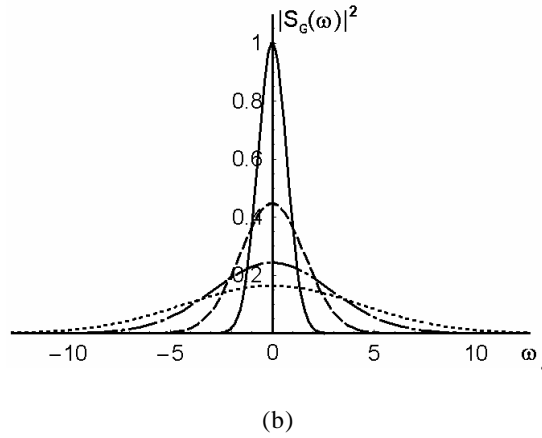


Figure 2.2. The Gaussian pulse with $T = 1$: the power density profile (a) and the spectral density profiles (b) with the varying parameter of the frequency chirp: solid line for $b = 0$, dashed line for $b = 2$, dash-dotted line for $b = 4$, and dotted line for $b = 6$.

2.2 The gaussian pulse with a high-frequency filling.

Now, one can take the case of Gaussian pulse with the slowly varying amplitude and with a high-frequency filling by the optical carrier frequency $\omega \gg 1$:

$$U(t) = \exp\left(-\frac{t^2}{2T^2}\right) \cos\left(\omega t + \frac{bt^2}{2T^2}\right). \quad (2.6)$$

The corresponding intensity distribution, instead of a smooth contour described by Eq.(2.3) for $I(t) = |A_g(t)|^2$, includes now some oscillations and is given by:

$$J(t) = |U(t)|^2 = \exp\left(-\frac{t^2}{T^2}\right) \cos^2\left(\omega t + \frac{bt^2}{2T^2}\right), \quad (2.7)$$

The smooth contours $I(t)$ and the oscillating distributions $J(t)$ are shown in Fig.2.3. One can see from Fig.2.3. that the half width has the same value T for these two plots.

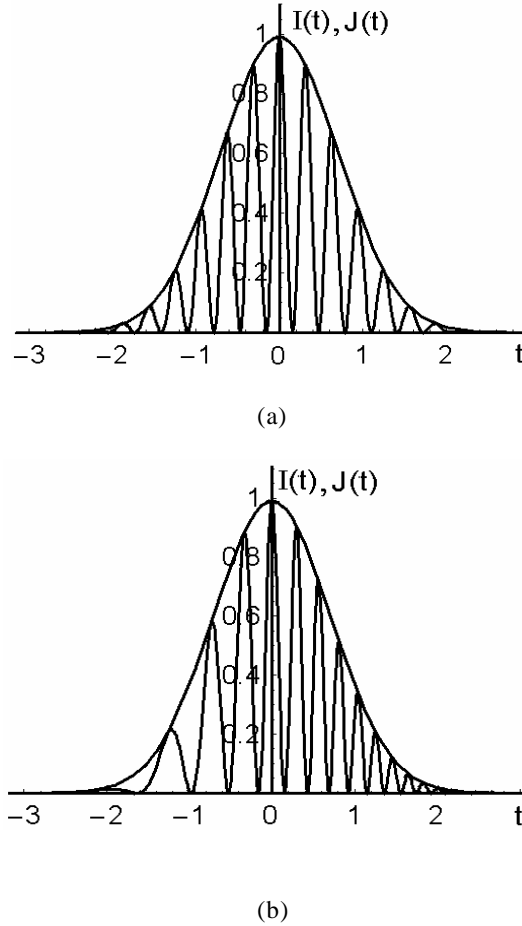


Figure 2.3. The plots of $I(t)$ and $J(t)$ with : (a) $b=0, T=1, \Omega=10$; (b) $b=4, T=1, \Omega=10$.

Then, one can consider the complex spectrum contour. Performing the Fourier transform of Eq.(2.6), one can find

$$B(\omega) = T \sqrt{\frac{p}{2}} \left\{ \frac{I}{\sqrt{I-ib}} \exp \left[-\frac{T^2 (\omega + W)^2}{2(I-ib)} \right] + \frac{I}{\sqrt{I+ib}} \exp \left[-\frac{T^2 (\omega - W)^2}{2(I+ib)} \right] \right\}. \quad (2.8)$$

The spectral intensity contour is now given by the following expression

$$J(\omega) = |B(\omega)|^2 =$$

$$\begin{aligned}
&= T^2 \frac{p}{2} \left\{ \frac{1}{\sqrt{1-ib}} \exp \left[-\frac{T^2 (\mathbf{w} + \mathbf{W})^2}{2(1-ib)} \right] + \frac{1}{\sqrt{1+ib}} \exp \left[-\frac{T^2 (\mathbf{w} - \mathbf{W})^2}{2(1+ib)} \right] \right\} \times \\
&\frac{1}{\sqrt{1-ib}} \exp \left[-\frac{T^2 (\mathbf{w} - \mathbf{W})^2}{2(1-ib)} \right] \left\{ \frac{1}{\sqrt{1+ib}} \exp \left[-\frac{T^2 (\mathbf{w} + \mathbf{W})^2}{2(1+ib)} \right] \right\} +, \quad (2.9)
\end{aligned}$$

This expression has real form

$$\begin{aligned}
J(\mathbf{w}) = |B(\mathbf{w})|^2 &= \frac{pT^2}{2} \left\{ \frac{1}{\sqrt{1+b^2}} \exp \left[-\frac{T^2 (\mathbf{w} - \mathbf{W})^2}{1+b^2} \right] + \frac{1}{\sqrt{1+b^2}} \exp \left[-\frac{T^2 (\mathbf{w} + \mathbf{W})^2}{1+b^2} \right] \right\} + \\
&+ \left(\frac{2}{1+b^2} \exp \left[-\frac{T^2 (\mathbf{w}^2 + \mathbf{W}^2)}{1+b^2} \right] \left\{ \cos \left[\frac{bT^2 (\mathbf{w}^2 + \mathbf{W}^2)}{1+b^2} \right] - b \sin \left[\frac{bT^2 (\mathbf{w}^2 + \mathbf{W}^2)}{1+b^2} \right] \right\} \right) \cdot \quad (2.10)
\end{aligned}$$

Now, one can consider the case of $\mathbf{w} \approx \mathbf{W}$ with $\mathbf{w} \gg 1$. In this case, $(\mathbf{w} + \mathbf{W})^2 \gg (\mathbf{w} - \mathbf{W})^2$ and $(\mathbf{w}^2 + \mathbf{W}^2) \gg (\mathbf{w} - \mathbf{W})^2$, so that Eq.(2.8) give

$$B(\mathbf{w}) \approx T \sqrt{\frac{p}{2(1+ib)}} \exp \left[-\frac{T^2 (\mathbf{w} - \mathbf{W})^2}{2(1+ib)} \right],$$

and

$$B^*(\mathbf{w}) \approx T \sqrt{\frac{p}{2(1-ib)}} \exp \left[-\frac{T^2 (\mathbf{w} - \mathbf{W})^2}{2(1-ib)} \right],$$

while Eq.(2.10) saves only the first term in the external brackets. Consequently, the spectral intensity contour can be approximately estimated by

$$J(\omega) = |B(\omega)|^2 \approx \frac{pT^2}{2\sqrt{1+b^2}} \exp\left[-\frac{T^2(\omega - W)^2}{1+b^2}\right], \quad (2.11)$$

which is presented in Fig.2.4.

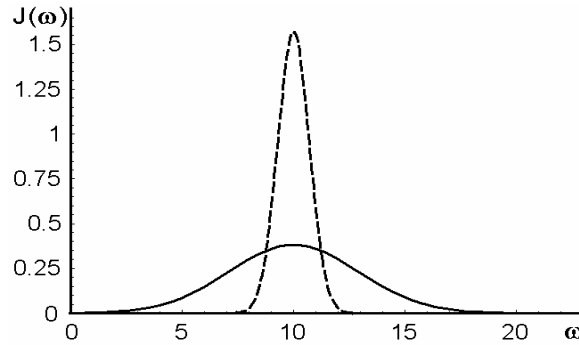


Figure 2.4. Spectral intensity of Gaussian pulses: $b = 0, T = 1, \Omega = 10$ – dashed line; $b = 4, T = 1, \Omega = 10$ – solid line.

The width of this contour is determined by $DW = \omega - W$, so one can write

$$DWT = \sqrt{1+b^2}, \quad (2.12)$$

Equation (2.12) is quite similar to Eq.(2.5) and has the same meaning.

Finally, the field strength auto-correlation function can be estimated. For this purpose, one can consider a two-beam scanning Michelson interferometer and a nonlinear medium, which is the simplest optical auto-correlator. Such a device makes it possible to register the field strength auto-correlation function, which can be exploited via the inverse Fourier transform for finding the spectral power density $|S(\omega)|^2$

and measuring the width of the spectral contour. In so doing, one has to use a square-law photodiode detecting an interference of two incident field strengths $U(t)$ and $U(t-t)$, where the delay time t of the second field can be varied by the corresponding movable mirror of the scanning interferometer.

The issuing electronic signal is proportional to the energy E under registration, if the integration time of that photodiode is sufficiently long. Generally, this energy is proportional to the value

$$E \sim \int_{-\infty}^{\infty} [U(t) + U(t-t)]^2 dt \sim G_0(0) + 2G_A(t) \quad , \quad (2.13)$$

where $G_0(0)$ is a background and

$$G_A(t) = \int_{-\infty}^{\infty} [U(t) \times U(t-t)] dt = \frac{1}{2\mathbf{p}} \int_{-\infty}^{\infty} |B(\mathbf{w})|^2 \exp(-i\mathbf{w}t) d\mathbf{w} \quad , \quad (2.14)$$

Equation (2.14) is true only when the field strength $U(t)$ is real-valued; for example, for the Gaussian pulse described by Eq.(2.6). So, using Eq.(2.14), the function $G_A(t)$ can be calculated due to the Fourier transform of the spectral intensity contour

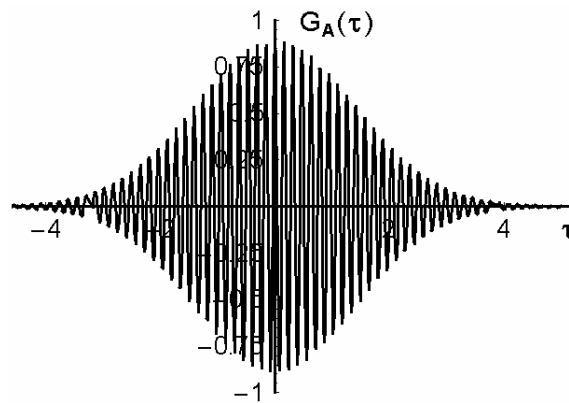
$$\begin{aligned} G_A(t) &= \frac{1}{2\mathbf{p}} \int_{-\infty}^{\infty} |B(\mathbf{w})|^2 \exp(-i\mathbf{w}t) d\mathbf{w} = \\ &= \frac{T\sqrt{\mathbf{p}}}{2} \exp\left(\frac{-t^2}{4T^2}\right) \left[\exp\left(\frac{-b^2 t^2}{4T^2}\right) \cos(Wq) + \right. \end{aligned}$$

$$+ \frac{1}{\sqrt[4]{1+b^2}} \exp \left(\frac{-T^2 W^2}{1+b^2} \right) \cos \left(\frac{b t^2}{4 T^2} - \frac{b T^2 W^2}{1+b^2} + \frac{b}{2} \right) \Bigg\}, \quad (2.15)$$

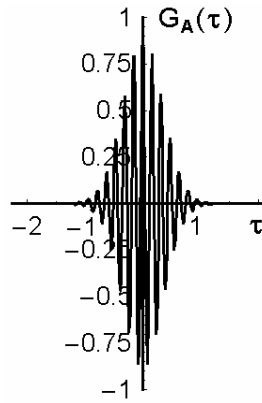
The analysis shows that the second term in the square brackets of Eq.(2.15) is negligible in comparison with the first one, so the approximate expression for the field-strength auto-correlation function can be written as

$$G_A(t) \approx \frac{T\sqrt{p}}{2} \exp \left[-\frac{(1+b^2)t^2}{4T^2} \right] \cos(Wq). \quad (2.16)$$

Two traces for this reduced auto-correlation function are shown in Fig.2.5.



(a)



(b)

Figure 2.5. Field-strength auto-correlation functions for the Gaussian pulses with:

(a) $b = 0, T = 1, \Omega = 40$; (b) $b = 4, T = 1, \Omega = 40$.

That is why the width of the field-strength auto-correlation function can be rather accurately estimated through estimating the exponential term in Eq.(2.16). A level of $1/e$ will be reached with

$$t = t_0 = 2T / \sqrt{1 + b^2} . \quad (2.17)$$

Consequently, t_0 is the half-width of the field-strength auto-correlation function at a level of $1/e$.

2.3 A new technique of measuring the train-average pulse width as well as the value and sign of the frequency chirp of picosecond optical pulses in high-repetition-rate trains

In many cases, for example, with the investigations of evolving the optical solitons in active and passive waveguide structures, a simple method is frequently required for measuring current time-frequency parameters of low-power pico and subpicosecond optical pulses traveling in high-repetition-rate trains. Most widely used is a method based on the formation of a train-average auto-correlation

function of the field strength, which is coupled through the Fourier transform with the spectral power density. From the recorded power spectral density, one can determine an average width of the radiation spectrum. However, in this case, information on the average field phase is lost and it is impossible to determine the time variation of the field amplitude $A(t)$. Exact determination of the train-average pulse duration from the width of the radiation spectrum is only possible when the shape of pulse envelope is known a priori and, in addition, the pulse spectrum is limited [8]. An approximate estimation of the pulse duration is also correct, if the frequency chirp is sufficiently small [9]. In the general case, it is necessary either to pass to determination of the intensity auto-correlation or cross-correlation [10] functions, or to make special measurements to obtain information on the field phase, which often require the application of rather complicated experimental facilities or special computer algorithms [11-14].

Here, it demonstrates an opportunity of providing experimental conditions, under which the train-average auto-correlation function of the field strength can serve as a source of exact and reliable information on the average values of both duration and frequency chirp of a low-power optical pulses traveling in high-repetition-rate trains.

It proceed from the assumption that all pulses in a train are identical pulses with a Gaussian envelope described by Eq.(2.1) with the amplitude $A_0 = \sqrt{P}$, where P is the incoming pulse peak power. These assumptions are not specific for the proposed method and are typical of most of the other measurement methods [8-12]. For a Gaussian envelope, the relationships between the train-average pulse parameters T and b and the width t_0 of the corresponding auto-correlation function measured on a level of $1/e$ are given by Eq.(2.17).

Usually, the real-time auto-correlation function of the field strength averaged over a train of optical pulses is obtained with a scanning Michelson interferometer, which allows measuring the value of t_0 . However, it follows from formula (2.17) that information on the width t_0 of the field strength auto-correlation function is insufficient to determine the time-frequency parameters of the pulse train. That is why one can propose performing two additional measurements of the auto-correlation function width with the help of a scanning Michelson interferometer.

During the second and third measurements, supplementary optical components, changing the parameters T and b in a predetermined way but not influencing the envelope of the investigated pulses, should be placed in front of the beam-splitting mirror of the interferometer, which is presented in the figure 2.6.

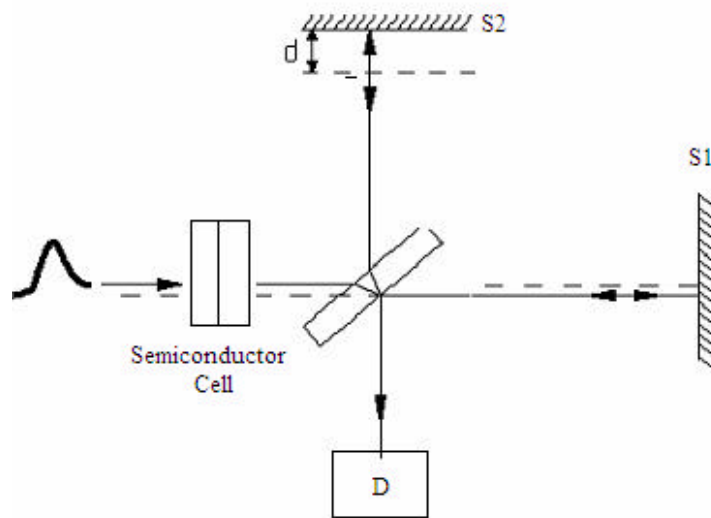


Figure 2.6. Michelson interferometer with a supplementary semiconductor cell.

The auto-correlation function widths \mathbf{t}_m ($m=1, 2$) obtained from the repeated measurements are coupled with the new values of the pulse duration T_m and the frequency chirp b_m through formula (2.17), it assumes that

$$T_m = \mathbf{a}_m T_0 \quad (2.18)$$

and

$$b_m = b_0 + \mathbf{b}_m \quad (2.19)$$

where T_0 and b_0 are unknown values of the parameters T and b , while the quantities \mathbf{a}_m and \mathbf{b}_m are determined by supplementary optical components. Using the above-noted relations, one can write two different algebraic quadratic equations for a quantity of b_0 . The corresponding solutions are given by the formulas

$$b_0 = (q_m \mathbf{a}_m^2 - 1)^{-1} \left[\mathbf{b}_m \pm \sqrt{q_m \mathbf{a}_m^2 (\mathbf{b}_m^2 + 2) - (q_m^2 \mathbf{a}_m^4 + 1)} \right], \quad (2.20)$$

where $q_m = \mathbf{t}_0^2 / \mathbf{t}_m^2$ and \mathbf{t}_m is the width of the field strength auto-correlation function obtained without supplementary optical components. For ($m=1, 2$), Eq.(2.20) gives four values of b_0 , of which two coincide with each other and correspond to just the true value of the train-average frequency chirp of the pulses. The proposed measurement method allows one to determine not only the value, but the sign of the frequency chirp as well, which is often impossible even with the help of substantially more complicated methods, such as, for example, the method described in Ref.[13].

Once the pulse frequency chirp b_0 is determined, one can use formula (2.20) to calculate the pulse duration T by using \mathbf{t}_0 and $b = b_0$.

For the supplementary electronically controlled optical component, one can propose exploiting a specific device based on an InGaAsP single-mode traveling-wave semiconductor laser heterostructure, which is quite similar to a saturable-absorber laser [14] with clarified facets. This device comprises two domains, see Fig.2.7.

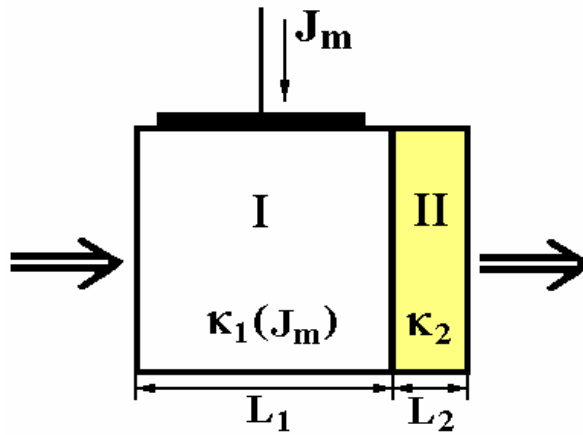


Figure 2.7. Design of the supplementary semiconductor cell: **I** is the domain of linear amplification controlled by the pump current J ; **II** is the domain with a fast-saturable absorption.

Domain I of the linear amplification controlled by pumping current J_m has the length L_1 and is characterized by the low-signal gain factor $k_1(J_m)$. Domain II of a fast-absorption saturation, created by a deep implantation of oxygen ions into the output facet of the heterostructure, has the length L_2 and is characterized by the low-signal absorption factor k_2 and the saturation power P_s . Domain I is able to modify the peak power P_m of pulses entering domain II, so that:

$$P_m = P \exp [k_1(J_m)L_1] \quad (2.21)$$

The peak power P_m determines, in its turn, the values of the parameters \mathbf{a}_m and \mathbf{b}_m , reflecting the action of domain II on the pulses. In the low-signal case, one can use the relations.

$$\begin{aligned} \text{a) } \mathbf{a}_m &= \left(\mathbf{r} P_m \sqrt{2} + 1 \right)^{-1/2}, \\ \text{b) } \mathbf{b}_m &= -z \mathbf{r} P_m \sqrt{2}, \end{aligned} \quad (2.22)$$

where z is the line-width enhancement factor, which is usually in the range $z = 3-8$, and

$$\mathbf{r} = (2 P_s)^{-1} [\mathbf{k}_l (J_m) L_l]. \quad (2.23)$$

is the absorption parameter which may be of the order of $\mathbf{r} \leq 1W^{-1}$. Such a device makes possible performing the repeated measurements without re-adjusting the optical circuit and ensures additions $\mathbf{b}_m \leq 5$ to the frequency chirp [15].

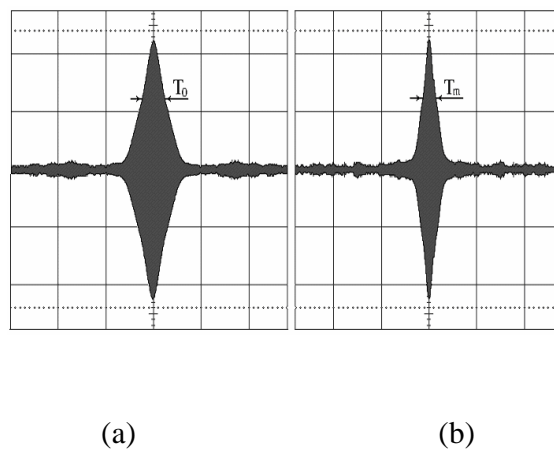


Figure 2.8. Results of numerical simulation of forming the auto-correlation functions by the scanning Michelson interferometer:

(a) without and (b) with an supplementary semiconductor cell introduced into the measurement circuit.

The figure 2.8 demonstrates variation in the auto-correlation function after inserting the supplementary electronically controlled semiconductor optical cell into the measurement circuit. It shows a pair of simulated oscillograms for the auto-correlation functions of Gaussian pulses formed by a scanning Michelson interferometer without (a) and with (b) inserted semiconductor cell for the case of $\mathbf{b}_m = -2$. Arrows mark a level of $\exp(-0.5) \approx 0.606$ used to determine the value of T .

The numerical simulation has been performed for a signal-to-noise ratio of 10, which corresponds to rather typical experimental conditions [16]. The data obtained from triply repeated measurements of T allows us to determine the pulse duration in a range of 1 – 50 ps and the pulse frequency chirp in a range of [-10,10] with an account for the chirp sign. The measurement accuracy is determined by the instability of radiation source and uncertainty of the scanning circuit characteristics as well as by the errors arising during the recording. The total measurement errors for both the pulse duration and the frequency chirp do not exceed 5%.

2.4 Conclusion

It is presented a stimulating contribution to the development of the advanced metrology. Such a viewpoint is based on the two well-determined propositions. The first of them is represented by our theoretic approach to the characterization of low-power bright picosecond optical pulses with an internal frequency modulation simultaneously in time and frequency domains. This proposition exploits

the joint Wigner time-frequency distribution, which can describe the width and the frequency chirp of optical pulse in a unified format. The case, of Gaussian shape when the Wigner distribution is positive has been taken, and the peculiarities for just the Gaussian pulses with a high-frequency filling have been followed in details in both time and frequency domains as well as in terms of the field-strength auto-correlation function. The second proposition is related to the principles of creating the joint Wigner time-frequency distribution by the methods of modern experimental technique. It is proposed and considered conceptually the key features of a new interferometric method elaborated explicitly for accurate and reliable measurements of the train-average width as well as the value and sign of the frequency chirp in bright picosecond optical pulses in high-repetition-rate trains. For this purpose, a two-beam scanning Michelson interferometer has been chosen for obtaining the field-strength auto-correlation function of low-power picosecond pulse trains.

The proposed technique is founded on an ingenious metrology algorithm, assumes using a specially designed two-domain supplementary semiconductor cell, and suggests carrying out a pair of additional measures with exploiting this semiconductor cell, whose properties have been physically described as well. The procedure makes possible constructing the current Wigner distribution in real time scale, which is rather desirable practically, and thus describing low-power bright picosecond optical pulses simultaneously in both time and frequency domains.

2.5 References

[1] E.P.Ippen and C.V.Schenk, "Picosecond Techniques and Applications." in *Ultrashort Light Pulses*, Ed. by S.Shapiro (Springer, Heidelberg, 1977).

- [2] L. Cohen, "Time-frequency distributions—a review," *Proc.IEEE*, vol. 77, no. 7, pp. 941–981, 1989.
- [3] D. Dragoman and M. Dragoman, "Quantum coherent versus classical coherent light," *Optical and Quantum Electronics*, vol. 33, no. 3, pp. 239–252, 2001.
- [4]. A.S.Shcherbakov. "Synchronization of a radio-interferometer by the high-repetition-rate picosecond solitons." *Tech.Phys. Lett.*, vol.19, 615-616 (1993).
- [5]. J. Herrmann and B.Wilhelmi. *Laser fur Ultrakurze Lichtimpulse*. (Akademi-Verlag, Berlin, 1984).
- [6]. J.-C.Diels, J.J.Fontaine, I.C.McMichel, et al. "Control and measurement of ultrashort pulse shapes (in amplitude and phase) with femtosecond accuracy." *Appl. Opt.*, vol.24, 1270-1282 (1985).
- [7]. K.Nagamuna, K.Mogi, and H.Yamada. "General method for ultrashort light pulse chirp measurement." *IEEE J. Quantum Electron.*, vol.25, 1225-1233 (1989).
- [8]. D.J.Kame and R.Trebino. "Single-shot measurement of the intensity and phase of a femtosecond laser pulse." *Proc. SPIE*, vol.1861, 150-160 (1993).
- [9]. E.L.Portnoy, S.D.Yakubovich, N.M.Stelmakh, et. al. "Dynamics of emission of radiation from a hetero-laser with a saturable absorber formed by deep implantation of oxygen ions", *Phys. Semicond.*, vol.22, no.7, 766-768 (1988).
- [10]. **3.5. A.S.Shcherbakov, A.L.Muñoz Zurita, and J.Campos Acosta. "A new technique of measuring low-power picoseconds optical pulse trains". The 2007 SPIE Photonics North Conference (June 4-7, 2007, Ottawa, Canada), Technical Program, p.191, #PD-6-14-2 (2007).**
- [11]. G.P.Agrawal and N.K.Dutta, *Semiconductor lasers*. 2-nd Ed. (Van Nostrand Reinhold, New-York, 1993).
- [12]. I.A.Kniazev, A.S.Shcherbakov, Yu.V.Il'in, et al., "Picosecond pulse source based on a semiconductor laser with a fiber cavity." *Tech. Phys. Lett.*, vol.17, 82-83 (1991).
- [13]. E.I.Andreeva, A.S.Shcherbakov, I.E.Berishev, et al. "Semiconductor source of picosecond pulses at a wavelength of 1.55 μm ." *Tech. Phys. Lett.*, vol.18, 803-804 (1992).

- [14]. A.S.Shcherbakov and E.I.Andreeva. "Observation of picosecond optical pulses with a guiding-center soliton in a single-mode optical fiber wave-guide." Tech. Phys. Lett., vol.20, 873-875 (1994).
- [15]. R.M.Wilcox. "Exponential operators and parameter differentiation in quantum physics." J. Math. Phys., vol.8, 962-982 (1967).
- [16]. **A.S.Shcherbakov, A.L.Muñoz Zurita, A. Y. Kosarsky, J. Campos Acosta** "*Determining the time-frequency parameters of low-power bright picosecond optical pulses by using the interferometric technique*", **Optik**,(2008).

CHAPTER 3

DETERMINING THE TIME-FREQUENCY PARAMETERS OF LOW-POWER BRIGHT PICOSECOND OPTICAL PULSES WITH HYPERBOLIC-SECANT SHAPE.

The characterization of bright optical solitary pulses in pico- and subpicosecond temporal domains is connected with the fundamental problem governed by transferring the data from extremely fast all-optical representation related to frequencies exceeding 1 THz to much slower electronic representation due to the operation of all the modern measurement electronic equipment over frequencies not exceeding 10 GHz. This problem cannot be resolved or canceled, because our equipment cannot operate over light signals directly. Therefore, the progress in measuring both time and frequency parameters of ultrashort optical pulses was oriented on deciding just this fundamental problem [1-4].

The most attractive approach, allowing at least simplifying the fore-mentioned problem, exploits train average characterization of ultrashort pulse strings rather than solitary optical pulses. Nevertheless, the train-average approach needs the regular strings of identical ultrashort optical pulses and, together with this, requires the utilization of a mechanism for sampling. Evidently, the most advanced algorithms for realizing similar sampling all-optically are based on analyzing various correlations between portions inherent in different picosecond pulses in the same pulse string [5-8], i.e. on shaping auto-correlations.

The simplest of them are auto-correlations of the second order, which can be shaped by a two-beam scanning Michelson interferometer.

However, in general case the simplest auto-correlations of the second order does not allow identifying the train-average pulse width due to possible contribution from the internal frequency modulation of pulses under consideration. Such a statement is of particular importance for low-power optical pulses, because just for them it becomes to be particularly complicated to apply any nonlinear-optic technique for growing the second-order correlations.

That is why characterizing low-power optical pulses is often provided via interferometric technique, which makes it possible to perform the needed transformations to keep and measure the most important parameters of picosecond pulses in a high-frequency repetition strings [7–10].

3.1. The Wigner time -frequency distribution for a sech-like pulse

The complex amplitude of optical soliton is given by

$$A_S(t) = \text{sech} \frac{a}{c} \frac{t}{t_0} \frac{\ddot{\theta}}{\theta} \exp \left[i \frac{bt^2}{2t_0^2} \frac{\ddot{\theta}}{\theta} \right], \quad (3.1)$$

where t_0 is the pulse width, b is the parameter of frequency modulation. Generally, the Wigner time-frequency distribution is given by [12]

$$W(t, w) = \frac{1}{2p} \int_{-\infty}^{\infty} A \left(\frac{t}{t_0} - \frac{t_0}{2} \right) \exp(-i t w) A \left(\frac{t}{t_0} + \frac{t_0}{2} \right) dt. \quad (3.2)$$

In the case of a sech-shaped pulse described by Eq.(3.1), the Wigner distribution from Eq.(3.2) can be rewritten as

$$W_S(t, w) = \frac{1}{p} \int_{-\infty}^{\infty} \frac{\exp(-i t g)}{\cosh(t/t_0) + \cosh(2t/t_0)} dt = \frac{2}{p} \int_0^{\infty} \frac{\cos(t g)}{\cosh(t/t_0) + \cosh(2t/t_0)} dt, \quad (3.3)$$

where $g = w + b t / (2 t_0^2)$. Using Ref.[13], see the number 2.5.48-2, one can find from Eq.(3.3) that

$$W_S(t, w) = 2 t_0 \sin \left(2 w t + \frac{b t^2}{t_0^2} \right) \sinh^{-1} \left(\frac{2 t}{t_0} \right) \times \sinh^{-1} \left(\frac{t}{t_0} \right) \exp \left(- \frac{t}{t_0} \left(w + \frac{b t}{2 t_0^2} \right) \right). \quad (3.4)$$

A few examples of the Wigner distribution for a sech-pulse defined by Eq.(3.4) with $t_0 = 1$ are presented in Fig.3.1.

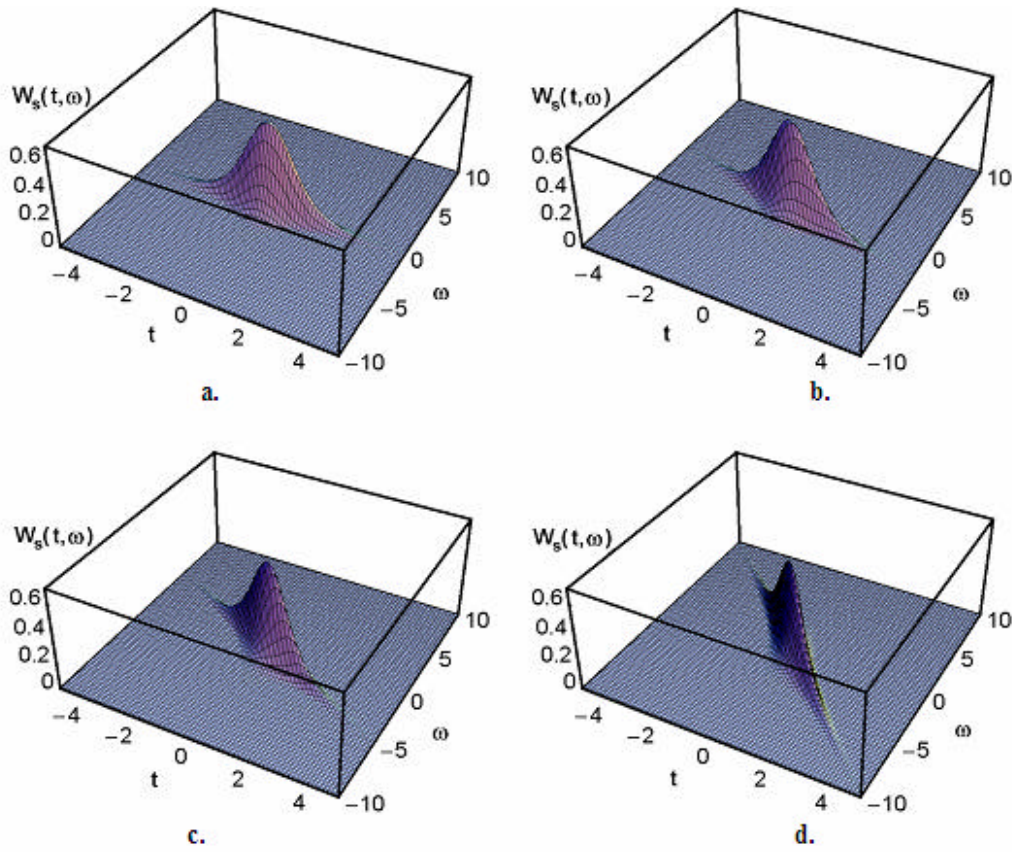


Figure 3.1.

The Wigner time-frequency distribution for a sech-shaped pulse with $t_0 = 1$ and the varying parameter \mathbf{b} : (a) $\mathbf{b} = 0$, (b) $\mathbf{b} = 1$, (c) $\mathbf{b} = 2$, (d) $\mathbf{b} = 4$, and (e) $\mathbf{b} = 6$.

With decreasing the parameter \mathbf{b} , the energy distribution concentrates in a bandwidth corresponding the chirp-free spectrum whose center lies along the line $w = -\mathbf{b}t/t_0^2$. Using Eq.(3.2), one can find the partial (or marginal) one-dimensional distributions for the sech-shaped pulse over the time or frequency separately by

$$\begin{aligned}
 \text{a) } |A_S(t)|^2 &= \int_{-\infty}^{\infty} W_S(t, w) dw, & \text{b) } |S_S(w)|^2 &= \int_{-\infty}^{\infty} W_S(t, w) dt
 \end{aligned}$$

(3.5)

Substituting Eq.(3.2) in Eq.(3.5a), one can write

$$\int_{-\infty}^{\infty} \dot{W}_S(t, w) dw = \frac{2t_0}{\sinh(2t/t_0)} \int_{-\infty}^{\infty} \frac{\sin(2wt + bt^2 t_0^{-2})}{\sinh[p t_0 (w + 2^{-1} b t t_0^{-2})]} dw$$

Using the notation $x = p t_0 (w + b t t_0^{-2})$ and applying Ref.[13], see the number 2.5.46-2, one can obtain

$$\int_{-\infty}^{\infty} \dot{W}_S(t, w) dw = \frac{4t_0}{p \sinh(2t/t_0)} \int_0^{\infty} \frac{\sin(2t x p^{-1} t_0^{-1})}{\sinh x} dx = \operatorname{sech}^2 \left(\frac{p t_0 w_0}{2} \right). \quad (3.6)$$

Then, in the case of the unchirped pulse when $b = 0$, one can write, in particular, that

$$|S_S(w, b = 0)|^2 = \int_{-\infty}^{\infty} \dot{W}_S(t, w, b = 0) dt = \frac{4t_0}{\sinh(p t_0 w)} \int_0^{\infty} \frac{\sin(2tw)}{\sinh(2t t_0^{-1})} dt = \frac{t_0^2}{4} \operatorname{sech}^2 \left(\frac{p t_0 w_0}{2} \right), \quad (3.7)$$

where again Ref.[13], see the number 2.5.46-2, had been applied. When $b \neq 0$, the corresponding integral expression includes both odd and even functions under the integral signs. Because of integrating in symmetric limits, only the even terms give non-zero contributions in this integral, so that one can obtain

$$a) |S_S(w, b \neq 0)|^2 = \int_{-\infty}^{\infty} \dot{W}_G(t, w) dt = X_I^2(w) + Y_I^2(w),$$

$$b) X_1(\omega) = \frac{1}{2p} \int_{-\infty}^{\infty} \text{sech} \left(\frac{t}{t_0} \right) \cos \left(\frac{bt^2}{2t_0^2} \right) \cos(\omega t) dt,$$

$$c) Y_1(\omega) = \frac{1}{2p} \int_{-\infty}^{\infty} \text{sech} \left(\frac{t}{t_0} \right) \sin \left(\frac{bt^2}{2t_0^2} \right) \cos(\omega t) dt.$$

(3.8)

Both the integrals in Eqs.(3.8b) and (3.8c) can be calculated, but the resulting expressions are too cumbersome; that is why they are in use with these notations. A few examples of the partial one-dimensional distributions for the sech-pulses, determined by Eqs.(3.6) and (3.8) with $t_0 = 1$ in time and frequency domains, are shown in Fig.3.2.

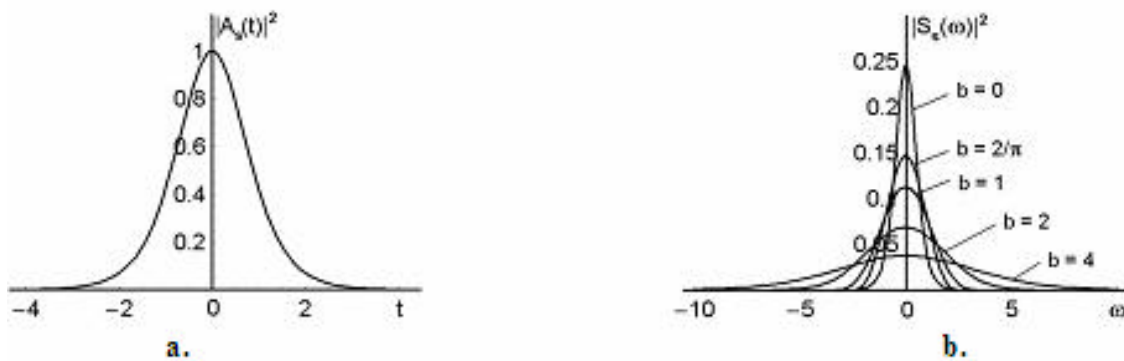


Figure 3.2. The **sech**-pulse with $t_0 = 1$ $t_0 = 1$: the power density profile (a) and the spectral density profiles (b) with the varying parameter **b** of the frequency chirp: **b = 0** (for the maximal intensity plot), **b = 2/p**, **b = 1**, **b = 2**, and **b = 4** (for the minimal intensity plot).

3.2 Square -average determination for the parameters of a sech-pulse.

Originally, the square-average time duration t_{SA} and the square-average spectral width w_{SA} for an arbitrary pulse are determined by the following set of equations [14]

$$\text{a) } t_{SA} = \sqrt{T_2 - (T_1)^2}, \quad \text{b) } T_n = E^{-1} \int_{-\infty}^{\infty} t^n |A_S(t)|^2 dt, \quad \text{c) } E = \int_{-\infty}^{\infty} |A_S(t)|^2 dt. \quad (3.9)$$

$$\text{a) } w_{SA} = \sqrt{w_2 - (w_1)^2}, \quad \text{b) } w_n = E^{-1} \int_{-\infty}^{\infty} w^n |Z(w)|^2 dw, \quad \text{c) } Z(w) = \frac{1}{2p} \left| \int_{-\infty}^{\infty} A_S(t) \exp(-iwt) dt \right|^2. \quad (3.10)$$

Let us consider these values for a chirped pulse with a sech-like shape, which is given by Eq.(3.1). Exploiting Eq.(3.9) for such a pulse with an arbitrary frequency chirp, one can estimate the square-average time duration of a sech-pulse as $t_{SA} = pt_0 / (2\sqrt{3})$, because $E = 2t_0$, $T_1 = 0$, and $T_2 = p^2 t_0^2 / 12$. To estimate the square-average spectral width w_{SA} let us first consider an unchirped sech-pulse with $\mathbf{b} = \mathbf{0}$. Using the Ref.[13], see no.2.4.10-19, one can find

$$\text{a) } Z(w, \mathbf{b} = \mathbf{0}) = \frac{pt_0^2}{2} \text{sech}^2 \left[\frac{p}{2} \frac{t_0 w}{\sqrt{3}} \right], \quad \text{b) } w_2(\mathbf{b} = \mathbf{0}) = \frac{1}{3t_0^2}, \quad \text{c) } w_{SA}(\mathbf{b} = \mathbf{0}) = \frac{1}{t_0 \sqrt{3}}, \quad (3.11)$$

due to $w_1(\mathbf{b} = \mathbf{0}) = 0$. It should be noted that $t_{SA} \times w_{SA}(\mathbf{b} = \mathbf{0}) = p/6$. When $\mathbf{b} \neq \mathbf{0}$, one can write

$$|Z(w, \mathbf{b})|^2 = 2p[X_1^2(w) + Y_1^2(w)], \quad (3.12)$$

Using Eqs.(3.10) and (3.12), one can find that $w_1 = \frac{p}{t_0} \int_{-\infty}^{\infty} w [X_1^2(w) + Y_1^2(w)] dw$, due to the oddness of a function under integral, which is calculated within symmetric limits. In its turn, the value of w_2 consists of two contributions $w_2 = w_2(X_1) + w_2(Y_1)$, where

$$\begin{aligned} \text{a) } w_2(X_1) &= \frac{p}{t_0} \int_{-\infty}^{\infty} w^2 X_1^2(w) dw, & \text{b) } w_2(Y_1) &= \frac{p}{t_0} \int_{-\infty}^{\infty} w^2 Y_1^2(w) dw. \end{aligned} \quad (3.13)$$

The term $w_2(X_1)$ from Eq.(3.13a), in particular, can be rewritten in more details as

$$w_2(X_1) = \frac{1}{4pt_0} \int_{-\infty}^{\infty} dt_1 \operatorname{sech} \left(\frac{at_1}{c} \right) \cos \left(\frac{bt_1}{2t_0} \right) \int_{-\infty}^{\infty} dt_2 I(w, t_1, t_2) \operatorname{sech} \left(\frac{at_2}{c} \right) \cos \left(\frac{bt_2}{2t_0} \right), \quad (3.14)$$

$$\begin{aligned} I(w, t_1, t_2) &= \int_{-\infty}^{\infty} dw w^2 \cos(wt_1) \cos(wt_2) = \\ &= -\frac{p}{2} \left[d^{(2)}(t_1 + t_2) + d^{(2)}(t_1 - t_2) + d^{(2)}(-t_1 + t_2) + d^{(2)}(-t_1 - t_2) \right], \end{aligned} \quad (3.15)$$

because of [15] the relation $d^{(m)}(x - y) = \frac{1}{2p} \int_{-\infty}^{\infty} dw (iw)^2 \exp(iwx) \exp(-iwy)$.

Then, one can use the standard formula $\int_{-\infty}^{\infty} dx F(x) d^{(m)}(x-y) = \int_{-\infty}^{\infty} dx \frac{d^2 F(x)}{dx^2} d(x-y) = \frac{d^2 F(y)}{dy^2}$ to

convert Eq.(14) into

$$w_2(X_1) = -\frac{1}{2t_0} \int_{-\infty}^{\infty} dt_1 \operatorname{sech} \frac{at_1}{c t_0} \cos \frac{bt_1^2}{2t_0} \cdot \frac{d^2}{dt_1^2} \operatorname{sech} \frac{at_1}{c t_0} \cos \frac{bt_1^2}{2t_0}, \quad (3.16)$$

where the evenness of hyperbolic and trigonometric functions had been exploited. Quite similar result appears during the corresponding conversion of the term $w_2(Y_1)$ from Eq.(3.13b)

$$w_2(Y_1) = -\frac{1}{2t_0} \int_{-\infty}^{\infty} dt_1 \operatorname{sech} \frac{at_1}{c t_0} \sin \frac{bt_1^2}{2t_0} \cdot \frac{d^2}{dt_1^2} \operatorname{sech} \frac{at_1}{c t_0} \sin \frac{bt_1^2}{2t_0}. \quad (3.17)$$

Summing Eqs.(3.15) and (3.16), one can calculate

$$w_2 = w_2(X_1) + w_2(Y_1) = -\frac{1}{2t_0} \int_{-\infty}^{\infty} dt_1 \left[\operatorname{sech} \frac{at_1}{c t_0} \cos \frac{bt_1^2}{2t_0} \cdot \frac{d^2}{dt_1^2} \operatorname{sech} \frac{at_1}{c t_0} \cos \frac{bt_1^2}{2t_0} - \operatorname{sech}^2 \frac{at_1}{c t_0} \cdot \frac{d^2}{dt_1^2} \operatorname{sech} \frac{at_1}{c t_0} \cos \frac{bt_1^2}{2t_0} \right]. \quad (3.18)$$

Finally with $w_1 = 0$, the following results can be obtained

$$\text{a) } w_2 = \frac{1}{3t_0^2} + \frac{pb^2}{12}, \quad \text{b) } w_{SA} = \sqrt{w_2 - (w_1)^2} = \sqrt{\frac{1}{3t_0^2} + \frac{pb^2}{12}}. \quad (3.19)$$

In the particular case of $b = 0$, Eq.(3.19b) is coinciding with Eq.(3.11c).

3.3 A sech-pulse with a high-frequency filling

Now, one can take the case of sech-pulse with the slowly varying amplitude and with a high-frequency filling by the optical carrier frequency $W \gg 1$:

$$U_S(t) = \text{sech} \left[\frac{a}{c} \frac{t}{t_0} \right] \cos \left[Wt + \frac{bt^2}{2t_0^2} \right]. \quad (3.20)$$

The corresponding intensity distribution, instead of a smooth contour described by Eq.(3.6) for

$I(t) = |A_S(t)|^2$, includes now some oscillations and is given by

$$J(t) = |U(t)|^2 = \text{sech}^2 \left[\frac{a}{c} \frac{t}{t_0} \right] \cos^2 \left[Wt + \frac{bt^2}{2t_0^2} \right], \quad (3.21)$$

The smooth contours $I(t)$ and the oscillating distributions $J(t)$ are shown in Fig.3.3 One can see from Fig.3.3 that the half-width has the same value t_0 for these two plots.

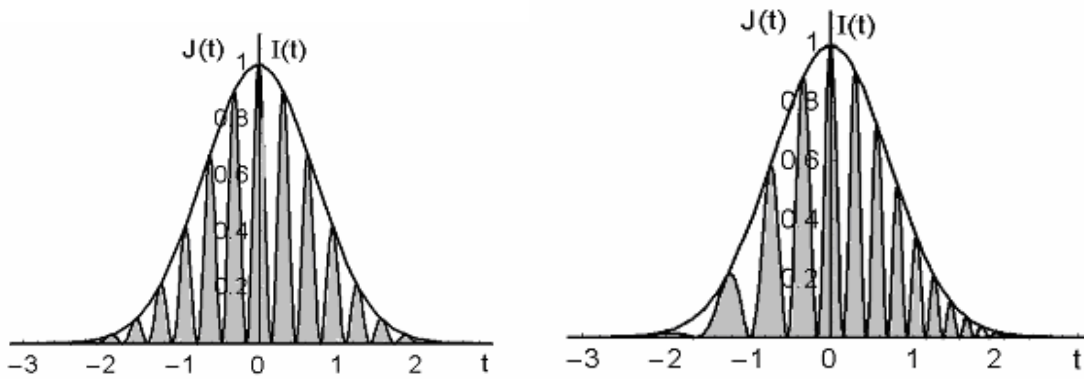


Figure 3.3

The plots of $I(t)$ and $J(t)$ with : (a) $b = 0, t_0 = 1, W = 10$; (b) $b = 4, t_0 = 1, W = 10$.

Then, one can consider the complex spectrum contour. Performing the Fourier transform of Eq.(3.20), one can find

$$B_S(\omega) = \frac{1}{2\pi} \int_{-\infty}^{\infty} U_S(t) \exp(i\omega t) dt = \frac{1}{2\pi} \int_{-\infty}^{\infty} \operatorname{sech} \frac{\alpha t}{t_0} \cos \frac{\alpha}{\xi} Wt + \frac{bt^2}{2t_0^2} \exp(i\omega t) dt. \quad (3.22)$$

Equation (3.22) includes both odd and even functions under the integral signs. Because of integrating in symmetric limits in Eq.(3.22), only even terms have to be conserved. Then, one can consider the case of $\omega \gg W$ with $W \gg 1$. In this case, $(\omega + W) \gg (\omega - W)$ and one may omit all the fast-oscillating terms in Eq.(3.22). As a result, one can obtain

$$B_S(\omega) = X_2(\omega) + i Y_2(\omega), \quad (3.23)$$

$$X_2(\omega) = \frac{1}{4\pi} \int_{-\infty}^{\infty} \operatorname{sech} \frac{\alpha t}{t_0} \cos \frac{\alpha}{\xi} \frac{bt^2}{2t_0^2} \cos[(\omega - W)t] dt, \quad (3.24)$$

$$Y_2(\omega) = \frac{1}{4p} \int_{-\infty}^{\infty} \operatorname{sech} \left[\frac{a}{c} \left(\frac{t}{t_0} - \frac{b}{2t_0^2} t^2 \right) \right] \cos[(\omega - W)t] dt. \quad (3.25)$$

Both the integrals in Eqs.(3.24) and (3.25) can be calculated, but the resulting expressions are too cumbersome, so that it will use these notations. The spectral intensity contour is given by the following real-valued expression

$$J(\omega) = |B_S(\omega)|^2 = X_2^2(\omega) + Y_2^2(\omega), \quad (3.26)$$

which gives the distributions being quite similar to the plots presented in Fig.3.2, but shifted by the carrier frequency W .

3.4 Auto-correlation function for a sech-pulse with the frequency chirp.

The field strength auto-correlation function can be estimated, for this purpose, one can consider a two-beam scanning Michelson interferometer, which is the simplest optical auto-correlator. Such a device makes it possible to register the field strength auto-correlation function, which can be exploited via the inverse Fourier transform for finding the spectral power density $|S_S(\omega)|^2$ and measuring the width of the spectral contour. In so doing, one has to use a square-law photodiode detecting an interference of two incident field strengths $U_S(t)$ and $U_S(t - \tau)$, where the delay time τ of the second field can be varied by the corresponding movable mirror of the scanning interferometer. The issuing electronic signal is proportional to the energy E under registration, if the integration time of that photodiode is sufficiently long. Generally, this energy includes a background $G_0(0)$ and is proportional to the value

$$E \sim \int_{-\infty}^{\infty} [U_S(t) + U_S(t-t)]^2 dt \sim G_0(0) + 2G_A(t), \quad (3.27)$$

$$G_A(t) = \int_{-\infty}^{\infty} [U_S(t) - U_S(t-t)] dt = \frac{1}{2\pi} \int_{-\infty}^{\infty} |B_S(w)|^2 \exp(-iwt) dw. \quad (3.28)$$

Equation (3.28) is true only when the field strength $U_S(t)$ is real-valued as for a sech-pulse described by Eq.(3.20). So, using Eq.(3.28), the function $G_A(t)$ can be calculated due to the Fourier transform of the spectral intensity contour

$$G_A(t) = \frac{1}{2\pi} \int_{-\infty}^{\infty} |B_S(w)|^2 \exp(-iwt) dw = \frac{1}{2\pi} \int_{-\infty}^{\infty} [X_2^2(w) + Y_2^2(w)] \exp(-iwt) dw \quad (3.29)$$

In fact, the function $G_A(t)$ includes two terms

$$\text{a) } G_1(t) = \frac{1}{2\pi} \int_{-\infty}^{\infty} X_2^2(w) \exp(-iwt) dw, \quad \text{b) } G_2(t) = \frac{1}{2\pi} \int_{-\infty}^{\infty} Y_2^2(w) \exp(-iwt) dw. \quad (3.30)$$

Using Eq.(3.24), the integral in Eq.(3.30) can be formally rewritten as

$$G_1(t) = \frac{1}{32p^3} \int_{-\infty}^{\infty} dt_1 \operatorname{sech} \left[\frac{t_1}{t_0} \right] \cos \left[\frac{bt_1^2}{2t_0^2} \right] \int_{-\infty}^{\infty} dt_2 \operatorname{sech} \left[\frac{t_2}{t_0} \right] \cos \left[\frac{bt_2^2}{2t_0^2} \right] \int_{-\infty}^{\infty} dw \exp(-iwt) \cos[(w-W)t_1] \cos[(w-W)t_2] \quad (3.31)$$

The last internal integral in Eq.(3.31) can be presented as

$$H = \int_{-\infty}^{\infty} dw \exp(-iwt) \cos[(w-W)t_1] \cos[(w-W)t_2] = H_1 + H_2, \quad (3.32)$$

where $H_{1,2} = \frac{1}{2} \int_{-\infty}^{\infty} dw \exp(-iwt) \cos[(w-W)(t_1 \pm t_2)]$. Let us introduce the new variable $J = w - W$

with $dw = dJ$ to convert of $H_{1,2}$ into the form

$$H_{1,2} = \frac{1}{2} \exp(-itW) \int_{-\infty}^{\infty} dJ \exp(-iJt) \cos[J(t_1 \pm t_2)].$$

Because of $\frac{1}{2p} \int_{-\infty}^{\infty} dx \exp(-ixy) \cos(ax) = \frac{1}{2} [d(y+a) + d(y-a)]$, one can find that

$$H = \frac{p}{2} \exp(-itW) [d(t+t_1+t_2) + d(t+t_1-t_2) + d(t-t_1-t_2) + d(t-t_1+t_2)]. \quad (3.33)$$

These d -functions work during the calculation of middle integral with respect to t_2 in Eq.(3.31) as

$$\int_{-\infty}^{\infty} dt_2 H \operatorname{sech} \left[\frac{t_2}{t_0} \right] \cos \left[\frac{bt_2^2}{2t_0^2} \right] = \frac{p}{2} \exp(-itW)$$

$$\begin{aligned}
& \int_{-\infty}^{\infty} dt_2 \operatorname{sech} \frac{a t_2}{c} \frac{\ddot{\theta}}{t_0} \cos \frac{b t_2^2}{2 t_0^2} \frac{\ddot{\theta}}{\theta} \left[d(t + t_1 + t_2) + d(t + t_1 - t_2) + d(t - t_1 - t_2) + d(t - t_1 + t_2) \right] = \\
& = p \exp(-itW) \int_{-\infty}^{\infty} \operatorname{sech} \frac{a t + t_1}{c} \frac{\ddot{\theta}}{t_0} \cos \frac{b(t + t_1)^2}{2 t_0^2} \frac{\ddot{\theta}}{\theta} \dot{u} + \operatorname{sech} \frac{a t - t_1}{c} \frac{\ddot{\theta}}{t_0} \cos \frac{b(t - t_1)^2}{2 t_0^2} \frac{\ddot{\theta}}{\theta} \dot{u} \dot{y} \dot{p}, \quad (3.34)
\end{aligned}$$

where the evenness of functions has been used. Then, Eq.(3.34) can be substituted into Eq.(3.31)

$$\begin{aligned}
G_1(t) &= \frac{1}{32p^2} \exp(-itW) \int_{-\infty}^{\infty} dt_1 \operatorname{sech} \frac{a t_1}{c} \frac{\ddot{\theta}}{t_0} \cos \frac{b t_1^2}{2 t_0^2} \frac{\ddot{\theta}}{\theta} \dot{u} \dot{y} \dot{p} \\
& \int_{-\infty}^{\infty} \operatorname{sech} \frac{a t + t_1}{c} \frac{\ddot{\theta}}{t_0} \cos \frac{b(t + t_1)^2}{2 t_0^2} \frac{\ddot{\theta}}{\theta} \dot{u} \dot{y} \dot{p} + \operatorname{sech} \frac{a t - t_1}{c} \frac{\ddot{\theta}}{t_0} \cos \frac{b(t - t_1)^2}{2 t_0^2} \frac{\ddot{\theta}}{\theta} \dot{u} \dot{y} \dot{p}. \quad (3.35)
\end{aligned}$$

Now, applying the same approach to Eq.(3.30b), one can obtain

$$\begin{aligned}
G_2(t) &= \frac{1}{32p^2} \exp(-itW) \int_{-\infty}^{\infty} dt_1 \operatorname{sech} \frac{a t_1}{c} \frac{\ddot{\theta}}{t_0} \sin \frac{b t_1^2}{2 t_0^2} \frac{\ddot{\theta}}{\theta} \dot{u} \dot{y} \dot{p} \\
& \int_{-\infty}^{\infty} \operatorname{sech} \frac{a t + t_1}{c} \frac{\ddot{\theta}}{t_0} \sin \frac{b(t + t_1)^2}{2 t_0^2} \frac{\ddot{\theta}}{\theta} \dot{u} \dot{y} \dot{p} + \operatorname{sech} \frac{a t - t_1}{c} \frac{\ddot{\theta}}{t_0} \sin \frac{b(t - t_1)^2}{2 t_0^2} \frac{\ddot{\theta}}{\theta} \dot{u} \dot{y} \dot{p}. \quad (3.36)
\end{aligned}$$

To simplify a sum of Eq.(3.35) and (3.36) one can use the standard ratios and find

$$G_A(t) = G_1(t) + G_2(t) = \frac{1}{32p^2} \exp(-itW) \int_{-\infty}^{\infty} dt_1 \operatorname{sech} \frac{a t_1}{c} \frac{\ddot{\theta}}{t_0} \frac{\ddot{\theta}}{\theta} \dot{u} \dot{y} \dot{p}$$

$$\int_{-1}^1 \operatorname{sech} \frac{a}{c} \frac{t+t_1}{t_0} \frac{\ddot{0}}{\ddot{\theta}} \cos \frac{b(t^2+2t_1 t)}{2t_0^2} \frac{\dot{u}}{\dot{h}} + \operatorname{sech} \frac{a}{c} \frac{t-t_1}{t_0} \frac{\ddot{0}}{\ddot{\theta}} \cos \frac{b(t^2-2t_1 t)}{2t_0^2} \frac{\dot{u}}{\dot{h}} \frac{\ddot{y}}{\ddot{p}}. \quad (3.37)$$

Then, one can apply the ratios $\cos \frac{b(t^2 \pm 2t_1 t)}{2t_0^2} \frac{\dot{u}}{\dot{h}} = \cos \frac{a}{c} \frac{bt^2}{2t_0^2} \frac{\ddot{0}}{\ddot{\theta}} \cos \frac{a}{c} \frac{bt_1 t}{t_0^2} \frac{\ddot{0}}{\ddot{\theta}} \mp \sin \frac{a}{c} \frac{bt^2}{2t_0^2} \frac{\ddot{0}}{\ddot{\theta}} \sin \frac{a}{c} \frac{bt_1 t}{t_0^2} \frac{\ddot{0}}{\ddot{\theta}}$ to

Eq.(3.37). Two terms with $\sin(bt_1 t/t_0^2)$ give the odd functions under the integral signs in symmetrical limits, so that the corresponding integrals equal to zero. That is why with $G_A(t) = G_1(t) + G_2(t)$ it arrive at

$$G_A(t) = \frac{\exp(-itW)}{32p^2} \cos \frac{a}{c} \frac{bt^2}{2t_0^2} \frac{\ddot{0}}{\ddot{\theta}} \int_{-1}^1 dt_1 \operatorname{sech} \frac{a}{c} \frac{t_1}{t_0} \frac{\ddot{0}}{\ddot{\theta}} \cos \frac{a}{c} \frac{bt_1 t}{t_0^2} \frac{\ddot{0}}{\ddot{\theta}} \left[\operatorname{sech} \frac{a}{c} \frac{t+t_1}{t_0} \frac{\ddot{0}}{\ddot{\theta}} + \operatorname{sech} \frac{a}{c} \frac{t-t_1}{t_0} \frac{\ddot{0}}{\ddot{\theta}} \right]. \quad (3.38)$$

At this stage, one can take the ratios

$$\operatorname{sech} \frac{a}{c} \frac{t_1}{t_0} \frac{\ddot{0}}{\ddot{\theta}} \operatorname{sech} \frac{a}{c} \frac{t \pm t_1}{t_0} \frac{\ddot{0}}{\ddot{\theta}} = 2 \frac{e}{e} \cosh \frac{a}{c} \frac{t_1 + t \pm t_1}{t_0} \frac{\ddot{0}}{\ddot{\theta}} + \cosh \frac{a}{c} \frac{t_1 - t \mp t_1}{t_0} \frac{\ddot{0}}{\ddot{\theta}} \frac{\dot{u}}{\dot{h}}^{-1} \quad \text{and include them into Eq.(3.38) to}$$

write $G_A(t) = g_1(t) + g_2(t)$, where

$$g_1(t) = \frac{\exp(-itW)}{16p^2} \cos \frac{a}{c} \frac{bt^2}{2t_0^2} \frac{\ddot{0}}{\ddot{\theta}} \int_{-1}^1 dt_1 \cos \frac{a}{c} \frac{bt_1 t}{t_0^2} \frac{\ddot{0}}{\ddot{\theta}} \left[\cosh \frac{a}{c} \frac{t+2t_1}{t_0} \frac{\ddot{0}}{\ddot{\theta}} + \cosh \frac{a}{c} \frac{t}{t_0} \frac{\ddot{0}}{\ddot{\theta}} \right]^{-1}. \quad (3.39)$$

$$g_2(t) = \frac{\exp(-itW)}{16p^2} \cos \frac{a}{c} \frac{bt^2}{2t_0^2} \frac{\ddot{0}}{\ddot{\theta}} \int_{-1}^1 dt_1 \cos \frac{a}{c} \frac{bt_1 t}{t_0^2} \frac{\ddot{0}}{\ddot{\theta}} \left[\cosh \frac{a}{c} \frac{t}{t_0} \frac{\ddot{0}}{\ddot{\theta}} + \cosh \frac{a}{c} \frac{2t_1 - t}{t_0} \frac{\ddot{0}}{\ddot{\theta}} \right]^{-1}. \quad (3.40)$$

To integrate Eqs.(3.39) and (3.40) one has to introduce a pair of the new independent variables

$J_{1,2} = 2t_1 \pm t$, so that $t_1 = (J_{1,2} \mp t)/2$ and $dt_1 = dJ_{1,2}/2$. Again, one can exploit the standard ratios

$$\cos \frac{bt_1 t_0}{c} = \cos \frac{bt(J_{1,2} \mp t)}{2c} = \cos \frac{btJ_{1,2}}{2c} \cos \frac{bt^2}{2c} \pm \sin \frac{btJ_{1,2}}{2c} \sin \frac{bt^2}{2c}$$

Function $g_1(t)$ and $g_2(t)$ take the same form in terms of the corresponding new variable, J_1 or J_2 , namely,

$$g_{1,2}(t) = \frac{\exp(-itW)}{32p^2} \cos^2 \frac{bt^2}{2c} \int_0^\infty dJ_{1,2} \cos \frac{btJ_{1,2}t}{2c} \left[\cosh \frac{J_{1,2}}{t_0} + \cosh \frac{t}{t_0} \right]^{-1}. \quad (3.41)$$

The odd terms with $\sin[btJ_{1,2}/(2t_0^2)]$ gave zero. Using Ref.[13], the number 2.5.48-2, one can integrate Eq.(3.41)

$$\int_0^\infty dJ_{1,2} \cos \frac{btJ_{1,2}t}{2c} \left[\cosh \frac{J_{1,2}}{t_0} + \cosh \frac{t}{t_0} \right]^{-1} = \frac{pt_0 \sin \left[\frac{bt^2}{2t_0^2} \right]}{\sinh(t/t_0) \sinh[pt/(2t_0)]}. \quad (3.42)$$

Using Eqs.(3.39) and (3.40), one can express the field strength auto-correlation function inherent in a sech-like pulse as

$$G_A(t) = \frac{t_0 \exp(-itW)}{8p} \cos^2 \left[\frac{\pi b t^2}{2t_0^2} \right] \frac{\sin[bt^2/(2t_0^2)]}{\sinh(t/t_0) \sinh[pb t/(2t_0)]} \quad (3.43)$$

The normalized traces for the real parts of this field strength auto-correlation function are shown in Fig.3.4.

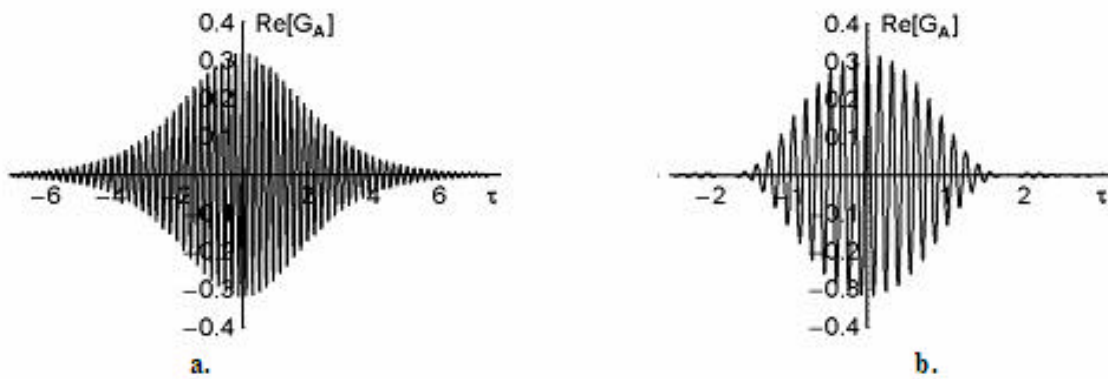


Figure 3.4

The normalized real parts of field-strength auto-correlation functions for the sech-pulses with:

$$(a) \mathbf{b} = \mathbf{0}, \quad t_0 = \mathbf{1}, \quad W = \mathbf{40}; \quad (b) \mathbf{b} = \mathbf{1}, \quad t_0 = \mathbf{1}, \quad W = \mathbf{40}.$$

Now, using Eq.(3.9), one can estimate a square-average width of the field strength auto-correlation function as

$$a) \quad t_A = \sqrt{T_{A2} - (T_{A1})^2}, \quad b) \quad T_{An} = E_A^{-1} \int_{-\infty}^{\infty} t^n |G_A(t)|^2 dt, \quad c) \quad E_A = \int_{-\infty}^{\infty} |G_A(t)|^2 dt. \quad (3.44)$$

It follows from Eq.(3.44b) that $T_{A1} \neq 0$. Both the integrals in Eqs.(3.44) cannot be for the present calculated analytically in a closed form, so that the duration t_A can be presented as the graphic

function of the parameters t_0 and b . That is why the variable t and another values in Eqs.(3.44) will be simply normalized by t_0 , and one can write with $q = t/t_0$

$$\begin{aligned}
 \text{a) } \frac{t_A}{t_0} = F(b) &= \frac{1}{E_A(b)} \int_{-\infty}^{\infty} q^2 \frac{\cos^4(bq^2/2) \sin^2(bq^2/2) dq}{\sinh^2(q) \sinh^2(pbq/2)} \quad (3.45) \\
 \text{b) } E_A(b) &= \int_{-\infty}^{\infty} \frac{\cos^4(bq^2/2) \sin^2(bq^2/2) dq}{\sinh^2(q) \sinh^2(pbq/2)}
 \end{aligned}$$

One can see from Eq.(3.45) that $F(b) = F(-b)$ and $E_A(b) = E_A(-b)$. The corresponding exact plots of $F(b)$, divided in two parts for the convenience of practical usage, are depicted in Fig.3.5

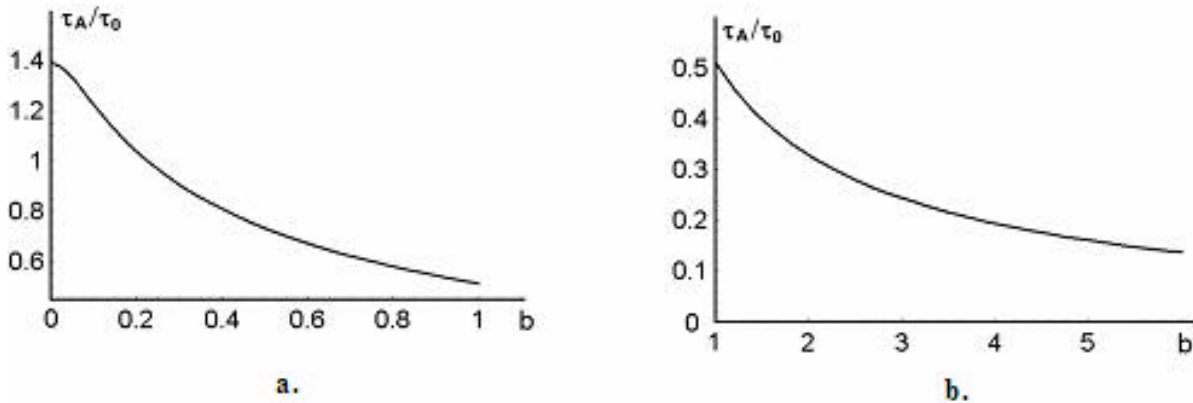


Figure 3.5.

The normalized square-average time duration t_A/t_0 of the field strength auto-correlation function versus the frequency chirp b for a sech-pulse: (a) $b \in [0, 1]$ and (b) $b \in [1, 6]$.

3.5. Application of the above proposed technique to sech-like pulses.

For a sech-pulse, the relation between the pulse parameters, namely, the frequency chirp b and the square-average pulse duration $t_{SA} = pt_0/(2\sqrt{3})$, and the square-average duration t_A of the

corresponding auto-correlation function follows from Eq.(3.44a) and is expressed through the function $F(\mathbf{b})$ presented in Fig.3.6 as

$$t_A = \frac{2\sqrt{3} t_{SA}}{p} F(\mathbf{b}) = t_0 F(\mathbf{b}). \quad (3.46)$$

To illustrate how such a technique works, let us consider the particular case, when, for example, the approximate presentation $F(\mathbf{b}) \approx \sqrt{2} (1+|\mathbf{b}|)^{-a}$ with $a \approx 1.3 - 1.5$, see Fig.3.6, can be chosen. Similar presentations give us an accuracy of about a few percents and can be considered as rather acceptable for practice. But what is much more important, such a presentation for $F(\mathbf{b})$ makes it possible to find both the value and the sign of the chirp parameter \mathbf{b} . One can see from Fig.3.6 that, in particular, the value $a = 1.5$ describes better an area of $|\mathbf{b}| \leq 1$.

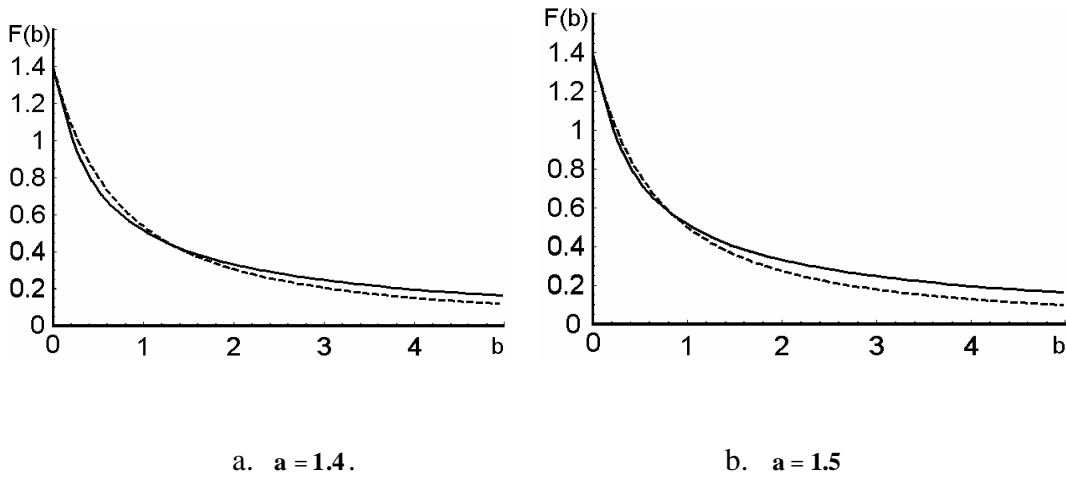


Figure 3.6. Two practically acceptable simple approximations for the function $F(\mathbf{b})$

with different values of the factor \mathbf{a} .

It assume that $t_m = a_m t_0$ and $\mathbf{b}_m = \mathbf{b}_0 + \mathbf{b}_m$, where t_0 and \mathbf{b}_0 are unknown values of the duration and frequency chirp, while the quantities a_m and \mathbf{b}_m are determined by supplementary optical components, and find

$$\text{a) } t_{A0} = t_0 F(\mathbf{b}_0) \gg \frac{t_0 \sqrt{2}}{(1+|\mathbf{b}_0|)^{3/2}}, \quad \text{b) } a_m^{-1} t_{Am} = t_0 F(\mathbf{b}_0 + \mathbf{b}_m) \gg \frac{t_0 \sqrt{2}}{(1+|\mathbf{b}_0 + \mathbf{b}_m|)^{3/2}}. \quad (3.47)$$

Using Eqs.(3.47), one can write the following equation

$$\text{a) } g_m^{2/3} (1+|\mathbf{b}_0|) = 1+|\mathbf{b}_0 + \mathbf{b}_m|, \quad \text{b) } g_m = \frac{t_{A0}}{t_{Am}} a_m > 0, \quad (3.48)$$

so that $\text{Im}(g_m^{2/3}) = 0$. At this stage, one has to take into account that both \mathbf{b}_0 and \mathbf{b}_m can be positive or negative valued. Consequently, it should consider a quartet of possible combinations of their signs:

1) $\mathbf{b}_0 > 0$ and $\mathbf{b}_m > 0$; Eq.(3.48a) takes the form $g_m^{2/3} (1+\mathbf{b}_0) = 1+\mathbf{b}_0 + \mathbf{b}_m$, so that

$$(\mathbf{b}_0)_{1m} = -1 - \frac{\mathbf{b}_m}{1 - g_m^{2/3}}. \quad (3.49)$$

2) $\mathbf{b}_0 > 0$ and $\mathbf{b}_m < 0$; Eq.(3.48a) can be written as $g_m^{2/3} (1+\mathbf{b}_0) = 1+|\mathbf{b}_0 - |\mathbf{b}_m||$. In this case, the result depends on a relation between the magnitudes of \mathbf{b}_0 and $|\mathbf{b}_m|$, and it yield

$$\text{(a) } g_m^{2/3} (1+\mathbf{b}_0) = 1+\mathbf{b}_0 - |\mathbf{b}_m|, \quad (\mathbf{b}_0)_{2Am} = -1 + \frac{|\mathbf{b}_m|}{1 - g_m^{2/3}} \quad \text{with } \mathbf{b}_0 > |\mathbf{b}_m|; \quad (3.50)$$

$$\text{(b) } g_m^{2/3} (1+\mathbf{b}_0) = 1 - \mathbf{b}_0 + |\mathbf{b}_m|, \quad (\mathbf{b}_0)_{2Bm} = \frac{1 - g_m^{2/3} + |\mathbf{b}_m|}{1 + g_m^{2/3}} \quad \text{with } \mathbf{b}_0 < |\mathbf{b}_m|.$$

3) $b_0 < 0$ and $b_m > 0$; one can find from Eq.(3.48a) $g_m^{2/3} (1+|b_0|) = 1+|b_m| - |b_0|$. Now, the result depends on a relation between the magnitudes of $|b_0|$ and b_m , and it find out

$$(a) \quad g_m^{2/3} (1+|b_0|) = 1+|b_0| - b_m, \quad |b_0|_{3Am} = -1 + \frac{b_m}{1 - g_m^{2/3}} \quad \text{with } |b_0| > b_m; \quad (3.51)$$

$$(b) \quad g_m^{2/3} (1+|b_0|) = 1 - |b_0| + b_m, \quad |b_0|_{3Bm} = \frac{1 - g_m^{2/3} + b_m}{1 + g_m^{2/3}} \quad \text{with } |b_0| < b_m.$$

4) $b_0 < 0$ and $b_m < 0$; one can find from Eq.(48a) $g_m^{2/3} (1+|b_0|) = 1+|b_0| + |b_m|$, so that

$$|b_0|_{4m} = -1 - \frac{|b_m|}{1 - g_m^{2/3}}. \quad (3.52)$$

Now, one can show how to exploit Eqs.(3.49) – (3.52) practically. In so doing, let us take sequentially 4 different situations.

Example A (positive frequency chirp): Let the basic measurement gives $t_{A0} = \sqrt{2/27}$. Then, the first additional measurement, performed with the supplementary element providing $a_1 = 2$ and $b_1 = 1$, gives $t_{A1} = 1/\sqrt{8}$. Exploiting these values, one can find $g_1^{2/3} = 4/3$. Due to $b_1 > 0$, one should consider Eqs.(3.49) and (3.51). The following results can be found

$$a) \quad \text{Eq.(49), } b_0 > 0 : (b_0)_{11} = -1 - \frac{1}{1 - (4/3)} = +2,$$

$$\text{b) Eq.(51) with } |\mathbf{b}_0| > b_1, \mathbf{b}_0 < 0: |\mathbf{b}_0|_{3A1} = -1 + \frac{1}{1 - (4/3)} = -4, \quad (3.53)$$

$$\text{c) Eq.(51b) with } |\mathbf{b}_0| < b_1, \mathbf{b}_0 < 0: |\mathbf{b}_0|_{3B1} = \frac{1 - (4/3) + 1}{1 + (4/3)} = +\frac{2}{7}.$$

Obviously Eq.(3.53b) gives an absurd negative result for modulus, but both Eqs.(3.53a) and (3.53c) can be true, formally speaking. To identify the correct magnitude of \mathbf{b}_0 the second additional measurement should be done. Let it is performed with $a_2 = 3$, $b_2 = 2$ and gives $t_{A2} = 3\sqrt{2}/5\sqrt{5}$. Exploiting these values, one can find $g_2^{2/3} = 5/3$. Due to $b_1 > 0$, one should again consider Eqs.(3.49) and (3.51). It yield

$$\text{a) Eq.(3.49), } \mathbf{b}_0 > 0: (\mathbf{b}_0)_{12} = -1 - \frac{2}{1 - (5/3)} = +2,$$

$$\text{b) Eq.(3.51) with } |\mathbf{b}_0| > b_2: |\mathbf{b}_0|_{3A2} = -1 + \frac{2}{1 - (5/3)} = -6, \quad (3.54)$$

$$\text{c) Eq.(3.51b) with } |\mathbf{b}_0| < b_2: |\mathbf{b}_0|_{3B2} = \frac{1 - (5/3) + 2}{1 + (5/3)} = +\frac{1}{2}.$$

Comparing results of numerical calculations, one can conclude that the final correct result is associated with coinciding with each other estimations from Eqs.(3.53a) and (3.54a). Thus, one should put $\mathbf{b}_0 = +2$ and obtain from each of Eqs.(3.47) that $t_0 = 1$.

Example B (negative frequency chirp): Let the basic measurement gives $t_{A0} = \sqrt{2/27}$ and the second additional measurement, performed with the supplementary element providing again $a_1 = 2$ and $b_1 = 1$,

gives $t_{A1} = 1$. Exploiting these values, one can find $g_1^{2/3} = 2/3$. Due to again $b_1 > 0$, one should consider once again the same Eqs.(3.49) and (3.51). The following numerical data will appear

$$\text{a) Eq.(49), } \mathbf{b}_0 > \mathbf{0} : (\mathbf{b}_0)_1 = -1 - \frac{1}{1 - (2/3)} = -4,$$

$$\text{b) Eq.(51a) with } |\mathbf{b}_0| > b_1, \mathbf{b}_0 < \mathbf{0} : |\mathbf{b}_0|_{3A1} = -1 + \frac{1}{1 - (2/3)} = +2 ; \quad (3.55)$$

$$\text{c) Eq.(3.51b) with } |\mathbf{b}_0| < b_1, \mathbf{b}_0 < \mathbf{0} : |\mathbf{b}_0|_{3B1} = \frac{1 - (2/3) + 1}{1 + (2/3)} = \frac{4}{5} .$$

As before, to identify the correct magnitude of \mathbf{b}_0 the second additional measurement should be done. Let it is performed with $a_2 = 4$, $b_2 = 3$ and gives $t_{A2} = 2$. Exploiting these values, one can find $g_2^{2/3} = 2/3$. Due to $b_1 > 0$, one should once again consider Eqs.(3.49) and (3.51) and obtain

$$\text{a) Eq.(3.49), } \mathbf{b}_0 > \mathbf{0} : (\mathbf{b}_0)_2 = -1 - \frac{3}{1 - (2/3)} = -10,$$

$$\text{b) Eq.(3.51a) with } |\mathbf{b}_0| > b_1, \mathbf{b}_0 < \mathbf{0} : |\mathbf{b}_0|_{3A2} = -1 + \frac{3}{1 - (2/3)} = +8 ; \quad (3.56)$$

$$\text{c) Eq.(3.51b) with } |\mathbf{b}_0| < b_1, \mathbf{b}_0 < \mathbf{0} : |\mathbf{b}_0|_{3B2} = \frac{1 - (2/3) + 3}{1 + (2/3)} = +2 .$$

The comparison of numerical results from Eqs.(3.55) and (3.56) shows that the final correct result is associated with coinciding with each other estimations from Eqs.(3.55b) and (3.56c). Thus, one should put $\mathbf{b}_0 = -2$ and obtain from each of Eqs.(3.47) that $t_0 = 1$.

3.6. Conclusion

The presented work develops the above-described avenue in practically very important case of low-power picosecond pulses with the sech-like shape inherent in just optical solitons. For this purpose, at first the problem is formulated in terms of the joint Wigner time-frequency distributions for the sech-like pulses [11]. At first, it consider such distributions for the slowly varying amplitudes and then, generalize them on the sech-like pulses with a high-frequency filling. In both these cases, all the values including the contributions from internal frequency modulation of pulses are described in terms of square-average magnitudes.

The developed analysis makes it possible to interpret potential experimental data in terms of the Wigner distributions and/or restore these distributions using the experimental results. Together with this, the corresponding approach to the field strength auto-correlation function of the second order is formulated in the same terms as well. Finally, is presented a novel interferometric technique of measuring the train-average pulse width as well as the value and sign of the frequency chirp inherent in low-power picosecond optical solitons belonging to high-repetition-rate trains.

Basic peculiarities of the technique under proposal are connected with rather specific algorithm of measurements having a two-beam interferometry into its background, with exploiting a specially designed supplementary semiconductor cell, and with carrying out two additional measures involving this semiconductor cell into the scheme of a two-beam scanning Michelson interferometer.

3.7 References

- [1]. M.B. Priestley *Spectral analysis and time series*. (Academic Press, London – New-York, 1982).
- [2]. D.B.Percival and A.T.Walden. *Spectral Analysis for Physical Applications: Multitaper and Conventional Univariate Techniques*. (Cambridge University Press, Cambridge, 1993).
- [3]. P.F.Dunn, *Measurement and Data Analysis for Engineering and Science*. (McGraw–Hill, New-York, 2005).
- [4]. J.-C. Diels and W. Rudolph. *Ultrashort laser pulse phenomena: fundamentals, techniques and applications on a femtosecond time scale*. (Academic Press, Boston, 1996).
- [5]. K.W. DeLong and R. Trebino, “Frequency-resolved optical gating with the use of second-harmonic generation.” *J. Opt. Soc. Am. B*. **1994**, vol.,11, 2206 – 2215.
- [6]. C. Iaconis and I.A. Walmsley, “Spectral phase interferometry for dielectric electric-field reconstruction of ultrashort optical pulses.” *Opt. Lett.* **1998**, vol.23, 792 - 794.
- [7]. J.Dai, H.Teng and Ch.Guo. “Second- and third-order interferometric autocorrelations based on harmonic generations from metal surfaces.” *Opt. Communications*. **2005**,vol.205, 173-178.
- [8]. E.P. Ippen and C.V. Shank In: S.L. Shapiro, Editor, *Ultrashort light pulses*, (Springer, New York, 1977).
- [9]. A.S.Shcherbakov, Synchronization of a radio-interferometer by the high-repetition-rate picosecond solitons, *Tech.Phys. Lett.*, **1993**,vol.19, 615-616.
- [10]. J. Herrmann and B.Wilhelmi, *Laser fur Ultrakurze Lichtimpulse*, (Akademi-Verlag, Berlin, 1984).
- [11]. D.Dragoman, Redundancy of phase-space distribution functions in complex field recovery problems, *Applied Optics*,**2003**, vol.42, no.11, 1932-1937.
- [12]. L.Cohen. “Time-frequency distributions: a review.” *Proc.IEEE*, **1989**,vol.77, no.7, 941-981.

- [13]. A.P.Prudnikov, Yu.A.Brychkov, and O.I.Marichev. *Integrals and Series*, (Gordon & Breach Science Publishers, Amsterdam, 1998), vol.1, Elementary Functions.
- [14]. S.A.Akhmanov, V.A.Vysloukh, and A.S.Chirkin. *Optics of Femtosecond Laser Pulses*. Moscow, Nauka, 1988, [Translated into English (New York: AIP, 1992)].
- [15]. G.A.Korn and T.M.Korn. *Mathematical Handbook*, (McGraw-Hill Comp., New-York, 1968), Chapter 21.
- [16]. J.-C.Diels, J.J.Fontaine, I.C.McMichel, Control and measurement of ultrashort pulse shapes (in amplitude and phase) with femtosecond accuracy, *Appl. Opt.*,**1985**, vol.24, 1270-1282.
- [17]. K.Nagamuna, K.Mogi, H.Yamada, General method for ultrashort light pulse chirp measurement, *IEEE J. Quantum Electron.*,**1989**, vol.25, 1225-1233.
- [18]. D.J.Kame, R.Trebino, Single-shot measurement of the intensity and phase of a femtosecond laser pulse, *Proc. SPIE*, **1993**, vol.1861, 150-160.
- [19]. E.L.Portnoy, S.D.Yakubovich, N.M.Stelmakh, Dynamics of emission of radiation from a hetero-laser with a saturable absorber formed by deep implantation of oxygen ions, *Phys. Semicond.*, **1998**, vol.22, no.7, 766-768.
- [20]. G.P.Agrawal and N.K.Dutta, *Semiconductor lasers*, (Van Nostrand Reinhold, New-York, 1993).
- [21]. I.A.Kniazev, A.S.Shcherbakov, Yu.V.II'in, Picosecond pulse source based on a semiconductor laser with a fiber cavity, *Tech. Phys. Lett.*, **1991**, vol.17, 82-83.
- [22]. E.I.Andreeva, A.S.Shcherbakov, I.E.Berishev, Semiconductor source of picosecond pulses at a wavelength of 1.55 μm , *Tech. Phys. Lett.*,**1992**, vol.18, 803-804.
- [23]. A.S.Shcherbakov and E.I.Andreeva, Observation of picosecond optical pulses with a guiding-center soliton in a single-mode optical fiber wave-guide, *Tech. Phys. Lett.*,**1994**, vol.20, 873-875.

[24] A.S.Shcherbakov, A.L.Muñoz Zurita, A. Y. Kosarsky, J. Campos Acosta.“ A new interferometric technique for determining the time frequency parameters inherent in low-power bright picosecond optical pulses with a sech-like shape”, (Submitted Article Manuscripts to Journal of Modern Optics).

[25] A.S.Shcherbakov, A.L.Muñoz Zurita, and J.Campos Acosta. “A new technique of measuring low-power picoseconds optical pulse trains”. The 2007 SPIE Photonics North Conference (June 4-7, 2007, Ottawa, Canada), Technical Program, p.191, #PD-6-14-2 (2007).

CHAPTER 4

APPLYING A TRIPLE AUTO-CORRELATION TO MEASURING THE ENVELOPES OF ULTRASHORT OPTICAL PULSES

It considers an opportunity of measuring the train-averaged parameters of picosecond optical pulses with both symmetric and asymmetric envelopes being arranged in high-frequency repetition trains and corrupted by additive Gaussian noise. In so doing, one can exploit the temporal triple auto-correlation function, whose Fourier transformation gives the bispectrum of signal.

The advantages of similar auto-correlation functions consist in the capability of recovering various signals almost unambiguously and low sensitivity of these functions to noise. It implements the technique and algorithmic investigation for recognizing the width as well as the magnitude and the sign of the frequency chirp peculiar to pulses with Gaussian-like, rectangular, and smooth asymmetric shapes.

4. 1. Triple auto-correlation

The triple auto-correlation of an ordinary function on the real time is the integral of the product of that function with two independently shifted copies of itself. Triple auto-correlation methods are frequently used in signal processing for treating signals that are corrupted by additive Gaussian noise; in particular, triple auto-correlation techniques perform well when multiple observations of the signal are

available and the signal may be translating in between the observations, e.g. a sequence of images of an object translating on a noisy background.

The triple auto-correlation particularly suitable for such tasks have three properties: (1) it is invariant under translation of the underlying signal; (2) it is almost insensitive to additive Gaussian noise; and (3) it retains most of the phase information in the underlying signal [1].

The triple auto-correlation is less popular than the standard correlation for several reasons: the triple auto-correlation is sometimes too difficult to process and to observe. Triple auto-correlation is small for many bipolar or complex signals, than mathematics associated with triple auto-correlation is better known.

On the other hand, the triple auto-correlation knows more about the signal than does the ordinary auto-correlation. The triple auto-correlation is very important because the underlying mathematical tools and report presents where triple auto-correlation was employed for studying for example the pulses shapes, astronomical speckle interferometry [2].

Another case is the intensity distribution at the exit of a Young-Michelson interferometer is analyzed in Fourier domain. It shows that two numbers are necessary for describing properly the variation of the visibility of the interferogram fringes.

One of them is the complex degree of spatial coherence, which describes the correlation between the contributions from the Young's slits. The second number describes the correlation between the Young's interferograms reflected by the mirrors of the Michelson interferometer, that is, the correlation

of optical fields that contain another correlation term. It has long been recognized that the term coherence plays a fundamental role in optics, in order to denote the correlation properties to different orders of the optical field.

Furthermore, it is accepted today that complete coherence requires significant correlation values to an infinite succession of orders [1,2] So, spatial coherence properties revealed by a simple Young's experiment are referred to as second order spatial coherence. It describes the tendency of two values of the optical field at distantly separated points to take on correlated value. Its basic quantity is the complex degree of spatial coherence [3].

4.2. The triple auto-correlation function for a one-dimensional signal

The triple auto-correlation function of the signal $F(t)$ is determined by the following integral

$$F_3(t_1, t_2) = \int_{-\infty}^{\infty} F(t)F(t+t_1)F(t+t_2) dt . \quad (4.1)$$

The Fourier transformation of Eq.(4.1) with the kernel $\exp[-2\pi i(f_1 t_1 + f_2 t_2)]$ gives the bispectrum

$$a) F_3(f_1, f_2) = F(f_1)F(f_2)F(-f_1 - f_2) , \quad b) F(f) = \int_{-\infty}^{\infty} F(t) \exp[-2\pi i f t] dt , \quad (4.2)$$

where $F(f)$ is the spectrum of signal. The bispectrum $F_3(f_1, f_2)$ has two following symmetries

$$\mathbf{F}_3(\mathbf{f}_1, \mathbf{f}_2) = \mathbf{F}_3(\mathbf{f}_2, \mathbf{f}_1) = \mathbf{F}_3(-\mathbf{f}_1 - \mathbf{f}_2, \mathbf{f}_1), \quad (4.3)$$

which lead to the redundancy of three fourths of the frequency plane $(\mathbf{f}_1, \mathbf{f}_2)$ with determining the bispectrum $\mathbf{F}_3(\mathbf{f}_1, \mathbf{f}_2)$. For a real-valued temporal signal $\mathbf{F}(t)$, both the spectrum $\mathbf{F}(f)$ and bispectrum $\mathbf{F}_3(\mathbf{f}_1, \mathbf{f}_2)$ are Hermitian self-conjugate functions, i.e.

$$\text{a) } \mathbf{F}(f) = \mathbf{F}^*(-f), \quad \text{b) } \mathbf{F}_3(\mathbf{f}_1, \mathbf{f}_2) = \mathbf{F}_3^*(-\mathbf{f}_1, -\mathbf{f}_2), \quad (4.4)$$

so that just in this particular case even one eighth of the frequency plane $(\mathbf{f}_1, \mathbf{f}_2)$ is quite enough for determining the bispectrum $\mathbf{F}_3(\mathbf{f}_1, \mathbf{f}_2)$.

If a system is linear in behavior and temporally invariant relative to the signal $\mathbf{F}(t)$, this system is linear in behavior and temporally invariant relative to the triple auto-correlation function as well.

It follows from the constraint equation coupling the input and output temporal signals, $\mathbf{F}_{\text{in}}(t)$ and $\mathbf{F}_{\text{out}}(t)$, through the response function $\mathbf{P}(t)$, namely,

$$\text{a) } \mathbf{F}_{\text{out}}(t) = \int_{-\infty}^{\infty} \mathbf{F}_{\text{in}}(t - \tau) \mathbf{P}(\tau) d\tau, \quad \text{b) } \mathbf{F}_{\text{out}}(f) = \mathbf{F}_{\text{in}}(f) \mathbf{P}(f). \quad (4.5)$$

It is seen from Eqs.(4.2) and (4.5b) that $\mathbf{F}_{3, \text{out}}(\mathbf{f}_1, \mathbf{f}_2) = \mathbf{F}_{3, \text{in}}(\mathbf{f}_1, \mathbf{f}_2) \mathbf{P}_3(\mathbf{f}_1, \mathbf{f}_2)$, so that

$$\mathbf{F}_{3, \text{out}}(t_1, t_2) = \int_{-\infty}^{\infty} \int_{-\infty}^{\infty} \mathbf{F}_{3, \text{in}}(t_1 - t_1, t_2 - t_2) \mathbf{P}_3(t_1 - t_1, t_2 - t_2) dt_1 dt_2, \quad (4.6)$$

where $\mathbf{P}_3(t_1, t_2)$ and $\mathbf{P}_3(f_1, f_2)$ are the corresponding response functions.

Then, Eq.(4.2) shows that the bispectrum becomes to be not varied when an arbitrary exponential factor is included into the spectrum of the temporal signal. Let us take $\mathbf{F}^S(f) = \mathbf{F}(f) \exp(gf)$, where g is an arbitrary complex-valued constant. In this case, one can calculate

$$\mathbf{F}_3^S(f_1, f_2) = \mathbf{F}^S(f_1) \mathbf{F}^S(f_2) \mathbf{F}^S(-f_1 - f_2) = \mathbf{F}(f_1) \mathbf{F}(f_2) \mathbf{F}(-f_1 - f_2) \exp[g(f_1 + f_2 - f_1 - f_2)] = \mathbf{F}_3(f_1, f_2) \quad (4.7)$$

This example demonstrates that the process of recovering the signal from the triple auto-correlation function or the bispectrum can be not always unambiguous and conclusive.

Now, one can illustrate these considerations by a few particular graphical cases. Figures 4.1 and 4.2 demonstrate the envelopes, triple auto-correlations, and bispectra for typical Gaussian and rectangular pulses of unit width given by

$$\text{a) } \mathbf{F}^G(t) = \exp\left(-t^2/2\right), \quad \text{b) } \mathbf{F}^R(t) = q(x + 0.5) - q(x - 0.5), \quad (4.8)$$

The corresponding analytical expressions describing Figs. 4.1b, 4.1c, 4.2b, and 4.2c are described by

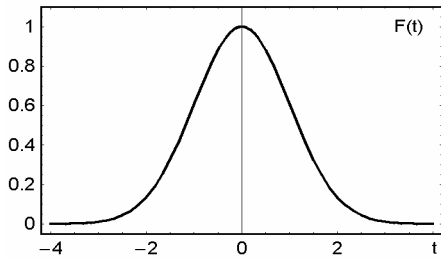
$$\text{a) } F_3^G(t_1, t_2) = \sqrt{\frac{2p}{3}} \exp\left\{-\frac{p}{3} (t_1^2 + t_2^2 - t_1 t_2)\right\} \dot{u},$$

$$\text{b) } F_3^G(f_1, f_2) = (2p)^{3/2} \exp\left\{-4p^2 (f_1^2 + f_2^2 + f_1 f_2)\right\} \dot{u},$$

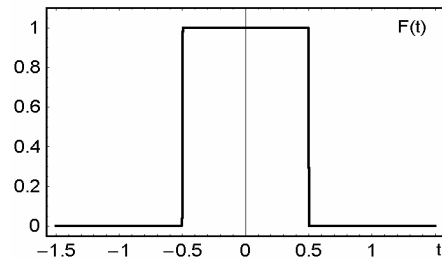
$$\text{c) } F_3^R(t_1, t_2) = 0.25 \left[\text{sign}(t_1 - t_2 - 1) (|1 - t_1| - |1 + t_2| + |t_1| - |t_2|) + \text{sign}(t_1 - t_2 + 1) \times \right.$$

$$\left. (|1 + t_1| + |1 - t_2| - |t_1| - |t_2|) + \text{sign}(t_1 - t_2) (|1 - t_1| - |1 + t_1| + |1 + t_2| - |1 - t_2|) \right],$$

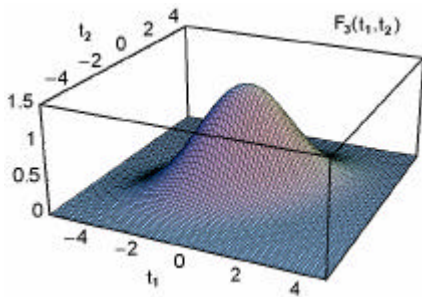
$$\text{d) } F_3^R(f_1, f_2) = \frac{\sin(pf_1)}{pf_1} \frac{\sin(pf_2)}{pf_2} \frac{\sin[p(f_1 + f_2)]}{p(f_1 + f_2)}. \quad (4.9)$$



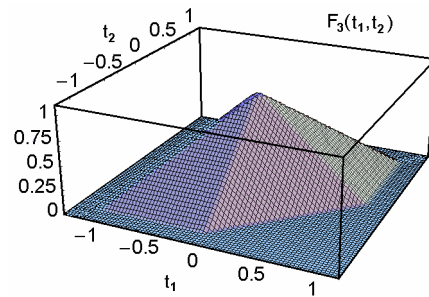
a.



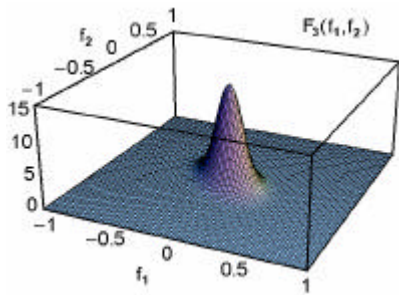
a.



b.

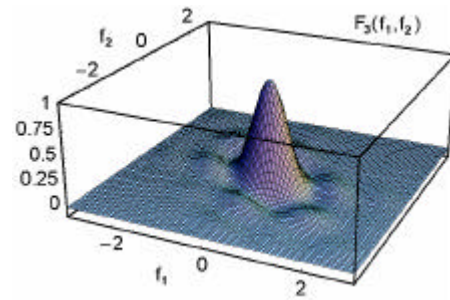


b.



c.

Figure 4.1. The envelope, triple auto-correlation, and bispectrum for real Gaussian pulse.



c.

Figure 4.2. The envelope, triple auto-correlation, and bispectrum for real rectangular pulse.

4.3. The triple auto-correlation function for the chirped Gaussian pulse

In this section, let us consider triple auto-correlation and bispectrum for the chirped Gaussian pulse given by

$$\mathbf{F}^G(\mathbf{t}) = \exp\left\{ \frac{\dot{\epsilon}}{\epsilon} (-\mathbf{a} + i\mathbf{b}) \mathbf{t}^2 \right\} \frac{\dot{\mathbf{u}}}{\mathbf{u}}, \quad (4.10)$$

where the parameters \mathbf{a} and \mathbf{b} characterize the pulse width and the frequency chirp, respectively. Substituting Eq.(4.10) into Eq.(4.1), one can find that

$$a) F_3^G(t_1, t_2) = \sqrt{\frac{p(a+ib)}{3(a^2+b^2)}} \exp\left\{\frac{2}{3}(a+ib)(t_1^2+t_2^2-t_1t_2)\right\} \quad (4.11)$$

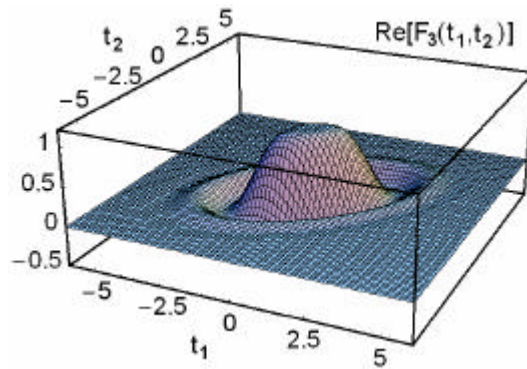
Then, one can use Eq.(4.2) to obtain the corresponding bispectrum

$$b) F_3^G(f_1, f_2) = \frac{p(a+ib)}{a^2+b^2} \exp\left\{-\frac{2p^2(a+ib)}{a^2+b^2}(f_1^2+f_2^2+f_1f_2)\right\} \quad (4.12)$$

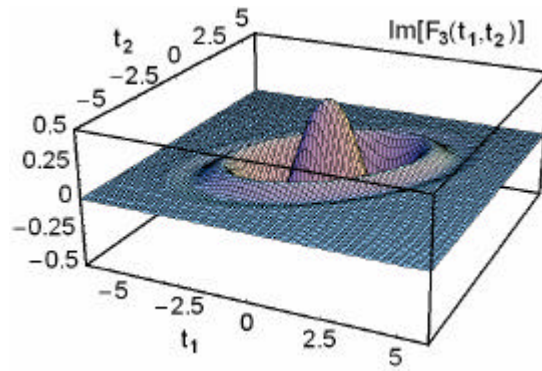
Dividing real and imaginary parts of Eq.(4.11), one can write for the triple correlation, see Fig.4.3.

$$\text{Re} [F_3^G(t_1, t_2)] = \sqrt{\frac{p}{3\sqrt{a^2+b^2}}} \exp\left\{\frac{2a}{3}(t_1^2+t_2^2-t_1t_2)\right\} \cos\left\{\frac{2b}{3}(t_1^2+t_2^2-t_1t_2)\right\} + \frac{1}{2} \arctan \frac{b}{a} \quad (4.13)$$

$$\text{Im} [F_3^G(t_1, t_2)] = \sqrt{\frac{p}{3\sqrt{a^2+b^2}}} \exp\left\{\frac{2a}{3}(t_1^2+t_2^2-t_1t_2)\right\} \sin\left\{\frac{2b}{3}(t_1^2+t_2^2-t_1t_2)\right\} + \frac{1}{2} \arctan \frac{b}{a} \quad (4.14)$$



a.



b.

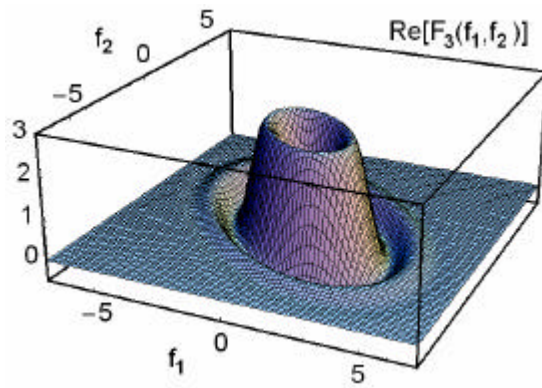
Figure 4.3. Triple auto-correlation function for the chirped Gaussian pulse with $a = 0.5$ and $b = 1.0$:

(a) real-valued part, (b) imaginary-valued part.

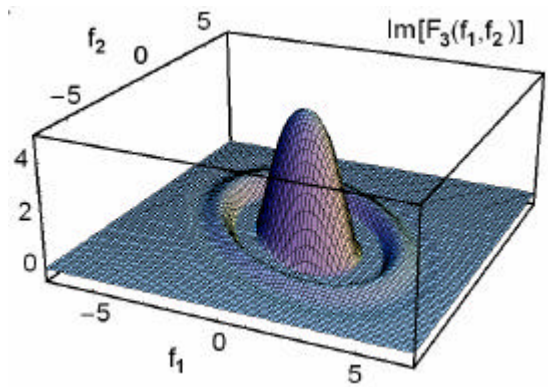
After that, dividing real and imaginary parts of Eq.(4.12), one can write for the corresponding bispectrum

$$\text{Re} \left[F_3^G(f_1, f_2) \right] = \frac{p^{3/2}}{(a^2 + b^2)^{3/4}} \exp \left[-\frac{2p^2 a (f_1^2 + f_2^2 + f_1 f_2)}{a^2 + b^2} \right] \cos \left[-\frac{2p^2 b (f_1^2 + f_2^2 + f_1 f_2)}{a^2 + b^2} + \frac{3}{2} \arctan \frac{b}{a} \right] \quad (4.15)$$

$$\text{Im} \left[F_3^G(f_1, f_2) \right] = \frac{p^{3/2}}{(a^2 + b^2)^{3/4}} \exp \left[-\frac{2p^2 a (f_1^2 + f_2^2 + f_1 f_2)}{a^2 + b^2} \right] \sin \left[-\frac{2p^2 b (f_1^2 + f_2^2 + f_1 f_2)}{a^2 + b^2} + \frac{3}{2} \arctan \frac{b}{a} \right] \quad (4.16)$$



a.



b.

Figure 4.4 Bispectrum for the chirped Gaussian pulse with $a = 0.5$ and $b = 1.0$:

(a) real-valued part, (b) imaginary-valued part.

4.4 The algorithm of recovering the temporal signal from its triple auto-correlation function.

If the temporal signal $F(t)$ is, for example, real-valued as well as is of a finite extent, it can be retrieved from its triple auto-correlation function $F_3(t_1, t_2)$ almost uniquely apart from a shift. For a real signal $F(t)$ of finite extent, its spectrum $F(f)$ can be analytically continued by extending the frequency f to the complex variable $z = z^c + i z^i$. The analytic continuation $F(z)$ is determined by its complex zeros z_n and can be written as a Hadamard product

$$F(z) = \exp(a + bz) \prod_n \tilde{O}(z - z_n) \exp\left\{ \frac{z}{z_n} \right\} \quad (4.17)$$

where a and b are some constants. This fundamental equation from the theory of complex functions cannot be applied directly to any arbitrary function of two variables. However, in the case of triple

correlations, it is known how the two-dimensional function $F_3(z_1, z_2)$ is related to the one-dimensional function $F(z)$, because one can exploit Eq.(4.2), so that one can write

$$F_3(z_1, z_2) = F(z_1)F(z_2)F(-z_1 - z_2) . \quad (4.18)$$

Consequently, one can insert Eq.(4.17) into Eq.(4.18) and obtain

$$F_3(z_1, z_2) = \exp(3a) \prod_n \tilde{O}(z_1 - z_n)(z_2 - z_n)(-z_1 - z_2 - z_n) . \quad (4.19)$$

Using Eq.(4.19), one can derive the particular complex zeros of $F(z)$ from the complex zero subspaces of $F_3(z_1, z_2) = 0$. Once the zeros z_n are known, one can compute $F(z)$, hence $F(f)$, and then $F(t)$. The detailed consideration of this proof shows that for the general case of the complex-valued function $F(t)$, its spectrum $F(f)$ can be reconstructed up to the exponential factor $\exp(a + bf)$, where the factor b is an arbitrary, broadly speaking complex-valued, constant, while $a = \{0, 2\pi i - (1/3), 2\pi i - (2/3)\}$.

One can consider a retrieval algorithm. For the sake of simplicity let us assume reality of the signal $F(t)$ and hence Hermitian symmetry of its spectrum $F(f)$, see Eq.(4.4a). It begins by assuming that $f_2 = 0$ in a bispectrum $F_3(f_1, f_2)$, consequently

$$F_3(f_1, 0) = F(f_1)F(0)F(-f_1) = |F(f_1)|^2 F(0) \quad (4.20)$$

and therefore the Fourier amplitude $|F(f)|$ is available directly on the f_1 -axis of $F_3(f_1, f_2)$.

Then, one can retrieve the Fourier phase $j(f)$, defined by $F(f) = |F(f)| \exp[j(f)]$. To that end it concentrate on a straight line, being parallel to the f_1 -axis, but above it by one sampling step df

$$F_3(f_1, df) = F(f_1)F(df)F(-f_1 - df) = F(df) \times |F(f_1)F(-f_1 - df)| \exp[ij(f_1) - ij(f_1 + df)]. \quad (4.21)$$

Defining $j_3(f_1, f_2)$ as the phase of the bispectrum $F_3(f_1, f_2)$, one can derive from Eq.(4.21) the following phase equation

$$j_3(f_1, f_2) = j(df) + [j(f_1) - j(f_1 + df)]. \quad (4.22)$$

Finally, one can extract $j(f_1)$ itself, apart from an additive constant, and a term linear in f_1 , that reflects the lack of knowledge about t_0 in $F(t - t_0)$.

4.5. Application to the characterization of picosecond optical pulses

A few years ago it became possible to generate optical pulses whose widths lie in pico- and femtosecond ranges. Since a new field of researches had been developed, and now the pulse durations reported by experiments are approaching the theoretical limits [4,5].

Nevertheless, up to now there are no detectors being fast enough to measure such ultrashort pulses directly. That is why a lot of the elaborated methods of measuring are based on the analysis of various auto-correlation functions.

Unfortunately, the auto-correlation functions of the second order is symmetric in behavior, so that they cannot give us any information about asymmetry if optical pulses under investigation.

At this point, one can benefit from a triple auto-correlation, which can provide the true pulse shape. A triple-intensity correlation interferometer is shown in Fig.4.5.

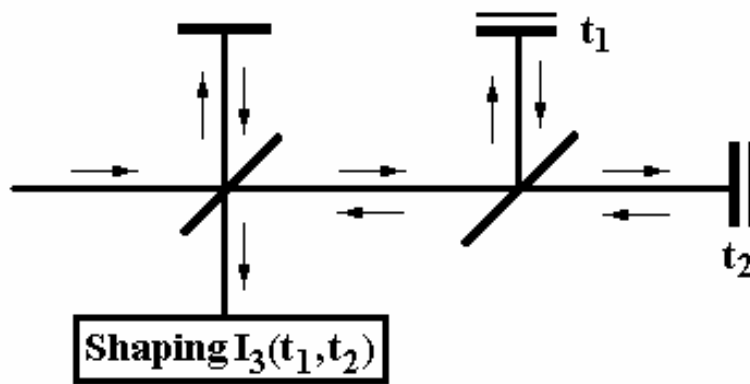


Figure 4.5. A three-beam interferometer for registering the intensity triple auto-correlation function of a high-repetition train of ultrashort optical pulses.

This interferometer can be exploited to record the raw data of the experiments with a sequence of ultrashort optical pulses.

The triplet of arms of this interferometer provides mutually delayed pulse trains with the intensities $I(t+t_1)$ and $I(t+t_2)$ together with the non-delayed one $I(t)$. Mixing these three pulse trains on nonlinear crystal with the resulting third-harmonic generation, one can obtain the intensity triple auto-

correlation function. The third-harmonic generation is possible to obtain of different forms, see Fig 4.6 and Fig 4.7.



Figure 4.6 Direct third harmonic generation

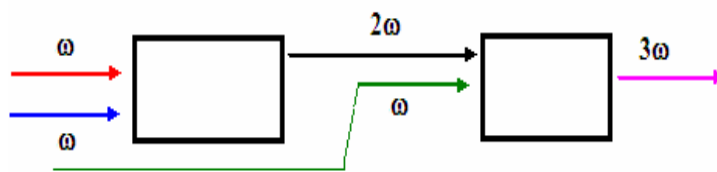


Figure 4.7 Cascade third harmonic generation

Once the intensity triple auto-correlation function of the optical pulses is known, the pulse shape $I(t)$ can be reconstructed using the algorithm described the previous section.

In the figure 4.8 illustrates the corresponding steps of such a reconstruction. Thus, this technique makes possible measuring asymmetric envelopes of ultrashort optical pulses and recovering signals almost unambiguously.

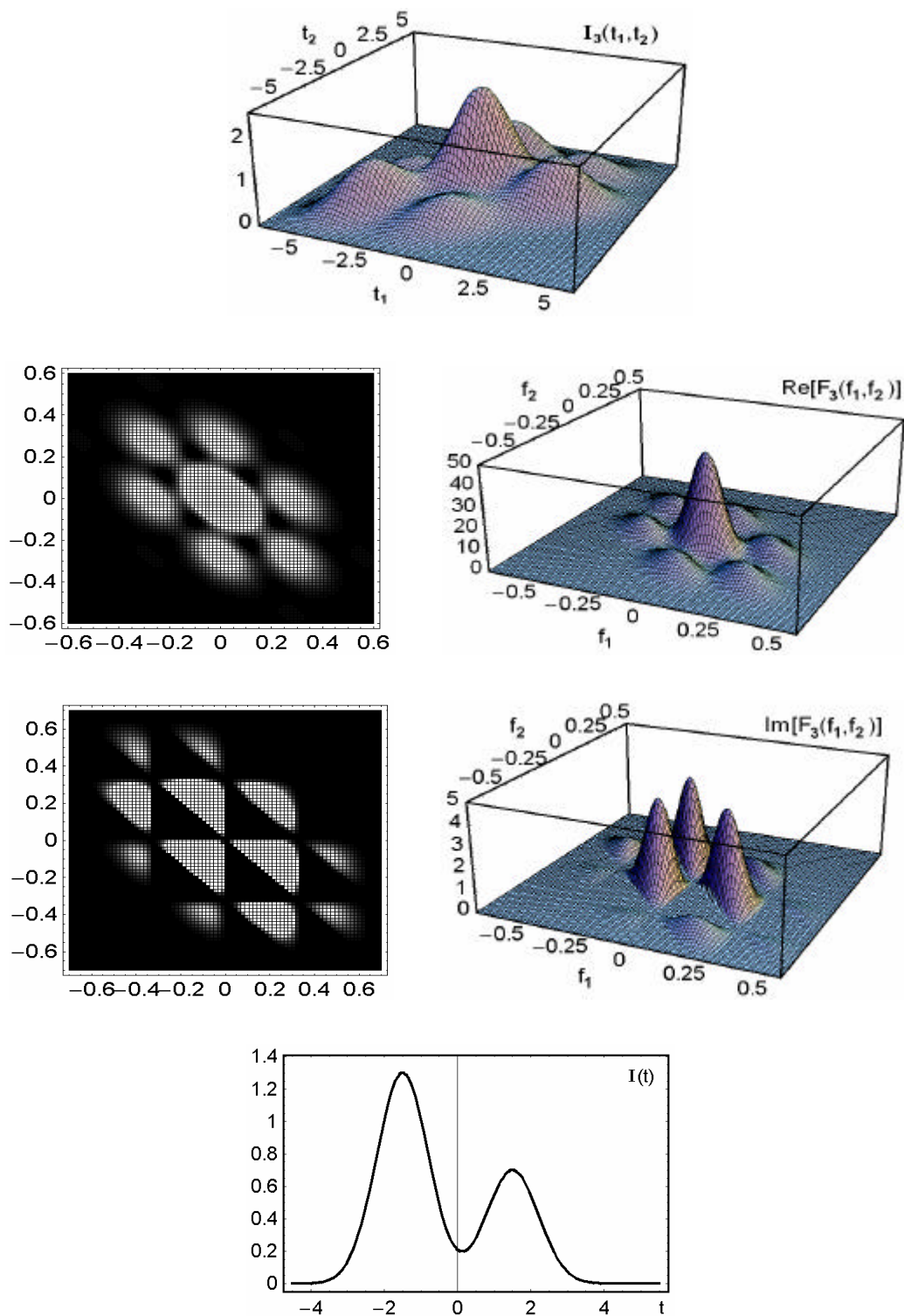


Figure 4.8. The steps of reconstructing an asymmetric optical pulse: the upper insert is for the triple auto-correlation function; then, two inserts are for real and imaginary parts of the bispectrum; the bottom insert is for the reconstructed pulse.

4.6. Conclusions

The intensity triple auto-correlation function of the optical pulses is known, the pulse shape $I(t)$ can be reconstructed using the algorithm described in this article. Figure 4.6 illustrates the corresponding steps of such a reconstruction. Thus, this technique makes possible measuring asymmetric envelopes of ultrashort optical pulses and recovering signals almost unambiguously. It used the phase of the different pulse and with this is possible to observe better behavior or form of the pulse and it has more details in the reconstruction of these pulses.

Now it has a new technique it is base in the triple correlation and is possible to create the algorithm by the measurement. In this case is using the technique of interferometer, with the measurements and the use of the triple correlation.

4.7. References

- [1] A.S.Shcherbakov, A.L.Munoz Zurita, and A.Yu.Kosarsky. *“Describing and measuring the time-frequency parameters of low-power bright picoseconds optical pulses using the interferometric technique.”* Proc. of SPIE, Vol.6292-95, 62921H, p.1-11 (2006).
- [2]. R Kakarala. Triple correlation on groups. Ph.D. Thesis University of California Irvine (1992).
- [3] E.P.Ippen and C.V.Schenk, “Picosecond Techniques and Applications.” in *Ultrashort Light Pulses*, Ed. by S.Shapiro, (Springer, Heidelberg, 1977).
- [4] A.S.Shcherbakov. “Synchronization of a radio-interferometer by the high-repetition-rate picosecond solitons.” Tech.Phys. Lett., vol.19, 615-616 (1993).

- [5] E.I.Andreeva, A.S.Shcherbakov, I.E.Berishev, et al. “Semiconductor source of picosecond pulses at a wavelength of 1.55 μm .” Tech. Phys. Lett., vol.18, 803-804 (1992).
- [6] A.S.Shcherbakov and E.I.Andreeva. “Observation of picosecond optical pulses with a guiding-center soliton in a single-mode optical fiber wave-guide.” Tech. Phys. Lett., vol.20, 873-875 (1994).
- [7] A.S.Shcherbakov, A.L.Muñoz Zurita, S.A.Nemov, and J.Campos Acosta. “*Applying a triple correlation to measuring the envelopes of ultrashort optical pulses*”. Proc. of the XXII SOMI Congress, ASSXXII-75, p.1-5, 2007.
- [8] A.L.Muñoz Zurita, A.S.Shcherbakov, Sergey A. Nemov , E. Tepichin Rodriduez and J. Campos Acosta, “*Applying the triple correlation functions to characterizing high-frequency repetition trains of picosecond optical pulses*”, Proc. of SPIE, Vol.7072, p.1-9 (2008).
- [9] A.S.Shcherbakov, A.L.Munoz Zurita, and A.Yu.Kosarsky. “*Describing and measuring the time-frequency parameters of low-power bright picoseconds optical pulses using the interferometric technique.*” The 2006 SPIE Optics and Photonics Conference (August 13 – 17, 2006, San Diego, CA, USA), Technical Program, p.45, #6292-59 (2006).
- [10] A.S.Shcherbakov, A.L.Muñoz Zurita, A.Luna Castellanos, S.A.Nemov, and J.Campos Acosta. “*Applying a triple correlation to measuring the envelopes of ultrashort optical pulses*”. The 2007 SPIE Photonics North Conference (June 4-7, 2007, Ottawa, Canada), Technical Program, p.217, #PDS-5-9-4 (2007).
- [11] A.L.Muñoz Zurita, A.S.Shcherbakov, Sergey A. Nemov , E. Tepichin Rodriduez and J. Campos Acosta, “*Applying the triple correlation functions to characterizing high-frequency repetition trains of picosecond optical pulses*”, The 2008 SPIE Optics and Photonics Conference (August 9 – 13, 2008, San Diego, CA, USA), Technical Program, p.40, (2008).

CHAPTER 5.

ANALYSIS OF SILICON PHOTODIODES SPECTRAL REFLECTANCE FOR RESPONSIVITY SCALES.

Silicon photodiodes have very good radiometrical features and are more sensitive and quicker than thermal detectors. For these reasons silicon photodiodes are used in many applications where optical radiation has to be measured in the spectral range from 300 nm to 1000 nm and particularly to maintain scales of spectral responsivity in different laboratories, including international metrology laboratories [1,2]. Photodiode's reflectance plays an important roll regarding the relation between responsivity and the incident flux, because the detector signal depends on the absorbed radiation, but it is used to know the incident radiation, so the reflected part of the radiation has to be considered.

Although every photodiode to be used in a device to measure optical radiation has to be calibrated and manufacturers give information about typical responsivity values that can be expected from their photodiodes, it is interesting to measure the reflectance of diodes from the same manufacturer and see whether the reflectance change explains the variability in responsivity claimed by the manufacturer. Furthermore, to know how much the reflectance change among diodes of the same batch is interesting in order to select the diodes for silicon trap detectors [3,4]. These detectors, widely used in high accuracy radiometric measurements, are formed by 3 or 5 photodiodes (depending on the configuration) and are built in such a way that radiation regularly reflected by one photodiode impinges

on the following one and so on. After 5 reflections the amount of non absorbed radiation is negligible compared to the incoming one and because of that the device is called a “radiation trap detector”. If the device is configured in such a way that the third photodiode is placed at normal incidence, then the 5 reflections can be obtained with only 3 photodiodes that must not be in the same plane in order to have the same total reflectance for any polarization state [6,7]. To fulfill this requirement it is also needed that the first and second photodiodes have the same reflectance. Therefore if photodiodes’ reflectance within a batch changes from item to item, it will be necessary to measure their reflectance to select them for using them in silicon trap detectors, while if the reflectance is constant this measurement will not be necessary.

In the other hand it is also interesting to know whether the responsivity ageing observed in silicon photodiodes is related to reflectance changes in addition to internal quantum efficiency change, whose stability has been studied by other authors [8,9]. To know the origin of the ageing is very important in order to be able to minimize it.

Therefore in this work it analyzes how the spectral reflectance changes among photodiodes from the same manufacturer and batch and how the reflectance of three standard photodiodes has drifted after six years. The results obtained show reflectance changes from diode to diode within the same batch and also show that reflectance of photodiodes changes on time. This ageing is also spectrally dependent.

5.1 Photodiode spectral reflectance.

From an optical point of view, a silicon photodiode can be considered as a layered structure as shown in figure 5.1.

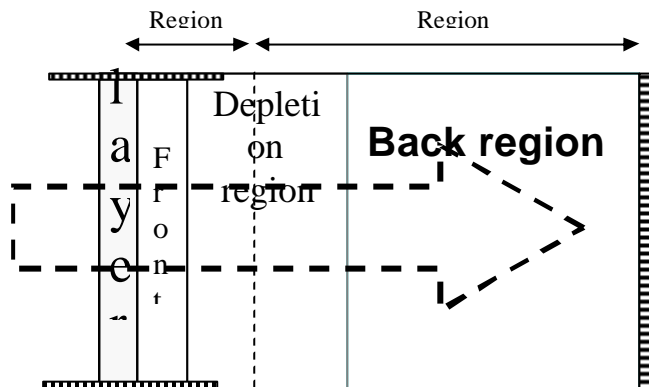


Figure 5.1 Silicon photodiode structure.

The first layer, the passivation layer, is made of silicon oxide and is transparent to the optical radiation within the spectral range in which silicon photodiodes are sensitive. The other layers are the absorbing layers, made of silicon with different dopants: phosphor in region n and boron in region p. Therefore the reflectance of these devices can be obtained as the reflectance of a transparent layer of a given thickness over an absorbing layer whose thickness, in principle, may be considered infinity. According to reference 5 the such reflectance is given by:

$$r = \frac{r_{12}^2 + r_{23}^2 + 2 r_{12} r_{23} \cos (f_{23} + 2b)}{1 + r_{12}^2 r_{23}^2 + 2 r_{12} r_{23} \cos (f_{23} + 2b)} \quad (5.1)$$

Where r_{12} is the reflection coefficient between air and the silicon oxide layer, r_{23} is the one between silicon oxide and silicon, f_{23} is the phase change produced between the silicon oxide and the silicon and $b = 2\pi n_2 h \cos(\theta_2) / \lambda_0$, with h the thickness and n_2 the refractive index of the oxide layer and θ_2 the angle of refraction.

Looking at the previous equation and considering that refractive index of doped silicon is assumed to be equal to that of undoped silicon, the variability in reflectance could be due to variations in the oxide thickness.

Because of that, to approach the first objective, the study was restricted to a single manufacturer, since the thickness of the passivation layer may be differently designed by different manufacturers. Photodiodes from Hamamatsu were chosen, because they are the most stable and most used in many international laboratories. Furthermore photodiodes from just one batch have been used to avoid as much as possible changes in the oxide thickness which in turn produce different reflectance values.

To achieve the second goal, the ageing of photodiodes, the reflectances of three silicon photodiodes have been measured. Those photodiodes are also from Hamamatsu and are used to maintain the scale of spectral responsivity of Institute for Applied Physics (CSIC),

Looking at the reflectance equation and bearing in mind the layered structure of silicon photodiodes and the high refractive index values, it is noticeable to remark that photodiode's response notably depends on the angle of incidence and the polarization state of the incoming radiation [10,11].

5.2 Experimental setup for reflectance measurement.

To measure the photodiodes reflectance an experimental setup as shown in figure 1 has been arranged. Krypton, He-Ne and He-Cd lasers have been used in turn in this setup as radiation sources. The use of lasers is not completely necessary for this measurement since the reflectance of these photodiodes varies smoothly with wavelength in the spectral range of interest in this work and therefore the bandwidth effect is either negligible or calculable. However, using laser sources facilitates to control beam parameters such as polarization and incidence angle, which, as mentioned before, has to be very well controlled because of the angular dependency of the photodiode's response.

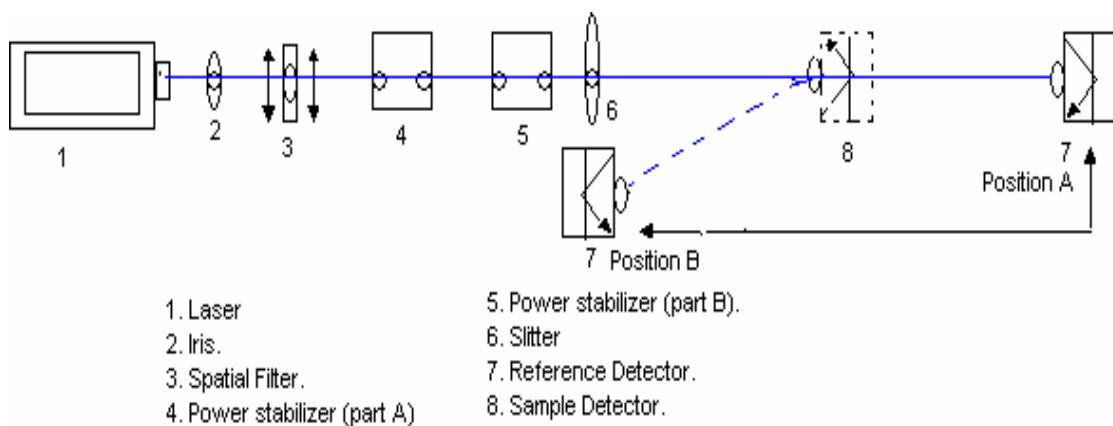


Figure 5.2. Experimental setup for measuring reflectance.

Essentially, the linearly polarized laser beam is spatially filtered and power stabilized by using an electro-optical device. This device has got two parts: The first one has got the electro-optical crystal and the second one has got the monitor detector to keep constant power. This feature allows to stabilize the power at a position different to that of the crystal, although this is not necessary in this setup. Afterward the beam goes through a shutter that can be controlled via a PC (Personal Computer), which is used to block the laser beam to measure the photodiode dark response that is subtracted to every photodiode's reading.

To measure a photodiode reflectance, the reference detector is placed first at position A and its reading is recorded. Afterward the photodiode to be tested is introduced in the laser beam at half way between the shutter and position A, with an angle of incidence about 3° and the reference photodiode is moved to position B and its response recorded. Then the reflectance is given by the ratio between the reference detector reading at position B and the reading at position A. Placing the photodiode to be tested at that position assures that the beam seen by the reference detector runs the same distance in both cases, avoiding errors associated to the divergence of the laser beam. A 3° incidence angle is small enough so that the measured reflectance is considered as the normal incidence reflectance. Finally, just to remark that the reference detector is placed at normal incidence any time..

By this method the spectral reflectance of one set of ten photodiodes from the same manufacturer and batch and another set of three photodiodes (from the same manufacturer) used to maintain the spectral responsivity scale at the Institute for Applied Physics (CSIC) has been measured at wavelengths: 441.8 nm (He-Cd), 568.2 nm (Kr), 632.8 nm (He-Ne) and 647.1 nm (Kr). A typical uncertainty value for this kind of measurement in this laboratory is 0.15 %, which is determined mainly by the measurement

repeatability and the linearity of the reference detector and its associated electronics[12]. Just for identification purposes, the model of all photodiodes studied is S1337-1010BQ.

5.3 Analysis of Spectral Reflectance of Silicon Photodiodes.

The reflectance values measured for photodiodes 1 to 5 are shown in Figure 5.3. Photodiodes 1 and 2 have almost the same behavior, and something similar happens with photodiodes 3 and 4. Only number 5 seems to behave in a more different way [13].

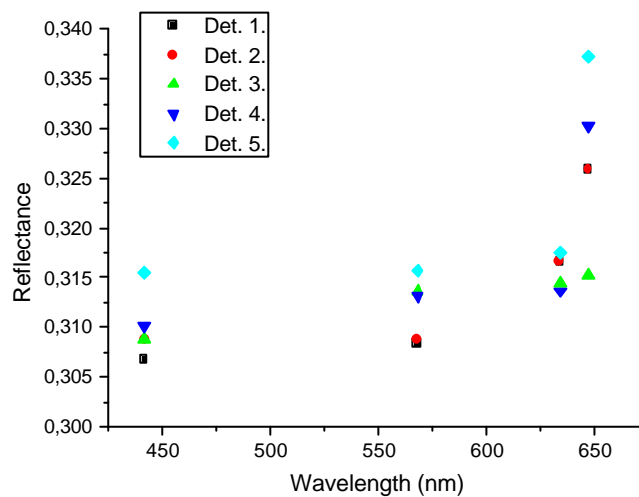


Figure 5.3. Measured reflectance of photodiodes 1 to 5.

Reflectance values measured for photodiodes 6 to 10 are shown in Figure 5.4. Photodiodes 7, 8 and 9 have almost the same behavior up to the wavelength of 632.8 nm from which they differentiate.

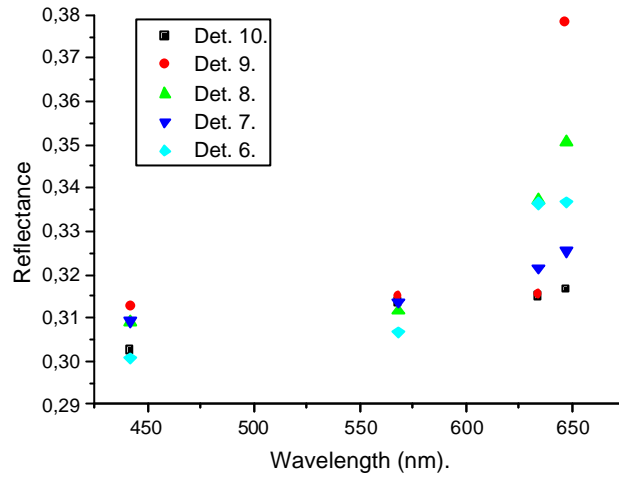


Figure 5.4. Measured reflectance of photodiodes 6 to 10.

In general spectral reflectance values of all the photodiodes studied are closer in the range (441.8 nm - 632.8 nm) and they differentiate more at the 647.1 nm wavelength. Quantitatively, the maximum difference is about 3 % at 441.8 nm and about 7 % at 647.1 nm. Considering the relationship between responsivity and reflectance given by equation 1.37 ($R(\lambda) \propto [1-\rho(\lambda)]$), the variability in reflectance would produce half a variability in responsivity, approximately; i. e. about 1.5 % at short wavelengths and up to a 3.5 % at longer wavelength. According to the data sheet available from the manufacturer, the variability in responsivity among photodiodes can be even larger, therefore it is not only due to the variability in reflectance of the sensitive surface but also to changes in internal quantum efficiency from diode to diode. In the other hand, the results obtained show an outstanding reflectance change among the photodiodes of the same batch, which indicates that it is necessary to measure the reflectance of every individual photodiode if accurate reflectance knowledge is needed, as it is the case for the diodes to be used in silicon trap radiometers for very low uncertainty measurements, in order to place them at most suitable position within the trap.

The second goal of this chapter was to study ageing effect over the reflectance of silicon photodiodes used to maintain responsivity scales. The reflectance values measured in this work for standard detectors Ciri, Dss01 and Dss02, are shown in Figure 5.5. The spectral responsivity of these photodiodes was calibrated six years ago for the first time [1].

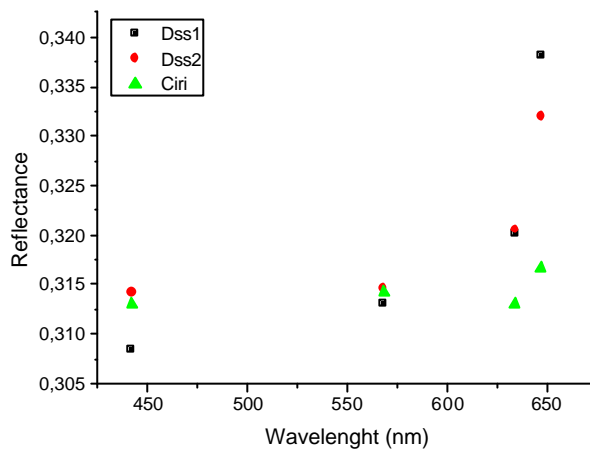


Figure 5.5. Measured reflectance of standard detectors.

Difference between the old spectral reflectance values and the present ones, for these photodiodes can be seen in Figure 5.6.

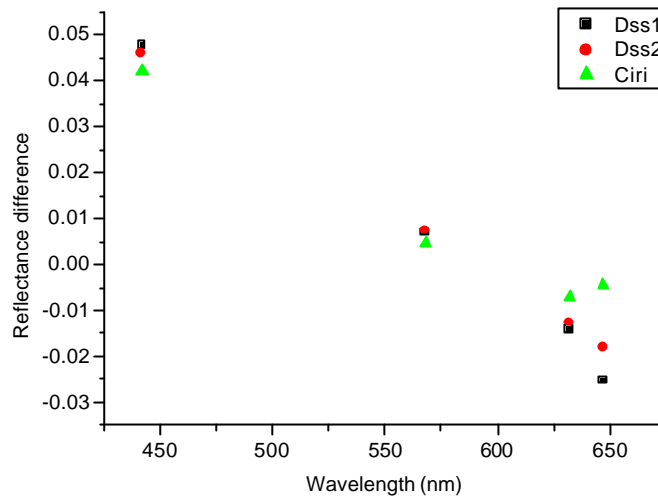


Figure 5.6 Difference between previous spectral reflectance values and this work values

It can be observed the same tendency for the three photodiodes: at short wavelength the reflectance difference is positive; i.e. the photodiode's reflectance has decreased, while at long wavelengths the reflectance difference is negative, which means that the photodiode reflectance has increased. Furthermore, the relative spectral reflectance change is larger at short wavelengths than at long wavelengths. It also seems that the tendency is spectrally monotonous.

If it is assumed that the change in reflectance is related just to a thickness change of the silicon oxide passivation layer, it would be needed an average thickness increase of about 2 nm over 30 nm, which is approximately the average thickness of these photodiodes [1] after manufacturing, to be able to explain such a change. This type of change in the silicon oxide layer has not been referred to in the literature (up to the knowledge of the authors) and it is not likely to be produced since the detectors have always been kept at room temperature in dry environments. Therefore another mechanism must be likely responsible for this behavior [14].

So, the study of standard detectors reflectance shows that ageing occurs in a different way for every one of them. Again, it is necessary to measure the reflectance of every individual photodiode to have a precise knowledge on the evolution of its reflectance. The knowledge of the photodiode reflectance at any wavelength given by the first equation in this chapter is very important in order to interpolate spectral responsivity values [1].

5. 4 Conclusions

At present state of the art of technology, reflectance of silicon photodiodes changes from item to item even within the same batch by an amount larger than the measurement uncertainty that can be expected in doing radiometric measurements with them. Therefore in high accuracy applications where the reflectance plays an important role as is the case of silicon trap detectors for radiometric measurements, it is necessary to measure the reflectance of single elements to select them for matching their reflectance within the trap.

Ageing of silicon photodiodes is not only related to internal quantum efficiency as it has been considered by other authors, but to spectral reflectance changes too as it has been shown in this thesis. The origin of the reflectance change is not likely to be explained just by a change in the silicon oxide thickness.

5.5 References.

- [1]. J. Campos, A. Pons and P. Corredera, “Spectral responsivity scale in the visible range based on single silicon photodiodes”, *Metrologia*, **40**, pág. S181-S184, 2003.
- [2] Gentile T R, Houston J M and Cromer C L, “Realization of a scale of absolute spectral response using the National Institute of Standards and Technology high-accuracy cryogenic radiometer”, *Appl. Opt.* **35**, pág. 4392-4403, 1996
- [3] N P Fox, “Trap Detectors and their Properties”, *Metrologia* **28**, pág. 197-202, 1991.
- [4] L Werner, J Fischer, U Johannsen, J Hartmann, “Accurate determination of the spectral responsivity of silicon trap detectors between 238 nm and 1015 nm using a laser-based cryogenic radiometer”, *Metrologia* **37**, pág. 279-284, 2000.
- [5] Born and Wolf, “principles of Optics”, Pergamon Press, 1980
- [6] R. Goebel and M. Stock, “New Developments in Absolute Radiometry-Nonlinearity and polarization effects in silicon trap detectors”, *Metrologia* **35**, pag. 413-418, 1998.
- [7] J. Campos, P. Corredera, A. Pons, A. Corróns and J. L. Fontecha, “Reflectance dependencies of silicon trap detectors”, *Metrologia*, 1998, **35**, pag. 455-460.
- [8] Raj Korde and Jon Geist, “Quantum Efficiency Stability of Silicon Photodiodes”, *Appl. Opt.* **26**, pag. 5284-5290, 1987.
- [9] L. Werner, “Ultraviolet stability of silicon photodiodes”, *Metrologia* **35**, pag. 407-411, 1998.
- [10] Goebel R., Yilmaz S., Pello R., “Polarization dependence of trap detectors”, *Metrologia*, **33**, pag 207-213, 1996.
- [11] J. Geist, E. F. Zalewski, and A. R. Schaefer, “Spectral Response Self-Calibration and Interpolation of Silicon Photodiodes”, *Appl. Opt.* **19**, pag 3795-3799, 1980.

[12] A. L. Muñoz Zurita, J. Campos Acosta, A. S. Shcherbakov, and A. Pons Aglio. “*Differences of s silicon photodiodes reflectance among a batch and by ageing*”. Proc. of the XXII SOMI Congress, AMZXXII-54, p.1-5, 2007.

[13] A. L. Muñoz Zurita, J. Campos Acosta, A. S. Shcherbakov, and A. Pons Aglio. “*Measuring the reflectance and the internal quantum efficiency of silicon and InGaAs/InP photodiodes in near infrared range*”. Proc of SPIE Photonics West Conference (January 22-26, 2008, San José, USA).

[14] A. L. Muñoz Zurita, J. Campos Acosta, A. S. Shcherbakov, A. Pons Aglio, “*Differences of silicon photodiodes reflectance among a batch and by ageing*”, Optoelectronics Letters, 4(5), (2008).

CHAPTER 6

STUDY OF REFLECTANCE AND NEW MODEL OF INTERNAL QUANTUM EFFICIENCY OF InGaAs/InP PHOTODIODES

The reflectance and the internal quantum efficiency are determined the photodiode spectral responsivity, which is the radiometric characteristic of interest in the fields where these devices can be used for optical radiation measurements. It presents the experimental set up for measuring the photodiode reflectance as well as the results of such measurements related to InGaAs/InP-photodiodes exploited in international laboratories.

The obtained experimental results show that some models of photodiodes have got an anti-reflecting coating on their sensitive facets and that reflectance does not change with varying the light polarization state within the measurement uncertain, when the angles of incidence are less that 7.4 °.

6.1 InGaAs/InP-photodetectors

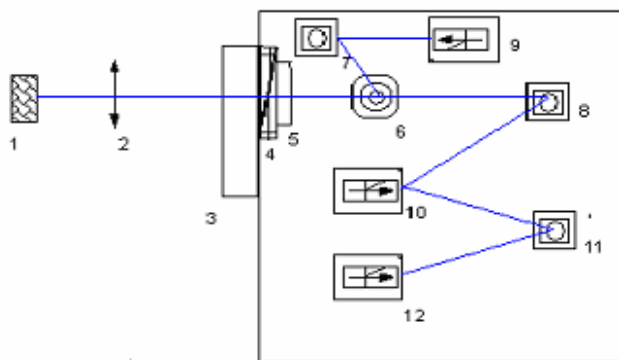
At the present time, the InGaAs/InP-photodetectors from different manufactures have rather low level of noise, a good uniformity of the surface response as well as a wide dynamic range and linearity.

For these reasons they are exploited in the instruments for measuring optical radiation within the near infrared (IR) range (800-1600 nm). Furthermore, the InGaAs/InP-photodetectors are used for

maintaining the scale of spectral responsivity in the same spectral range in many laboratories [1,2]. It presented this work devoted to studying the reflectance of photodiodes from different manufactures. For this reason, measuring the reflectance of photodiodes is presented in this chapter as a preliminary step to finding the responsivity[3,4]. It is seen from equation 2 that the photodiode response depends on a set of parameters inherent in the incident light like the spectral distribution, polarization, modulation of frequency, angle of incidence, and radiant power [5,6]. Then, the response is determined by such characteristics of photodetector as the material refraction index and the structure of diode as well as by some environmental factors, for example, by the temperature[7]

6.2 Experimental procedure

To realize our experiments related to measuring the reflectance of InGaAs/InP photodiodes it have arranged the experimental set-up presented in Figure 6.1



- | | |
|-------------------------------------|-------------------------------------|
| 1. Source light (Incandescent lamp) | 6. Beam splitter AR34 |
| 2. Lens | 7,8,11. Mirrors |
| 3. Monochromator | 9,12. Germanium detectors |
| 4. Polarizer | 10. InGaAs/InP detectors with is |
| 5. Stopper (Choper) | exchanged with standart mirror BK47 |

Figure 6.1. Experimental set-up for measuring the reflectance InGaAs/InP photodiodes

It has exploited an incandescence lamp is the source of white light imaged at the input slit of the monochromator. This lamp was able to cover the spectral range from 800 to 1600 nm and had appropriate blocking filters for second – order wavelengths.

After the monochromator, it had placed a linear polarizer and a beam splitter, which serves to monitor temporal fluctuations of light power. A germanium photodiode was used as the monitoring reference photodetector [8]. The experimental set-up included an optical system of mirrors, which consists of two parts. An upper part (see mirror 7 and germanium photodiode 9) realized monitoring temporal fluctuations of light power.

A bottom part (see mirrors 8, 11; InGaAs/InP-photodiode 10, and and germanium photodiode 12) formed an image of the monochromator's exit slit on the sensitive surfaces of photodiodes. The angle of incidence was equal to 7.4° which was accepted as the normal incidence in this train of measurements. The method of measurement consists in comparing the response from a germanium photodiode to the radiation reflected by the InGaAs/InP photodiode with the response from an aluminium standard mirror whose reflectance is known, so that [9]:

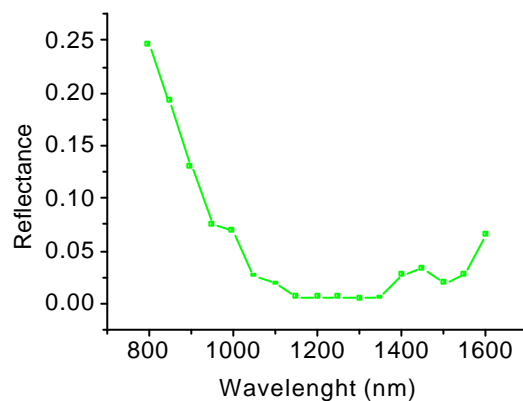
$$\mathbf{r}(\mathbf{I}) = \frac{I_p(\mathbf{I})}{I_m(\mathbf{I})} \mathbf{r}_m(\mathbf{I}) \quad (6.1)$$

Here, $I_p(\mathbf{I})$ is the response to the light reflected by the InGaAs/InP, $I_m(\mathbf{I})$ is the response to the light reflected by the mirror, and $\mathbf{r}_m(\mathbf{I})$ is the reflectance of a standard mirror. With this method it has

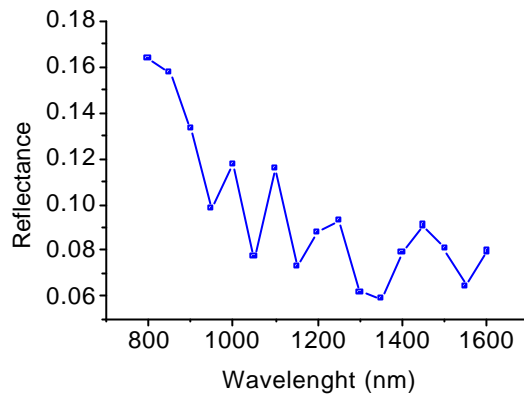
measured the reflectance of photodiodes from different manufacturers. One part of detectors had a round aperture of 5 mm in diameter and the other part had a rectangular aperture of 8 x 8 mm.

6.3. Analysis of Reflectance

The grade of light polarization at the output the monochromator was different with varying the wavelength, figure 6.2 illustrates spectral dependences of the reflectance, which had been obtained from photodetectors belonging to three different manufacturers. In figures 6.2a and 6.2b that the reflectance of such detectors has a minimum in an area of 1000 – 1600 nm, and they both are related to a structure of layers providing maximal responses in the spectral interval of mayor utility of these detectors in near IR optics communication [10]. The first photodiode, see Figure 6.2a, whose reflectance was minimized, is more efficient that the second one, see figure 6.2b.



(a)



(b)

Figure 6. 2. Detector with a round aperture with the diameter of 5 mm

One can see that this plot presents the other spectrum of reflectance in figure 6.3, is associated with a photodiode with rectangular aperture. In this case the reflectance has two minima at 1000 nm and 1600 nm, but the reflectance has a maximum between these minima. This photodiode is older than previous ones, and it was produced by the other manufacturer. One can remark that may be it was produced without good enough control, because the structure of layers on the sensitive surface modifies the reflectance [11].

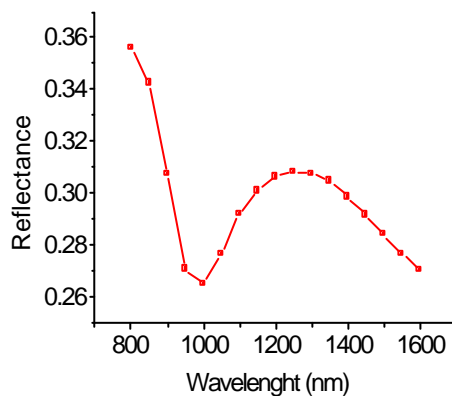


Figure 6. 3 Detector with a rectangular aperture of 8 x 8mm

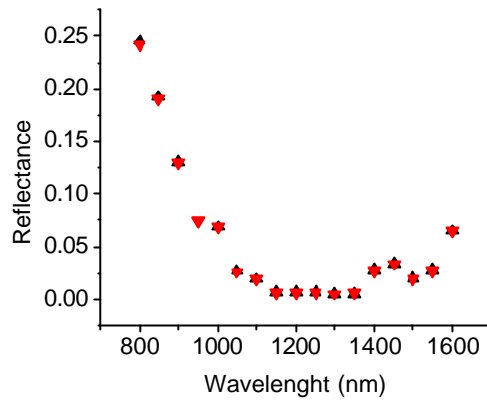


Figure 6.4

Spectrum of reflectance for photodiodes 1 and 4

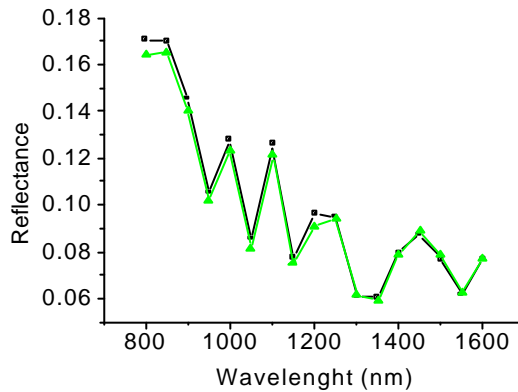


Figure 6.5 Spectrum of reflectance of photodiodes 2 and 5

The spectrum of reflectance for photodiodes 1 and 4 is presents in figure 6.4 which belong to the same manufacturer. The reflectance was measured with linearly polarized and non-polarized lights, and these pair of measurements gives quite similar results. In fact, the difference was equal to approximately 2%. The same results are depicted for the photodiodes 2 and 5, by the second manufacturer. It is important that the results do not depend on the polarization state of the incident light when the angle of incidence is smaller 10 angular degrees [12].

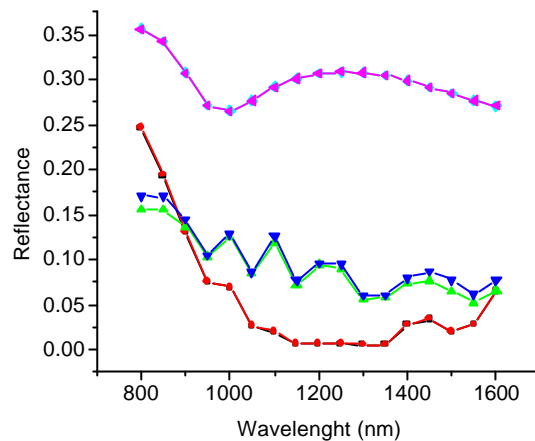


Figure 6.6 Spectrum of reflectance of photodiodes 1-6.

All spectrums of reflectance for photodiodes 1-6 is presents in the figure 6, with linearly polarized and non polarized lights and is possible to see the different behavior of the photodiodes in the near infrared wavelength.

In fact, in this thesis is studying the behavior of the photodetectors in the near infrared with the linearly polarized and non polarized lights in the case of the polarized lights the angle of incidence is smaller 10 angular degrees and is possible observed it doesn't have changes in the behavior of the reflectance.

6.4 New Model of Quantum Internal Efficiency of some photodetectors of InGaAs.

The responsivity measurement [R(λ)]: Measured by comparison to an electrically calibrated pyroelectric radiometer (ECPR), obtaining responsivity values with an uncertainty of 1.2 % approximately, roughly the uncertainty of the ECPR. Spectral responsivity values of one photodiode

from every manufacturer obtained from measurements are shown in figure 6.7 (analogous results are obtained for photodiodes from the same manufacturer).

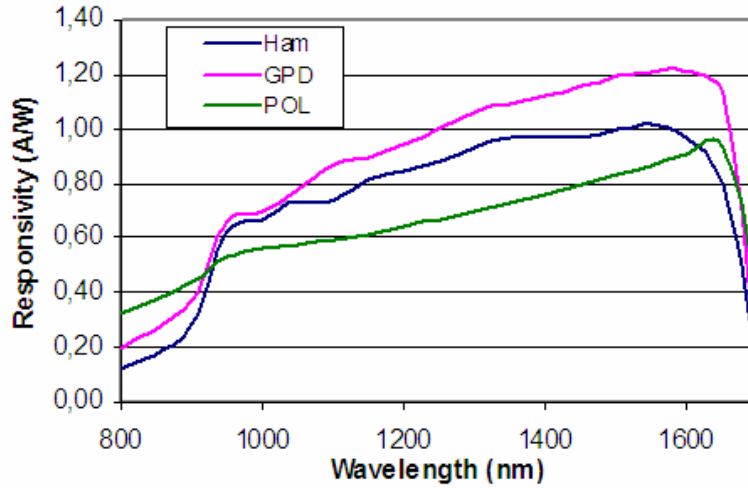


Figure 6.7 Spectral responsivity values of photodiodes.

6.4.1 External quantum efficiency.

It is obtained from the responsivity values according to the equation:

$$Q(l) = \frac{R(l) hc}{l e} , \quad (6.2)$$

Where h , c and e are the usual physical constants and l is the wavelength.

Values obtained are presented in figure 6.8 for the same detectors as before. It can be clearly seen that the oldest detector (POL) presents a lower external quantum efficiency than the other and that detector GPD presents a higher external quantum efficiency than detector HAM, which starts to decrease its quantum efficiency at a shorter wavelength.

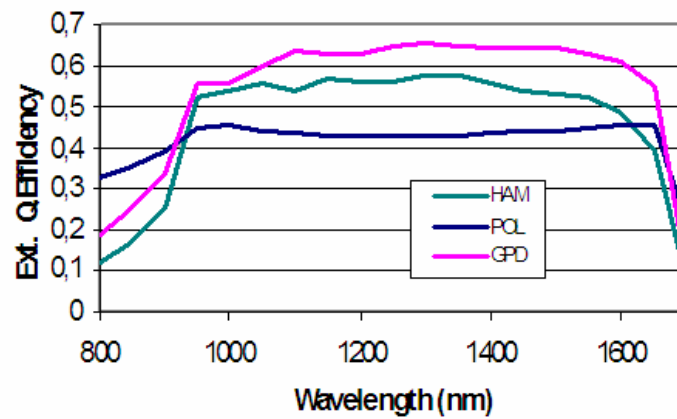


Figure 6.8. Spectral external quantum efficiency from responsivity values

6.4.2 Photodiode structure

Precise structure is not known. The assumed internal structure for photodiodes is shown in figure 6.9. It is more than likely that detector POL has got a different structure.

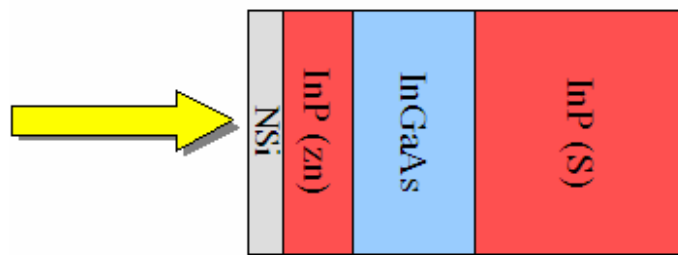


Figure 6.9. Possible Internal Structure

Spectral Reflectance measured and fitted values for photodiodes HAM and GPD

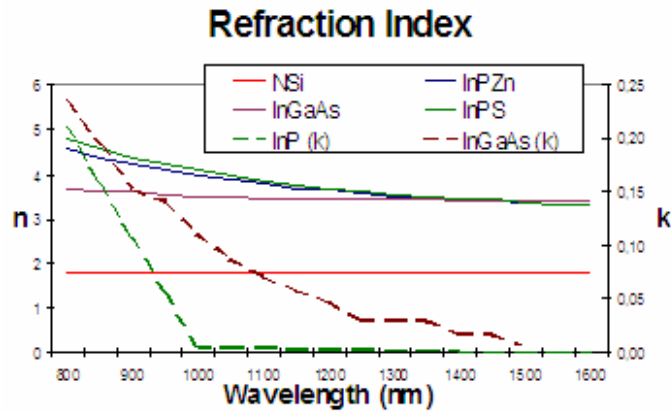


Figure 6.10 Materials' Refraction Index

Considering for the photodiodes the structure and refractive index values shown (figures 3 and 4), the reflectance can be fitted by using a multilayer model. Results obtained are shown in figure 6, except for photodiode POL that gave a poorer result. The thickness values obtained from the fit are shown in the table.

Photodiode	NSi	InP (Zn)	InGaAs
HAM	162.17nm	1213.35nm	1593.2nm
GPD	159.99nm	1200.54nm	1536.7nm

6.4.3 Internal quantum efficiency.

Internal quantum efficiency, $e(l)$, is calculated as usual: $e(l) = Q(l) / (1-r(l))$. Values obtained are shown in figure 6 for photodiodes HAM and GPD.

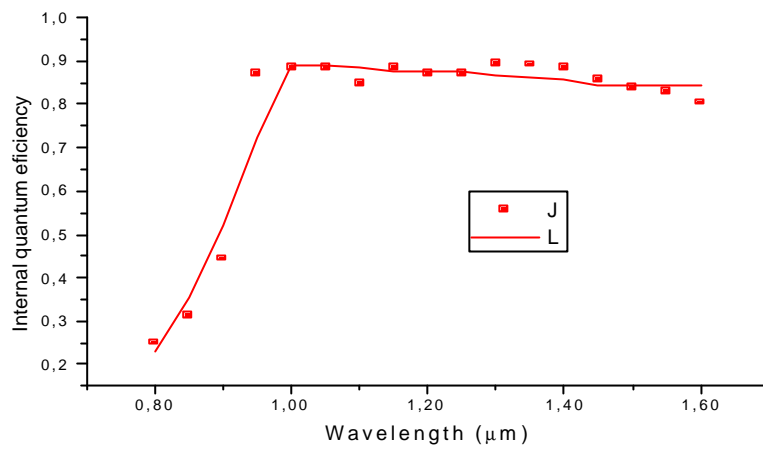


Figure 6.11 Internal quantum efficiency of photodiodes HAM experimental values (dots) and fitted values according to the model shown below.

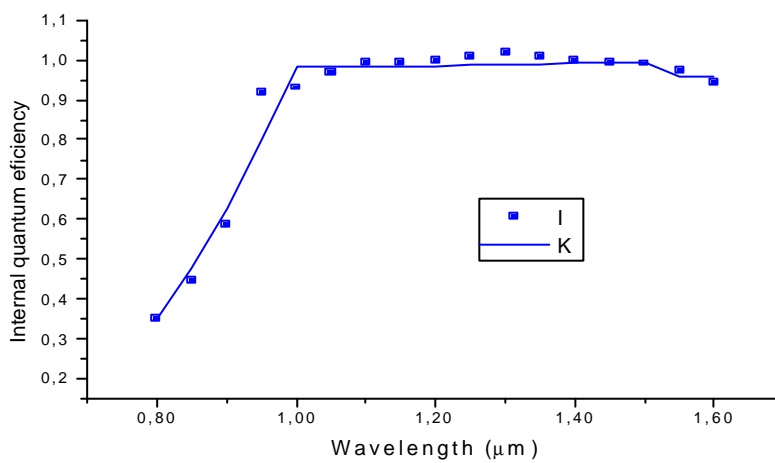


Figure 6.12 Internal quantum efficiency of photodiodes GPD experimental values (dots) and fitted values according to the model shown below.

Considering a structure as shown before and a simple model for the collection efficiency of carriers in all regions given by a constant value, P_f , lower than 1 in the first region, 1 in the depletion region and P_b in the back region, and an “infinite” thickness for the diode, $e(l)$ can be calculated by:

$$e(l) = P_f(1 - \exp(-aT)) + \exp(-aT) - \exp(-aT') + \exp(-aT') - \exp(-aD') - \exp(-aD) + \exp(1 - P_b) \exp(-aD) \quad (6.3)$$

Where T is the thickness at which collection efficiency becomes 1, T' is the thickness at which InGaAs region starts, D' is the the thickness at which the InP (S) starts and D is the thickness at which depletion region ends. By fitting the model to internal quantum efficiency value, the following parameters are obtained for every photodiode [13,14].

Photodiode	Pf	T	T'	D'	D	Pb
HAM	0	0.44	2.19	2.19	11.96	0.844
GPD	0	0.32	1.65	1.62	4351.16	0.960

6.5 Conclusions

The reflectance was measured with linearly polarized and non-polarized lights, and these pair of measurements gives quite similar results. In fact, the difference was equal to approximately 2%. The same results are depicted for the photodiodes 2 and 5, by the second manufacturer. It is important that the results do not depend on the polarization state of the incident light when the angle of incidence is smaller 10 angular degrees.

In fact in this thesis it are studying the behavior of the photodetectors in the near infrared with the linearly polarized and non polarized lights in the case of the polarized lights the angle of incidence is smaller 10 angular degrees and is possible observed it don't have changes in the behavior of the reflectance.

Reflectance fitting is better for HAM than for GPD. Perhaps the structure model needs some refinement. Internal Quantum Efficiency fitting is not very good at the elbow region.

6.6 References.

- [1]. J. Campos, P. Corredera, A. Pons, A. Corróns J. L. Fontecha. “Reflectance dependencies of silicon trap detectors”. ,IOP Metrología, 35, 455-460,(1998).
- [2]. P Corredera, M L Hernanz, M González-Herráez, J Campos “Anomalous non-linear behaviour of InGaAs photodiodes with overfilled illumination” IOP Metrología 40, S181-S184,(2003).
- [3]. P Corredera, M L Hernanz, J Campos, A Corróns, A Pons and J L Fontecha.. “Comparison between absolute thermal radiometers at wavelengths of 1300 nm and 1550 nm” IOP Metrología. 37. 237-247, (2000).
- [4]. J.Castrellon, G.Paez, M.Strojnjk. “Radiometric ana lisis of a fiber optic temperatura sensor” Opt. Eng, 41 (6),1255-1261 (2002).
- [5]. R. Goebel, S. Yilmaz, R.Pello.“Polarization dependence of trap detectors” IOP Metrología, 33,207-213, (1996).
- [6]. E.F.Zalewski, C.R.Duda, “Silicon photodiode device with 100% external quantum efficiency” Appl.Opt.,22, 2867-2873, (1983).
- [7]. J.M.Coutin, F.Chandoul, J.Bastie. “Characterization of new trap detectors as transfer standards” Proceedings of the 9th international conference on new developments and applications in optical radiometry.(2005).
- [8] **A.L.Muñoz Zurita, J.Campos Acosta, A.S.Shcherbakov, A.Pons Aglio.“Medida de reflectancia y de fotodiodos de InGaAs/InP”. Proc. of the VIII National Meeting on Optics, (Optical Society of Spain), p.27-30 (2006).**

- [9] A.L.Muñoz Zurita, J.Campos Acosta, A.S.Shcherbakov, and A.Pons Aglio. “Medida de reflectancia y linealidad de fotodiodos de InGaAs/ InP”. Proc. of the XXI SOMI Congress, AMZ 95, p.1-5 (2006).
- [10]. A.L.Muñoz Zurita, J.Campos Acosta, A.Pons Aglio. A.S.Shcherbakov. “Medida de la reflectancia de fotodiodos de InGaAs/InP”. *Óptica Pura y Aplicada*, 40(1), 105-109 (2007).
- [11] A.L.Muñoz Zurita, J.Campos Acosta, A.S.Shcherbakov, and A. Pons Aglio. “Measuring the reflectance and internal quantum efficiency of InGaAs/InP photodiodes in near infrared range”. Proc.of the IX International Congress on Advanced Infrared Technology and Applications, (AITA -9), p.1-6 (2007).
- [12]. A.L.Muñoz Zurita, J.Campos Acosta, A.Pons Aglio. A.S.Shcherbakov. “Medida de la reflectancia de fotodiodos de InGaAs/InP” *Óptica Pura y Aplicada*, 40(1), 105-109 (2007).
- [13] A.L.Muñoz Zurita, J.Campos Acosta, A.S.Shcherbakov, and A.Pons Aglio. “Measuring the reflectance and the internal quantum efficiency of silicon and InGaAs/InP photodiodes in near infrared range”. Proc of SPIE Photonics West Conference (January 22-26, 2008, San José, USA).
- [14] A.L.Muñoz Zurita, J.Campos Acosta, A.S.Shcherbakov, and A.Pons Aglio. “External Quantum efficiency of some InGaAs/InP photodiodes”, Proc of NewRad2008 congress, MO_P41, (1-3).

CHAPTER 7

GENERAL CONCLUSIONS

In this chapter the final conclusions of this Ph.D thesis are described. The results obtained during this work were shown.

The presented material as a stimulating contribution to the development of the advanced metrology. Such a viewpoint is based on the two well-determined propositions. The first of them is represented by our theoretic approach to the characterization of low-power bright picosecond optical pulses with an internal frequency modulation simultaneously in time and frequency domains. This proposition exploits the joint Wigner time-frequency distribution, which can describe the width and the frequency chirp of optical pulse in a unified format. The case, being practically much used, of Gaussian shape when the Wigner distribution is positive has been taken, and the peculiarities for just the Gaussian pulses with a high-frequency filling have been followed in details in both time and frequency domains as well as in terms of the field-strength auto-correlation function. The second proposition is related to the principles of creating the joint Wigner time-frequency distribution by the methods of modern experimental technique. It has proposed and considered conceptually the key features of a new interferometric method elaborated explicitly for accurate and reliable measurements of the train-average width as well as the value and sign of the frequency chirp in bright picosecond optical pulses in high-repetition-rate trains. For this purpose, a two-beam scanning Michelson interferometer has been chosen for obtaining the field-strength auto-correlation function of low-power picosecond pulse trains. The proposed technique is founded on an ingenious algorithm of metrology, assumes using a specially designed two-

domain supplementary semiconductor cell, and suggests carrying out a pair of additional measures with exploiting this semiconductor cell, whose properties have been physically described as well. The procedure makes possible constructing the current Wigner distribution in real time scale, which is rather desirable practically, and thus describing low-power bright picosecond optical pulses simultaneously in both time and frequency domains.

The intensity triple auto-correlation function of the optical pulses is known, the pulse shape $I(t)$ can be reconstructed using the algorithm described in this article. Figure 4.6 illustrates the corresponding steps of such a reconstruction. Thus, this technique makes possible measuring asymmetric envelopes of ultrashort optical pulses and recovering signals almost unambiguously. We used the phase of the different pulse and with this is possible to observed better behavior or form of the pulse and we have more details in the reconstruction of these pulses.

Now it has a new technique it is base in the triple correlation and is possible to create the algorithm by the measurement. In this case is using the technique of interferometer, with the measurements and the use of the triple correlation.

Reflectance measurements of high quality, large area silicon photodiodes have shown that their responsivity ageing is not only due to internal quantum efficiency temporal drift, as shown by other authors previously, but to a change in the reflectance too. The magnitude of this change, which is dependent on the individual photodiode, cannot be reasonably explained by just a change in the silicon oxide thickness. Therefore some more work will have to be done in the future in order to explain this

change, perhaps considering that internal changes effecting quantum efficiency drift may have some influence on the complex refraction index of the silicon as well.

In the other hand, measured reflectance changes from diode to diode within a set of ten silicon diodes from the same batch and model than the former ones, at present technology state of the art, are not totally responsible for the typical variability of the responsivity claimed by the manufacturer. Therefore the internal quantum efficiency also notably changes from diode to diode. In addition, the variability of the measured reflectance is such that in high accuracy applications where the reflectance plays an important role as in the case of silicon trap detectors for radiometric measurements, it is necessary to measure the reflectance of single elements to select them for matching their reflectance at some trap positions.

The spectral responsivity of InP photodiodes can be determined from the knowledge of their reflectance and internal quantum efficiency. At present the internal structure of these photodiodes and the composition of the materials composing them are not precisely known what do not allow estimating those quantities. To overcome that, experimental reflectance values have been fitted to a layered structure model obtaining a good agreement with experimental values. Using this layer structure, a internal quantum efficiency model has been proposed based on the thickness of the internal layers and the complex refractive index of the materials composing the layers. The model has been fitted to real values of internal quantum efficiency, calculated from the responsivity and reflectance measurements, and a good agreement has been also found between the model and the values. Therefore, by using these models the spectral responsivity can be calculated at any wavelength within the spectral interval of sensitivity. These calculated values will have to be compared to those obtained by calibrating the photodiode against another radiometer, what will be done in a future work.

STATEMENTS

- The proposed interferometric technique with a supplementary semiconductor cell is capable of measuring accurate and unambiguously the train-average pulse width as well as the value and sign of the frequency chirp of picosecond optical pulses with Gaussian and hyperbolic-secant shapes in high-repetition-rate trains and makes possible creating the corresponding joint Wigner time-frequency distributions.
- Applying the algorithm of triple correlation to precise characterization of picosecond optical pulses with arbitrary parameters in high-repetition-rate trains provides recovering the train average distributions for both the amplitude (intensity) and the phase of optical pulses.
- InP photodiodes' reflectance can be modeled by using a layered optical system having got a first transparent layer and three absorbing ones.
- InP photodiodes' internal quantum efficiency can be adequately modeled by a three region structure, where the charge collection efficiency is constant in the two first regions and variable in the last one.

- Responsivity ageing of high quality silicon photodiodes is determined not only by the internal quantum efficiency temporal drift, as shown previously by other authors, but by reflectance changes too.

APPENDIX I:

ORIGINATING THE JOINT WIGNER TIME-FREQUENCY DISTRIBUTION.

When the spectrum of signal varying in time is the subject of interest, it is rather worthwhile to refer to applying some joint function of the time and frequency, which would be able to describe the intensity distribution of this signal simultaneously in time domain as well as in frequency one. Such a distribution gives us opportunities for determining a relative part of energy at a given frequency in the required temporal interval or for finding the frequency distribution at a given instant of time.

The method of deriving the time-frequency distribution can be based on usage of the corresponding characteristic function. Let us assume that some time-frequency distribution $\mathbf{W}(\mathbf{t}, \mathbf{w})$ exists and presents a function of two variables \mathbf{t} and \mathbf{w} .

The characteristic function $\mathbf{M}(\mathbf{q}, \mathbf{t})$ inherent in this distribution can be written as mathematical expectation of the value $\exp(\mathbf{i} \mathbf{q} \mathbf{t} + \mathbf{i} \mathbf{t} \mathbf{w})$, i.e. as

$$\mathbf{M}(\mathbf{q}, \mathbf{t}) = \langle \exp(\mathbf{i} \mathbf{q} \mathbf{t} + \mathbf{i} \mathbf{t} \mathbf{w}) \rangle = \int_{-\infty}^{\infty} \int_{-\infty}^{\infty} \mathbf{W}(\mathbf{t}, \mathbf{w}) \exp(\mathbf{i} \mathbf{q} \mathbf{t} + \mathbf{i} \mathbf{t} \mathbf{w}) \mathbf{d} \mathbf{t} \mathbf{d} \mathbf{w}. \quad (\text{A1})$$

In its turn, the time-frequency distribution $\mathbf{W}(\mathbf{t}, \mathbf{w})$ can be found from the characteristic function $\mathbf{M}(\mathbf{q}, \mathbf{t})$ as

$$W(\mathbf{t}, \mathbf{w}) = \frac{1}{4\pi^2} \int_{-\infty}^{\infty} \int_{-\infty}^{\infty} M(\mathbf{q}, \mathbf{t}) \exp(-i\mathbf{q}\mathbf{t} - i\mathbf{t}\mathbf{w}) d\mathbf{q} d\mathbf{t} \quad (\text{A2})$$

Due to the characteristic function is some averaged value, one can use quantum mechanics method of the associated operators with ordinary variables. If we have the function $\mathbf{g}_1(\mathbf{t})$ depending only on the time \mathbf{t} , the average value for this function can be calculated by two ways, namely, exploiting the complex amplitude $\mathbf{A}(\mathbf{t})$ of a signal or its complex spectrum $\mathbf{S}(\mathbf{w})$ as

$$\langle \mathbf{g}_1(\mathbf{t}) \rangle = \int_{-\infty}^{\infty} \mathbf{g}_1(\mathbf{t}) |\mathbf{A}(\mathbf{t})|^2 d\mathbf{t} = \int_{-\infty}^{\infty} \mathbf{S}^*(\mathbf{w}) \mathbf{g}_1 \left(i \frac{d}{d\mathbf{w}} \right) \mathbf{S}(\mathbf{w}) d\mathbf{w} \quad (\text{A3})$$

because the time can be represented by the operator $i d/d\mathbf{w}$ in the frequency domain. Then, for the function $\mathbf{g}_2(\mathbf{w})$ depending only on the frequency \mathbf{w} , the average value can be estimated by

$$\langle \mathbf{g}_2(\mathbf{w}) \rangle = \int_{-\infty}^{\infty} \mathbf{g}_2(\mathbf{t}) |\mathbf{S}(\mathbf{w})|^2 d\mathbf{w} = \int_{-\infty}^{\infty} \mathbf{A}^*(\mathbf{t}) \mathbf{g}_2 \left(-i \frac{d}{d\mathbf{t}} \right) \mathbf{A}(\mathbf{t}) d\mathbf{t} \quad (\text{A4})$$

because the frequency is represented by the operator $-i d/d\mathbf{t}$ in the time domain as well. Consequently, one can combine the time and frequency with the non-commutative operators $\hat{\mathbf{A}}$ and $\hat{\hat{\mathbf{A}}}$, so that

$$\hat{\mathbf{A}} \otimes \mathbf{t}, \quad \hat{\hat{\mathbf{A}}} \otimes -i \frac{d}{d\mathbf{t}} \text{ in the time domain;}$$

$$\hat{A} \otimes i \frac{d}{d w}, \quad \hat{A} \otimes w \quad \text{in the frequency domain;}$$

where $\hat{A} \hat{A} - \hat{A} \hat{A} = i$. Introducing the operator $G(\hat{A}, \hat{A})$, associated with the function $g(t, w)$, one can write

$$\langle g(t, w) \rangle = \int_{-\infty}^{\infty} A^*(t) G(t, \hat{A}) A(t) dt = \int_{-\infty}^{\infty} S^*(w) G(\hat{A}, w) S(w) dw \quad (A5)$$

Due to the characteristic function is a mathematical expectation, one can apply Eq.(A5) to estimate $M(q, t)$ via

$$M(q, t) = \langle \exp(iqt + itw) \rangle \otimes \int_{-\infty}^{\infty} A^*(t) \exp(iq\hat{A} + it\hat{A}) A(t) dt. \quad (A6)$$

In fact, Eq.(A6) includes the Weil correspondence $\exp(iqt + itw) \otimes \exp(iq\hat{A} + it\hat{A})$, but such a correspondence is not a uniquely applicable. In principle, it can be generalized by substituting the normal ordered correspondences that leads to another possible time-frequency distributions. Nevertheless, now we have an opportunity to calculate the characteristic function $M(q, t)$ using Eq.(A6). In so doing, one has to take the particular case of well-known Backer-Hausdorff operator formula

$$\exp(iq\hat{A} + it\hat{A}) = \exp(-iqt/2) \exp(it\hat{A}) \exp(iq\hat{A}), \quad (A7)$$

where $\exp(it\hat{A})$ is the operator, because

$$\exp(i t \hat{A}) \mathbf{A}(t) = \exp(t d/dt) \mathbf{A}(t) = \mathbf{A}(t+t). \quad (\text{A8})$$

Substituting Eq.(A8) into Eq.(A6), one can yield

$$\mathbf{M}(q, t) = \int_{-\infty}^{\infty} \mathbf{A}^*(t) \exp(-iqt/2) \exp(iqt) \mathbf{A}(t+t) dt. \quad (\text{A9})$$

At this stage, a new independent variable $\mathbf{u} = t - t/2$ with $d\mathbf{u} = d\mathbf{t}$ can be introduced, so

$$\mathbf{M}(q, t) = \int_{-\infty}^{\infty} \mathbf{A}^*\left(\frac{\mathbf{x}}{e} \mathbf{u} - \frac{t}{2}\right) \exp(iqu) \mathbf{A}\left(\frac{\mathbf{x}}{e} \mathbf{u} + \frac{t}{2}\right) d\mathbf{u}. \quad (\text{A10})$$

Now we use Eq.(A2) to obtain the time-frequency distribution $\mathbf{W}(t, w)$

$$\mathbf{W}(t, w) = \frac{1}{4p^2} \int_{-\infty}^{\infty} \int_{-\infty}^{\infty} \mathbf{A}^*\left(\frac{\mathbf{x}}{e} \mathbf{u} - \frac{t}{2}\right) \exp(iqu) \mathbf{A}\left(\frac{\mathbf{x}}{e} \mathbf{u} + \frac{t}{2}\right) \exp(-iqt - itw) dq dt d\mathbf{u} \quad (\text{A11})$$

The integration with respect to q gives the Dirac delta-function $d(\mathbf{u} - t)$ in Eq.(A11), i.e.

$$\mathbf{W}(t, w) = \frac{1}{2p} \int_{-\infty}^{\infty} d(\mathbf{u} - t) \mathbf{A}^*\left(\frac{\mathbf{x}}{e} \mathbf{u} - \frac{t}{2}\right) \mathbf{A}\left(\frac{\mathbf{x}}{e} \mathbf{u} + \frac{t}{2}\right) \exp(-itw) dt d\mathbf{u} \quad (\text{A12})$$

Then, integrating with respect to \mathbf{u} , we arrive at the Wigner time-frequency distribution

$$\mathbf{W}(t, w) = \frac{1}{2p} \int_{-\infty}^{\infty} \mathbf{A}^*\left(\frac{\mathbf{x}}{e} t - \frac{t}{2}\right) \exp(-itw) \mathbf{A}\left(\frac{\mathbf{x}}{e} t + \frac{t}{2}\right) dt. \quad (\text{A13})$$

This distribution can be explained in terms of frequency as well by the following integral expression

$$\mathbf{W}(\mathbf{t}, \mathbf{w}) = \frac{1}{2\pi} \int_{-\infty}^{\infty} \int_{-\infty}^{\infty} \mathbf{S}^* \left(\frac{\mathbf{q}}{c} \mathbf{w} - \frac{\mathbf{q}}{2\theta} \right) \exp(i\mathbf{t}\mathbf{q}) \mathbf{S} \left(\frac{\mathbf{q}}{c} \mathbf{w} + \frac{\mathbf{q}}{2\theta} \right) d\mathbf{q} . \quad (\text{A14})$$

The kernel of this distribution is equal to unity, while the kernel of the Wigner transformation depends on the product of the arguments. The power density $|\mathbf{A}(\mathbf{t})|^2$ and the spectrum density $|\mathbf{S}(\mathbf{w})|^2$ are determined by

$$\text{a) } |\mathbf{A}(\mathbf{t})|^2 = \int_{-\infty}^{\infty} \mathbf{W}(\mathbf{t}, \mathbf{w}) d\mathbf{w} , \quad (\text{A15})$$

$$\text{b) } |\mathbf{S}(\mathbf{w})|^2 = \int_{-\infty}^{\infty} \mathbf{W}(\mathbf{t}, \mathbf{w}) d\mathbf{t} .$$

FIGURE INDEX

CHAPTER 1

Figure 1.1	10
Describe linear variation of frequency inside the pulse or the internal phase modulation, or the frequency chirp.	
Figure 1.2	15
Theoretical correlation traces for SHG and TPF measurements	
Figure 1.3	17
Illustrate the set-up for shaping both cross-correlation and auto-correlation functions	
Figure 1.4	18
Exploiting a two-beam Michelson interferometer as the correlator of the field strength	
Figure 1.5	21
Interferometric arrangement for pulse correlation measurement by SHG	
Figure 1.6	22
Triangular arrangements for TFP	

CHAPTER 2

Figure 2.1.	38
The Wigner time-frequency distribution for the Gaussian pulse with $T=1$ and the varying parameter b : (a) $b=0$, (b) $b=2$, (c) $b=4$, and (d) $b=6$	
Figure 2.2.	40
The Gaussian pulse with $T=1$: the power density profile (a) and the spectral density profiles (b) with the varying parameter of the frequency chirp: solid line for $b=0$, dashed line for $b=2$, dash-dotted line for $b=4$, and dotted line for $b=6$	
Figure 2.3.	41
The plots of $I(t)$ and $J(t)$ with : (a) $b=0$, $T=1$, $\Omega=10$; (b) $b=4$, $T=1$, $\Omega=10$	
Figure 2.4.	43
Spectral intensity of Gaussian pulses: $b=0$, $T=1$, $\Omega=10$ – dashed line; $b=4$, $T=1$, $\Omega=10$ – solid line	
Figure 2.5.	46
Field-strength auto-correlation functions for the Gaussian pulses with: (a) $b=0$, $T=1$, $\Omega=40$; (b) $b=4$, $T=1$, $\Omega=40$	
Figure 2.6.	49
Michelson interferometer with a supplementary semiconductor cell	

Figure 2.7.	50
Design of the supplementary semiconductor cell: I is the domain of linear amplification controlled by the pump current J ; II is the domain with a fast-saturable absorption	
Figure 2.8	52
Results of numerical simulation of forming the auto-correlation functions by the scanning Michelson interferometer: (a) without and (b) with an supplementary semiconductor cell introduced into the measurement circuit	

CHAPTER 3

Figure 3.1.	60
The Wigner time-frequency distribution for a sech-shaped pulse with $t_0 = 1$ and the varying parameter b : (a) b = 0 , (b) b = 1 , (c) b = 2 b = 4 , and (d) b = 4	
Figure 3.2	62
The sech-pulse with $t_0 = 1$ $t_0 = 1$: the power density profile (a) and the spectral density profiles (b) with the varying parameter b of the frequency chirp: b = 0 (for the maximal intensity plot), b = 2/p , b = 1 , b = 2 , and b = 4 (for the minimal intensity plot)	
Figure 3.3	67
The plots of I(t) and J(t) with : (a) b = 0 , $t_0 = 1$, W = 10 ; (b) b = 4 , $t_0 = 1$, W = 10	
Figure 3.4	75
The normalized real parts of field-strength auto-correlation functions for the sech-pulses with: (a) b = 0 , $t_0 = 1$, W = 40 ;(b) b = 1 , $t_0 = 1$, W = 40	
Figure 3.5.	76
The normalized square-average time duration t_A/t_0 of the field strength auto-correlation function versus the frequency chirp b for a sech-pulse: (a) b ≠ 1 and b ≈ 1	
Figure 3.6.	77
Two practically acceptable simple approximations for the function F(b) with different values of the factor a	

CHAPTER 4

Figure 4.1	92
The envelope, triple auto-correlation, and bispectrum for real Gaussian pulse	
Figure 4.2	92
The envelope, triple auto-correlation, and bispectrum for real rectangular pulse	
Figure 4.3	94
Triple auto-correlation function for the chirped Gaussian pulse with $a = 0.5$ and $b = 1.0$: (a) real-valued part, (b) imaginary-valued part	
Figure 4.4.	95
Bispectrum for the chirped Gaussian pulse with $a = 0.5$ and $b = 1.0$: (a) real-valued part, (b) imaginary-valued part...	
Figure 4.5.	99
A three-beam interferometer for registering the intensity triple auto-correlation function	
Figure 4.6	100
Direct third harmonic generation	
Figure 4.7	100
Cascade third harmonic generation	
Figure 4.8	101
The steps of reconstructing an asymmetric optical pulse: the upper insert is for the triple auto-correlation function; then, two inserts are for real and imaginary parts of the bispectrum; the bottom insert is for the reconstructed pulse.....	

CHAPTER 5

Figure 5.1	107
Silicon photodiode structure	
Figure 5.2.	109
Experimental setup for measuring reflectance	
Figure 5.3	111
Measured reflectance of photodiodes 1 to 5	
Figure 5.4	112
Measured reflectance of photodiodes 6 to 10	
Figure 5.5	113
Measured reflectance of standard detectors	
Figure 5.6	114
Difference between previous spectral reflectance values and this work values	

CHAPTER 6

Figure 6.1	120
Experimental set-up for measuring the reflectance InGaAs/InP photodiodes	
Figure 6. 2	122
Detector with a round aperture with the diameter of 5 mm	
Figure 6. 3	123
Detector with a rectangular aperture of 8 x 8mm	
Figure 6.4	
Spectrum of reflectance for photodiodes 1 and 4	123
Figure 6.5	
Spectrum of reflectance of photodiodes 2 and 5.....	123
Figure 6.6	124
Spectrum of reflectance of photodiodes 1-6	
Figure 6.7	125
Spectral responsivity values of photodiodes	
Figure 6.8	126
Spectral external quantum efficiency from responsivity values	
Figure 6.9	127
Possible Internal Structure	
Figure 6.10	127
Materials' Refraction Index	
Figure 6.11	128
Internal quantum efficiency of photodiodes HAM experimental values (dots) and fitted values according to the model shown below	
Figure 6.12	128
Internal quantum efficiency of photodiodes GPD experimental values (dots) and fitted values according to the model shown below	